Ab initio calculation of the coefficient of thermal expansion and the secondary pyroelectric vector

Fredrik Nyberg

Thesis submitted for the degree of

Master in Materials, Energy and Nanotechnology

60 credits

Department of physics

Faculty of mathematics and natural sciences

UNIVERSITY OF OSLO

November / 2020

Ab initio calculation of the coefficient of thermal expansion and the secondary pyroelectric vector

Fredrik Nyberg

2020

Ab initio calculation of the coefficient of thermal expansion and the secondary pyroelectric vector

Fredrik Nyberg

https://www.duo.uio.no/

Trykk: Reprosentralen, Universitetet i Oslo

Abstract

The world desperately needs new sources of renewable energy. One renewable source that has not been studied a lot, is pyroelectric phase-transforming materials (PTM). The purpose was to find a material that went through a phase change in the investigated temperature and pressure range, where the two phases have different pyroelectric vectors. This may cause a large electrical field over the material upon the phase change and by connecting it to an extrinsic circuit, a current may be produced. In order to find a pyroelectric PTM, many properties are needed. Some of these are the coefficient of thermal expansion (CTE), the piezoelectric tensor, the third order force constants at, and the Gibbs free energy. These have been found. In addition, the specific heat capacity at constant volume as a function of temperature has also been found. The CTEs and heat capacities were calculated as a function of temperature for diamond and three "Heusler alloys". The Gibbs free energies were found in the same temperature ranges for each material, and as a function of pressure too. The CTEs were found because thermal expansion leads to strain in the material that changes the electric dipole moment by a piezoelectric process[1]. This process is what the secondary pyroelectric vector accounts for. The Gibbs free energy was found as a function of temperature and pressure to see if some of the materials would go through a phase change in the temperature and pressure range investigated. The third order force constants were investigated because they are needed for the primary pyroelectric vector. The primary effect is the change in electric dipole moment by a change in the temperature at constant strain, so that expansion or compression are not possible[1]. The heat capacities were plotted because they are automatically calculated during the process of the present work and are interesting in many cases. The present work has used density functional theory (DFT) like calculations through the Vienna ab initio simulation program (VASP)[2-5] and the temperature dependent effective potential (TDEP) package[6-8].

Experimental values of the CTE of diamond exists, and the CTE of diamond in the present investigation could therefore be validated to experimental values. It turned out to fit extraordinary well in the whole temperature range considering that this CTE is calculated from completely ab initio assumptions and the deviations do not exceed the spread in the datapoints. The CTEs of the Heusler alloys were also found. The Gibbs free energy and heat capacity were also calculated successfully. Due to instability of some of the structures more materials than originally planned were investigated, which led to the primary pyroelectric vector not being calculated because of the thesis deadline. From the CTEs and the piezoelectric tensors the secondary pyroelectric vector was found. It was however only $GaCuSe_2$ which had a phase where this was nonzero, but the other phase of this material was not stable within these calculations. Therefore, a large change in the pyroelectric vector due to a phase change was not found in this study. A phase change could not be found either, because only one phase of each material was stable. However, the method used works impressively well and that brings hope for the future in finding a pyroelectric material that can convert heat into power effectively. None of the calculations needed unattainable central processing unit (CPU) time. It was shown that the number of supercell calculations needed could be reduced drastically for the anisotropic systems.

In conclusion, the CTE, Gibbs free energy, the secondary pyroelectric vector and heat capacity have been found for diamond, $TiFe_2Si$, $GaNaTe_2$ and $GaCuSe_2$. Where there have been experimental results to compare with, the calculations have shown to give results that are close to these. The required CPU time has turned out to be significantly less than what could be expected from such advanced calculations, and the calculations in this work are highly attainable for both isotropic and anisotropic materials.

Preface

This master thesis makes up the last part of the study program “Materials Science and Nanotechnology” at the University of Oslo, started in the spring 2019 and ended in the autumn 2020. The thesis has background from the project COMET (Conversion between Magnetic, Electric and Thermal energies in phase-transforming materials) which is led by SINTEF and financed by the Research Council of Norway. The thesis will investigate phase-transforming materials that are pyroelectric.

I would like to give a huge thank you to my supervisor Ole Martin Løvvik who has given invaluable support during the whole process through weekly meetings, availability by questions through email and motivational attitude. Also, another thanks to Ole Martin for being supportive about me doing the study at part time when I was moving to Tønsberg to play ice hockey. Thanks to Nicholas Pike for making programs that were useful for me. I would also like to thank my dad for reading the thesis and giving highly valuable feedback when the deadline was closing in. Thanks to Osama Zariouh too for giving feedback on part of the thesis and helping me with formal demands. I would like to say many thanks to my family for always being supportive and helpful. At last, I would like to thank my friends and the people at structure physics for making the study life a little more fun.

Contents

1. Introduction

1.1. Goal of thesis

The goal of the task is to find a large change in the pyroelectric vector by a change in temperature. This will tell how effectively the material theoretically can produce electricity during heating. From the theoretical schemes by Born[9] and Szigeti[10]; to calculate the full pyroelectric coefficient, you need to calculate some other coefficients. These are:

1. The Born effective charge.
2. thermal expansion coefficients (CTE).
3. Piezoelectric coefficients.
4. Third-order force constants.
5. Thermodynamic properties at a given temperature.

So, the sub goals will be to calculate these.

1.2. Problem and hypothesis

The problem in this thesis will be to compute:

1. The CTE
2. The pyroelectric vector
3. The Gibbs free energy from ab initio calculations

The CTE is calculated because it is needed to calculate the secondary pyroelectric vector. These goals will be performed for a material that hopefully is a phase-transforming material (PTM) with bandgap in both phases. This will give a material that is able to produce electricity from heat and can reduce greenhouse gas through more energy efficient devices. The main hypothesis is that it is possible to calculate the CTE and the pyroelectric vector for a PTM. The secondary hypothesis supporting this are:

1. Calculation of the CTE, Gibbs free energy and the pyroelectric vector can be done very efficiently with the temperature dependent effective potential (TDEP) method.
2. All the algorithms being developed by our in-house code work properly for all solid materials which have not much more than eight atoms in the unit cell.
3. The CPU and memory requirements are not prohibitive to perform all the steps of the calculations required to achieve the pyroelectric coefficients.

1.3. Motivation for investigating phase-transforming materials

One of the hardest tasks these days is to deliver enough electricity without making too much impact on the environment. One very environment friendly approach is the direct conversion of heat to electricity, as it produces no waste products during use. This approach can increase efficiencies remarkable and also lead to new renewable heat sources, as it is a large and expanding area[11]. This is efficient because heat that is produced during a process which normally is not used to anything, can now produce electricity. It is like collecting energy that is lost in the process. Earlier, fluids and moveable compounds have been used for this but is now being challenged by solids, where the energy conversion happens inside the materials. Using solid-state heat engines instead may have a lot of potential benefits[12], but it can only be used in a small area because it is expensive, has low efficiency and has many system-dependent questions to answer[13]. The most known technology in this area is thermoelectricity[14]. This master thesis will however focus on phase-transforming materials instead, which change their electric and magnetic fields during phase transformation. The reason why such materials are more interesting is that PTMs have an efficient heat-conversion at temperature differences from 10 K to 100 K around the transition temperature. For this to happen, the change in the electric field must be large. The larger the better, as this gives larger electric field and more electrical current. This electric field will be large if the change in pyroelectric vector is large when going from one phase to the other. In the case of thermoelectric devices, the conversion is most efficient at a lot larger temperature differences, which is not always optimal.

1.4. Phase-transforming materials

Phase-transforming materials are materials that undergo structural phase transformations without diffusion of atoms. The phase transformation is due to external impact like stress or temperature. This leads to change in properties, which corresponds to a change in energy. Some changes that are important are the change in shape, change in magnetic field or change in electrical polarization. It is the last change that will be investigated as the pyroelectric effect.

1.5. Reversibility of Phase-transforming materials

The problem with phase-transforming materials, is often the reversibility. Fracture often occurs after a few cycles, the transformation temperature moves and fails completely in the end. The hysteresis can also be at a 70 K range, which makes the conversion efficiencies bad. But recently, a new PTM alloy that can go through many million cycles has just emerged[15, 16]. This alloy closely satisfies the "cofactor conditions" derived by Chen and James[17, 18] and theorized to be important to the reversibility of phase transformations. The first cofactor condition is that the middle eigenvalue of the transformation stretch tensor is 1[18]. This corresponds to restrictions on the lattice parameters of the two phases so that the interfaces between them don't generate stress. For this to be fulfilled, a martensitic phase transformation is required.

1.6. Pyroelectricity explained

The pyroelectric effect is defined as the temperature dependence of the spontaneous polarization in certain anisotropic solids[1]. Many pyroelectric materials do exist, as tourmaline, triglyne sulfate and lead zirconate[1]. The reason pyroelectric materials are interesting, is because they can be used to generate electricity through a change in temperature of the pyroelectric materials. One way to do that is given by the following. The unit cells in a pyroelectric crystal has a dipole moment[1]. If you cut a pyroelectric material such that it has parallel surfaces, and the parallel surfaces are perpendicular to the crystallographic symmetry axes, then the dipole moment of the unit cells will cause a spontaneous polarization perpendicular to the surfaces[1]. A spontaneous polarization is the dipole moment per unit volume[1]. This will be equal to having opposite charges on the two surfaces. If you then put electrodes on the surfaces and connects them with a wire, a circuit will flow if the spontaneous polarization changes. In most materials, an increase in temperature causes a decrease in spontaneous polarization[1], and current will flow. If the temperature decreases, the spontaneous polarization will decrease instead, and the electric current will flow in the opposite direction[1].

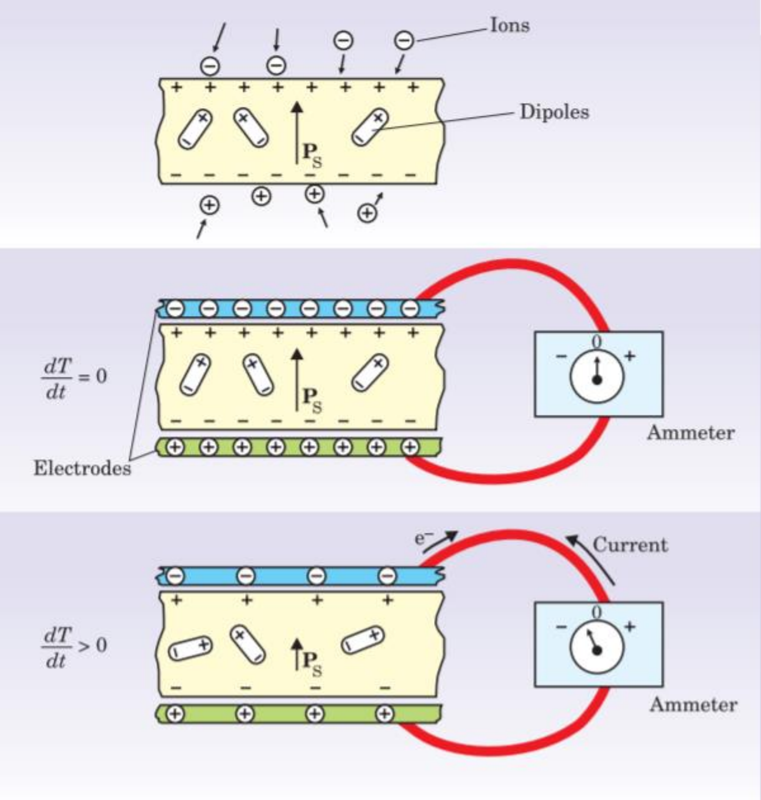

Figure 1: Illustration of the pyroelectric effect[1]. A pyroelectric material is attached to a circuit on the negative and positive charged surfaces. While the temperature T are constant, the electric dipole moment stays constant and no circuit flows. As the temperature changes, the dipole moment changes, and the charged particles moves through the circuit to compensate for the new surface charge.

1.7. Temperature dependent effective potential introduced

The TDEP package is a collection of programs to calculate finite temperature lattice dynamics. It contains programs as generate_structure, canonical configuration, extract_forceconstants, phonon_dispersion_relations and more. Along with VASP it can be used to calculate the pyroelectric coefficient amongst other properties from ab initio calculations. The coefficient of thermal expansion (CTE) is an important factor in the second term of the pyroelectric coefficient and has been calculated from ab initio assumptions using VASP and TDEP with great success. The results of Shulumba et. Al[19] who used DFT which is implemented in VASP, and TDEP to calculate the CTE, is shown in Figure 2. It shows how their theoretical line is within the experimental accuracy range for the temperatures experimental data exist.

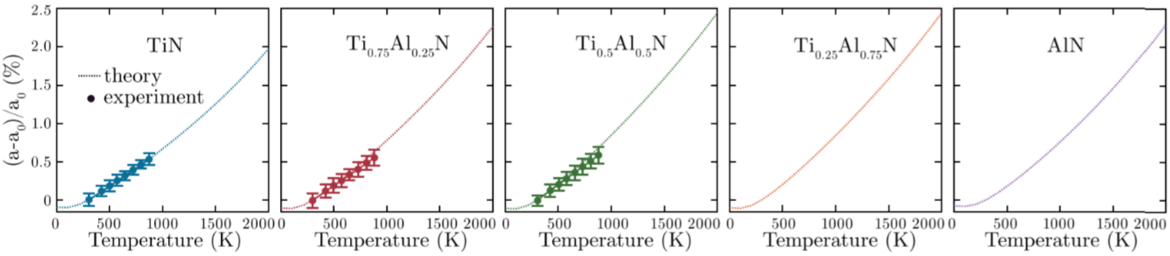

Figure 2: CTE of different combinations of $Ti_xAl_{1-x}N$ from the studies by Shulumba et al[19].

1.8. First principles pyroelectric vector

The pyroelectric vector has been calculated from first principles by Liu et al.[20] in 2016 and by Liu and Pantelides[21] in 2018 both for wurtzite GaN and ZnO. In 2016 they used the QUANTUM ESPRESSO package[22] within the local density approximation (LDA)[23] for electronic structure calculations and density functional perturbation theory (DFPT)[24] for calculations of the phonons. The third order anharmonic coefficients ($V_3\begin{pmatrix} 0 & \boldsymbol{q} & \boldsymbol{q} \\ j & \lambda & \lambda \end{pmatrix}$ in Equation 43) were calculated by displacing atoms along the displacement pattern $u_{\kappa\alpha}(\mathbf{0}\mathrm{j})$ from Equation 42 and taking the finite difference of the dynamical matrix from this. The pyroelectric vector is given by Equation 42 and Equation 45. The results of the 2016 work are shown in Figure 3 and Figure 4. In the 2018 article a third term was added which was supposed to account for the electron-phonon renormalization contribution. The results of this article are shown in Figure 5 and Figure 6.

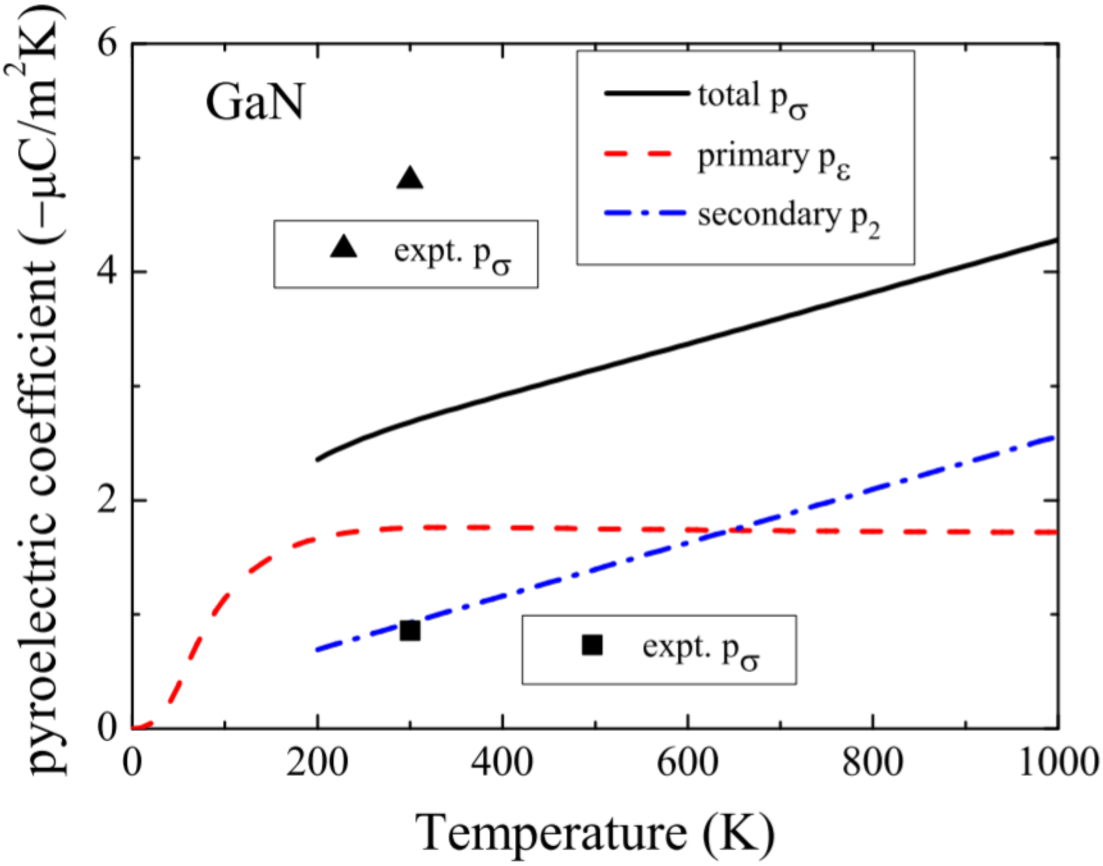

Figure 3: The pyroelectric coefficient of GaN from Liu et al.'s work[20]. The primary part equals the first term and the secondary equals the second term of the pyroelectric vector as described in theory of pyroelectricity. The triangle experimental value is from Matocha et al.[25] and the square experimental value is from Bykhovski[26].

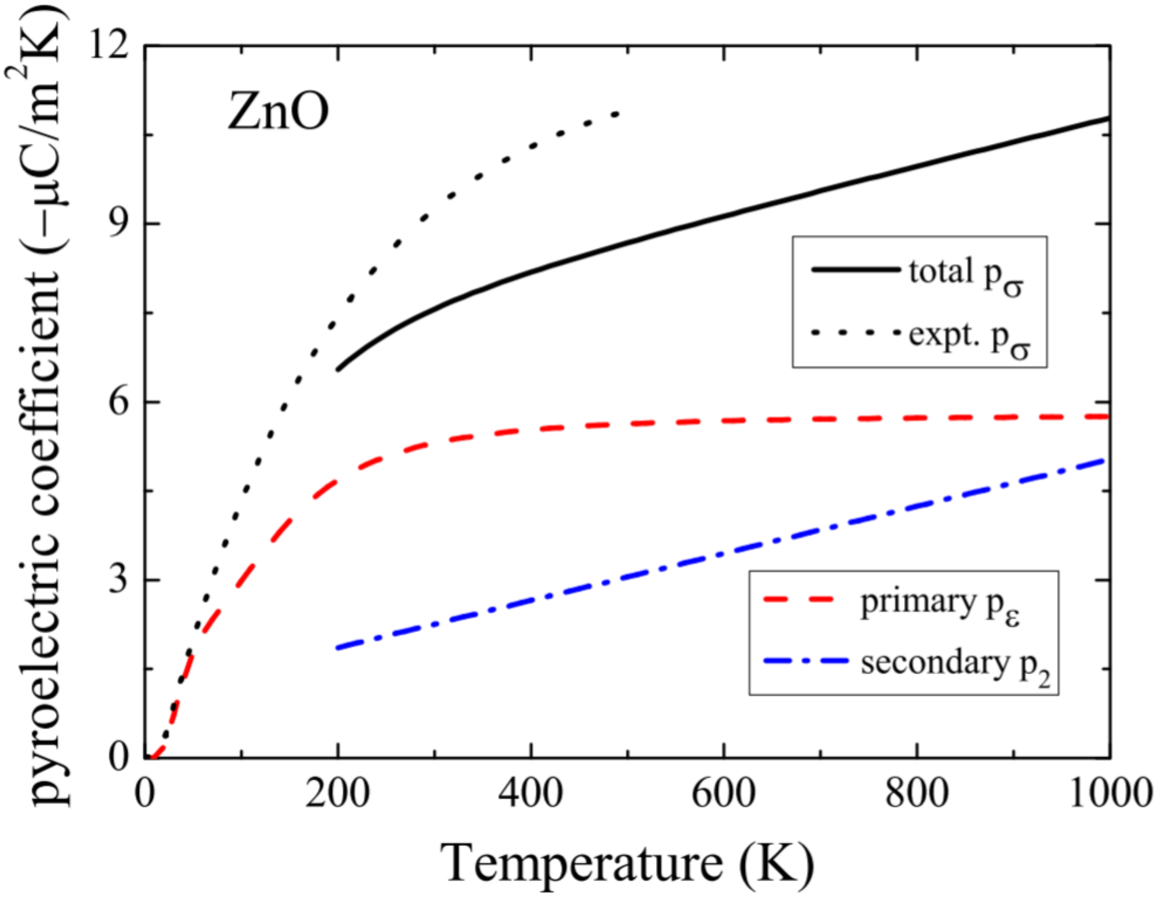

Figure 4: The pyroelectric coefficient of ZnO from Liu et al.'s work[20]. The experimental values are from Heiland and Ibach[27].

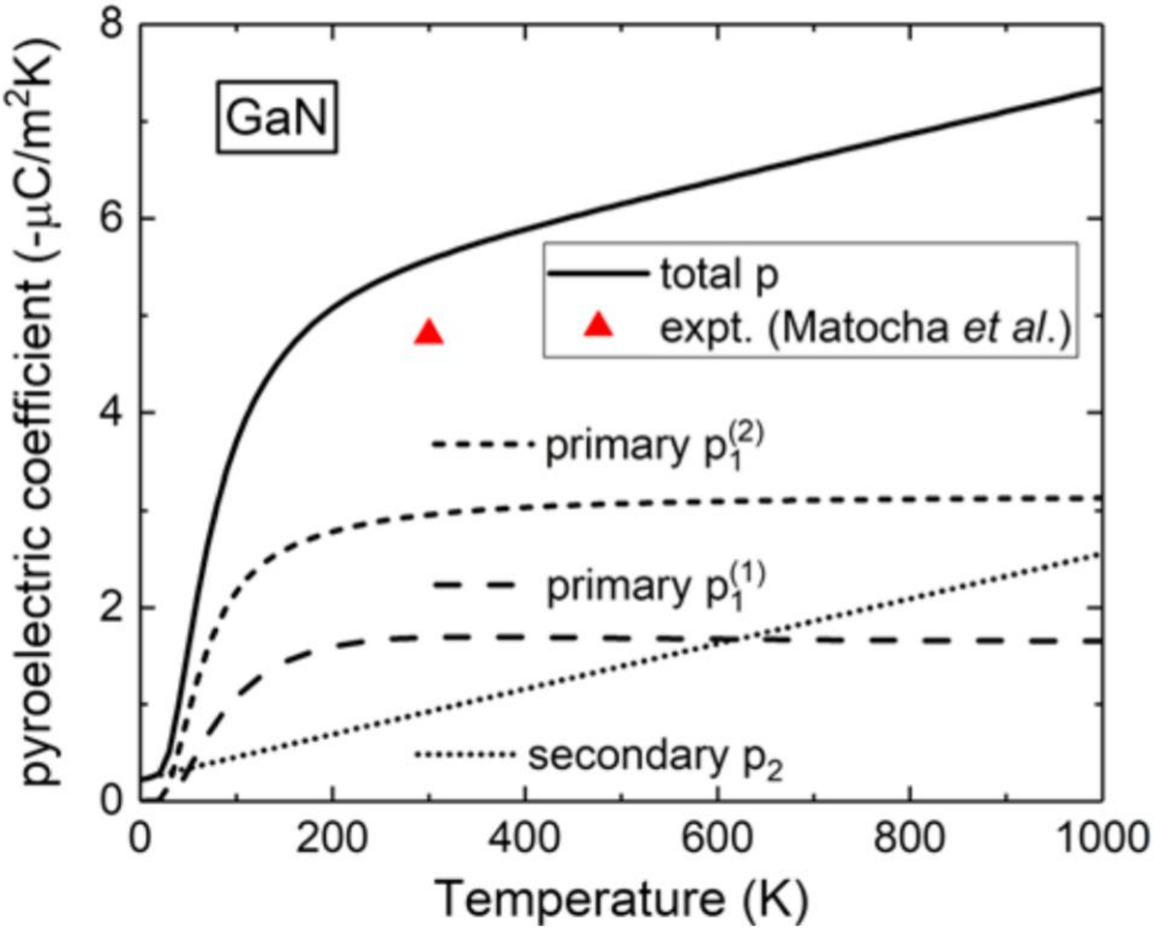

Figure 5: The pyroelectric coefficient of GaN from Liu and Pantelides work[21]. The experimental value is from Matocha et al.[25] The added term increases the pyroelectricity significantly and makes it a little higher than the experimental values.

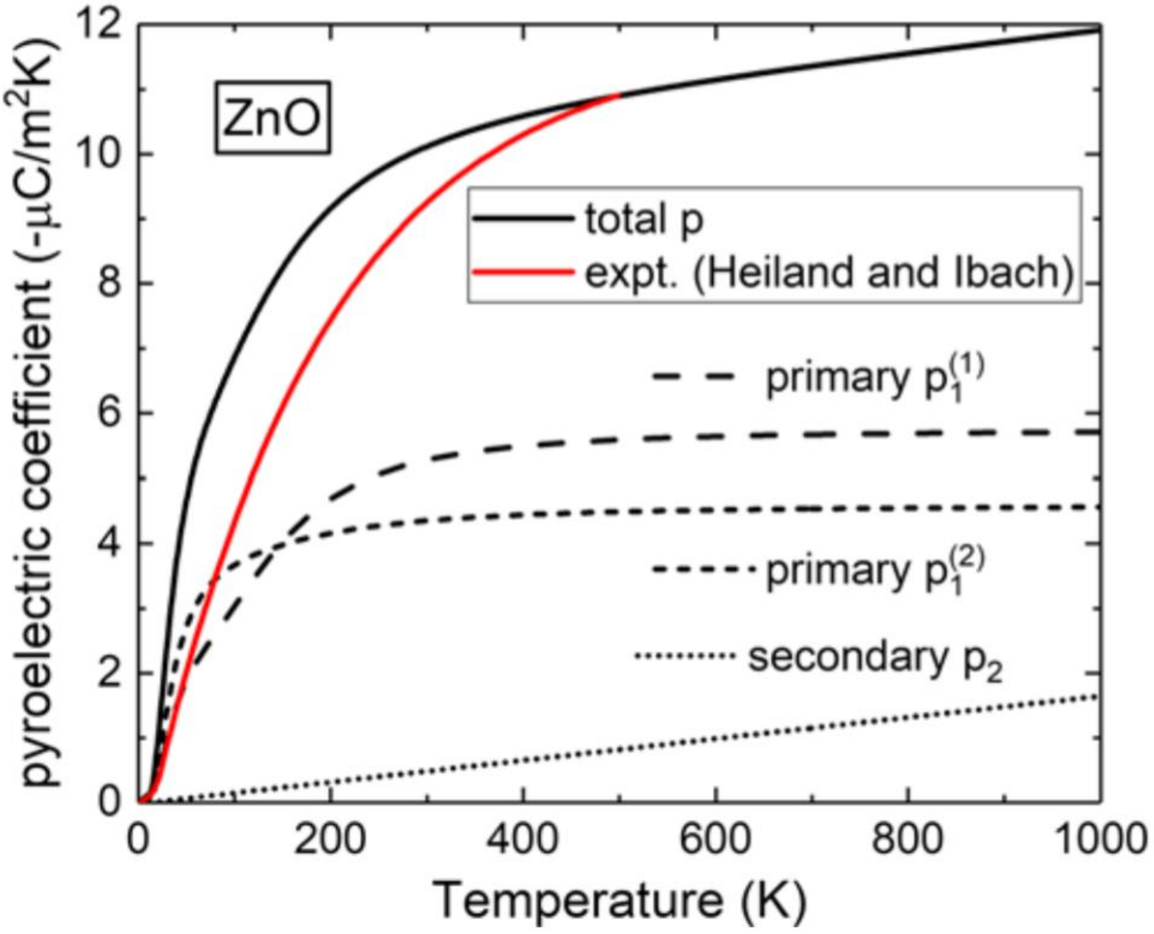

Figure 6: The pyroelectric coefficient of ZnO from Liu and Pantelides work[21]. The experimental line is from Heiland and Ibach[27]. The added term makes the total pyroelectric coefficient a little higher than the experimental values.

1.9. Materials investigated

In this thesis, there is searched for a material with nonzero piezoelectric tensor at low temperature and with zero piezoelectric tensor at high temperature, so that a phase change will give a large change in the pyroelectric vector. The material must have bandgap, else it cannot have a dipole moment. The materials investigated are presented here.

1.9.1. Diamond

Diamond was used just to demonstrate the method since it has a simple structure to work with and there is a lot of experimental data to compare with. It does not belong to a space group which lack inversion symmetry which is needed to have a non-zero piezoelectric tensor, which again is needed to have a nonzero secondary pyroelectric coefficient.

1.9.2. $TiFe_2Si$

One phase of $TiFe_2Si$ was investigated. That material has a Heusler structure and has space group $Fm\bar{3}m$ [225] with the titanium atoms at the (0,0,0) position and the silicon atoms at the (0.5,0.5,0.5) positions. $TiFe_2Si$ was originally the main material in this master thesis. Its cubic phase has bandgap which is needed for it to work as a pyroelectric material. It was supposed to be compared to a tetragonal or orthorhombic structure, but it was found that it was reported metastable[28]. Therefore, it was decided that it was not worth investigating another phase of this material.

1.9.3. $GaNaTe_2$

Two phases of $GaNaTe_2$ were investigated and both were tetragonal. The first structure of $GaNaTe_2$ is referred to as the α-structure and had space group $I\bar{4}2d$ $[122]$ with the Natrium atoms located at the positions (0,0,0) and (0.75,0.25,0.25) and the Gallium atoms located at (0.25,0.75,0.5) and (0.5,0.5,0). The second structure is referred to as the β-structure and had space group $I4/mcm$ $[140]$ with the natrium positions at (0.25,0.25,0) and (0.75,0.75,0) and the gallium positions at (0.25,0.75,0.5) and (0.75,0.25,0.5). $GaNaTe_2$ did originally have all the properties searched for. Two phases, one with a non-zero piezoelectric tensor and the other with a zero piezoelectric tensor and both structures with bandgap. However, the piezoelectric material turned out not being stable. Therefore, the secondary pyroelectric coefficient was again zero.

1.9.4. $GaCuSe_2$

Two phases of $GaCuSe_2$ were investigated, one tetragonal phase and one cubic phase. The tetragonal $GaCuSe_2$ had space group $I\bar{4}2d$ $[122]$ with the gallium atoms at (0.25,0.75,0.5) and (0.5,0.5,0) and the copper atoms at (0,0,0) and (0.75,0.25,0.5). The cubic $GaCuSe_2$ had the same space group as $TiFe_2Si$ with the gallium atoms at the silicon positions and the copper atoms at the titanium positions. The tetragonal $GaCuSe_2$ was the material in which a pyroelectric coefficient was found. It has bandgap, although low, the correct symmetry and it exists experimentally. The cubic phase of it was made from the structure of the $TiFe_2Si$, and it was not known if this phase actually existed. However, because it is an easy structure to deal with, it was considered to be worth investigating. It has the same symmetry as $TiFe_2Si$, its secondary pyroelectric vector is zero and could possibly with the tetragonal phase, be a system with all properties wanted. However, the cubic phase was also shown to be dynamically unstable.

2. Formalism

In this section the theory behind the CTEs and the secondary pyroelectric vector is explained. It starts with explaining DFT and VASP calculations. Density functional perturbation theory (DFPT), which is used by compared methods and when calculating the elastic tensor, is introduced. It is demonstrated how the elastic constants can be calculated and how those are further used by VASP and TDEP to calculate the force constants and free energies. The Birch-Murnaghan equation of state is introduced to show how the Helmholtz free energy can be found as a function of volume at constant temperature. It is explained how the Birch-Murnaghan equation of state can be used to calculate the Gibbs free energy as a function of pressure and temperature. The theory behind the pyroelectric vector is introduced.

2.1. Density functional Theory (DFT)

The time-independent nonrelativistic Schrödinger equation for a system of electrons affected by many nuclei can be written as[29]

$$\left[-\frac{\hbar^2}{2m}\sum_{i=1}^{N}\nabla_i^2+\sum_{i=1}^{N}V(\boldsymbol{r}_i)+\sum_{i=1}^{N}\sum_{j<i}U(\boldsymbol{r}_i,\boldsymbol{r}_j)\right]\Psi=E\Psi$$

Equation 1

where m is the electron mass, the first term is the kinetic energy of each electron, the second term is the affection on each electron from the collection of nuclei and the last term is the affection of the electrons on each other. Ψ is the wavefunction of the electrons and is a function of the spatial coordinates of each electron. So, for a system consisting of 10000 electrons, Ψ is a function of 30000 variables. E is the ground state energy of the electrons.

Density functional theory is based on two theorems by Kohn and Hohenberg[30, 31]. The first theorem is as follows; "The ground-state energy from Schrödinger's equation is a unique functional of the electron density"[31]. It states that there is a one-to-one mapping between density of the electrons and their wavefunction in the ground-state, which further means that all ground-state properties are decided by the electron density of the ground-state[31]. The second theorem states; "The electron density that minimizes the energy of the overall functional is the true electron density corresponding to the full solution of the Schrödinger equation"[31]. So the true electron density could be found if the true functional was known, by varying the density until the minimum energy was found[31]. This is very useful, since this means that the original $3*N$ dimensional problem where N is the number of electrons, can be reduced to a three-dimensional problem if the functional was known.

The electronic wavefunction $\Psi = \Psi(\boldsymbol{r}_1,\ldots,\boldsymbol{r}_N)$ can be approximated by $\Psi = \Psi_1(\boldsymbol{r})\Psi_2(\boldsymbol{r}),\ldots,\Psi_N(\boldsymbol{r})$, where Ψ_i is the wavefunction for the i'th single electron[29]. This approximation is known as the Hartree product[29]. Further the density can be approximated by these single electron wave functions as[30]

$$n(\boldsymbol{r})=2\sum_i\psi_i^*(\boldsymbol{r})\psi_i(\boldsymbol{r})$$

Equation 2

This is used by Kohn and Sham who proved that the correct electron density can be found solving a set of equations which only includes one electron each[32]. This expression is[32]

$$\left[-\frac{\hbar^2}{2m}\nabla^2 + V_{total}(\boldsymbol{r})\right]\psi_i\,(\boldsymbol{r}) = \varepsilon_i\psi_i(\boldsymbol{r})$$

Equation 3

Where $\psi_i(\boldsymbol{r})$ is the wavefunction of the *i*'th electron, ε_i is its energy and V_{total} is

$$V_{total}(\boldsymbol{r}) = V(\boldsymbol{r}) + V_H(\boldsymbol{r}) + V_{XC}(\boldsymbol{r}).$$

Equation 4

The first term is the kinetic energy of the electron, the second term is the interaction between the electron and all nuclei. The third term is the interaction between the electron and all electrons and is given as[33]

$$V_H(\boldsymbol{r}) = e^2 \int \frac{n(\boldsymbol{r}')}{|\boldsymbol{r}-\boldsymbol{r}'|} d^3r'.$$

Equation 5

It is called the Hartree potential and includes a self-interaction error because the electron considered is included in the electron density[33]. This error is corrected in the exchange-correlation potential V_{XC}[33]. This potential is not known and has to be approximated by a model[34].

There have been several attempts to approximate the exchange-correlation potential[35]. However, there exists a system where it is known perfectly[34]. The free electron gas. This is not a very physical system, since it is the interaction between electrons and nuclei that makes the species. But it gives decent results. In a free electron gas, the density is constant. Using the exact free electron gas exchange-correlation and the local density is called the local density approximation (LDA)[35]. Further the generalized gradient approximation (GGA) uses information about the gradient of the local density in addition[35]. There are several different GGA functionals since there are many ways the gradient of the electron density can be used[35].

As seen in the expression for the Hartree potential, an initial density is needed to solve the Kohn-Sham equations. Once the Kohn-Sham equations is solved, a new density can be made from Equation 2. If this density is the same as the one used to solve the Kohn-Sham equations, this density corresponds to the ground state. If it does not, the density need to be adjusted somehow. With the adjusted density, the Kohn-Sham equations can again be solved and the calculations starts all over again until the self-consistent density is found[33, 34].

2.2. Vienna ab initio simulation package (VASP)

Vienna *ab initio* simulation package (VASP) is a package that contains algorithms which has succesfully calculated the Kohn-Sham ground state of many different systems using pseudopotentials and a plane-wave basis set[5]. It solves the Kohn-Sham equations by two independent calculations. The first one is to find the eigenenergies and the eigenfunctions while the other is to find the density[5].

2.3. Density functional perturbation theory (DFPT)

The Kohn-Sham equations from Equation 3 is used in DFT. However, if there is a periodic perturbation potential V_p, the potential V_{total} will get an additional term V_{total}^p and

from nondegenerate first order perturbation theory[36] the first order equation will look like this

$$\left(-\frac{\hbar^2}{2m}\nabla^2 + V_{total}(\boldsymbol{r}) - \varepsilon_i\right)\psi_i^p(\boldsymbol{r}) = \left(\langle\psi_i(\boldsymbol{r})|V_{total}^p(\boldsymbol{r})|\psi_i(\boldsymbol{r})\rangle - V_{total}^p(\boldsymbol{r})\right)\psi_i(\boldsymbol{r}).$$

Equation 6

Linearizing the original Kohn-Sham equations V_{total}^p can be obtained as[37]

$$V_{total}^p = V_p(\boldsymbol{r}) + e^2\int\frac{n_p(\boldsymbol{r}')}{|\boldsymbol{r}-\boldsymbol{r}'|}d\boldsymbol{r}' + n_p(\boldsymbol{r})\left[\frac{dV_{xc}}{dn}\right]_{n=n_0(\boldsymbol{r})}$$

Equation 7

where n_p is the linear modification of the electron density and n_0 is the electron density resulting from the original Kohn-Sham equations. n_p can be written as[38]

$$n_p(\boldsymbol{r}) = 2\,Re\sum_i \psi_i^*(\boldsymbol{r})\psi_i^p(\boldsymbol{r})\Theta(\epsilon_F - \epsilon_i)$$

Equation 8

where Θ is the occupation function and ϵ_F is the fermi energy. These equations can be solved self-consistently after the unperturbed problem is solved by starting with a trial n_p and then solve Equation 6 until a self-consistent density is found.

2.4. Calculation of Elastic tensor

The elastic tensor is defined, as seen from Equation 9, from the stress tensor and the strain tensor[39]

$$\sigma_i = \sum_{j=1}^{6} C_{ij}\epsilon_j.$$

Equation 9

Here σ_i is the *i*'th component of the stress tensor, ϵ_j is the *j*'th component of the stress tensor and C is the elastic tensor. There are six independent components of the strain tensor, as it is a symmetric 3x3 tensor[40]. The components of it is just the distortion of a point from the original structure in the different directions and can be easily controlled. There are six independent stress components by the same reason as for the strain tensor[41]. These components are forces per unit area in different directions[42] and can be calculated from DFPT calculations within VASP. The elastic tensor can be considered as a 6x6 matrix. This is also symmetric which gives it 21 independent components[43]. Equation 9 therefore gives six equations with 21 unknown variables. Solving this equation can be done using IBRION 6 and ISIF >= 3 in VASP. This generates six configurations of the original structure with only one strain component present for each configuration and so that all strain components are generated[39]. Then the stresses are calculated for each configuration[39]. Each configuration will make it possible to solve six components of the elastic tensor[39]. The method described for the elastic tensor is valid for the triclinic case, which means that it holds for all other cases too.

2.5. Calculation of Debye temperature from elastic tensor

The elastic coefficients can be used to find the bulk moduli (B) and the shear moduli (G). They are given by

$$B = \frac{1}{9}\left((C_{11} + C_{22} + C_{33}) + 2(C_{12} + C_{31} + C_{23})\right)$$

Equation 10

and

$$G = \frac{1}{15}\big((C_{11} + C_{22} + C_{33}) - (C_{12} + C_{31} + C_{23}) + 3(C_{44} + C_{55} + C_{66})\big).$$

Equation 11

These can again be used to find the longitudinal (v_l) and shear (v_s) sound velocities as[44]

$$v_l = \sqrt{\frac{B + \frac{4}{3}G}{\rho}}$$

Equation 12

and

$$v_s = \sqrt{\frac{G}{\rho}}$$

Equation 13

where ρ is the materials density. From the longitudinal and shear sound velocities, the Debye temperature can be calculated as[45]

$$\Theta_\mathrm{D} = \frac{h}{k_B}\left(\frac{9m}{4\pi}\right)^{\frac{1}{3}}\left(\frac{1}{v_l^3} + \frac{2}{v_s^3}\right)^{-\frac{1}{3}}$$

Equation 14

2.6. Force constants from Debye temperature

Force constants are used to generate the canonical configurations[46]. This is done by Shulumba et al.'s method[46]. They are using a pair potential *U(r)* that must fulfil two needs:

$$\frac{\partial U(r)}{\partial r_{ij}} = 0,$$

Equation 15

$$\frac{\partial^2 U(r)}{\partial r_{ij}^2} = \frac{\eta}{r^4}.$$

Equation 16

The first precondition is that the potential must be zero at pair distances of the equilibrium crystal and the second is that the second derivatives should be positive and decrease quickly with increasing distance. As these preconditions are fulfilled, the crystal is forced to be stable in this configuration. From these pair potentials the force constants are calculated analytically as

$$\Phi_{ij}(\boldsymbol{r}) = -\frac{\eta}{r^6}\begin{pmatrix} r_x^2 & r_x r_y & r_x r_z \\ r_x r_y & r_y^2 & r_y r_z \\ r_x r_z & r_y r_z & r_z^2 \end{pmatrix},$$

Equation 17

where ***r*** is the vector between atom *i* and *j*. In this method, the force constants are given by η alone which is given by numerically matching the zero-point energy of the phonons to a Debye model,

$$\frac{1}{N_a}\sum_i \frac{\hbar\omega_i(\eta)}{2} = \frac{9k_B T_D}{8},$$

Equation 18

where T_D is the Debye temperature and ω_i is the phonon eigenfrequencies.

2.7. Frequencies

The frequencies are found by solving the eigenequation[47]

$$\omega^2(\boldsymbol{k},\nu)\boldsymbol{e}(\boldsymbol{k},\nu) = \boldsymbol{D}(\boldsymbol{k})\boldsymbol{e}(\boldsymbol{k},\nu),$$

Equation 19

where ***e*** is a 3*n* vector which consists of the displacements of the atoms weighted by the square root of the atomic mass and equals[47]

$$\boldsymbol{e}(\boldsymbol{k},\nu) = \begin{pmatrix} \sqrt{m_1}U_x(1,\boldsymbol{k},\nu) \\ \sqrt{m_1}U_y(1,\boldsymbol{k},\nu) \\ \sqrt{m_1}U_z(1,\boldsymbol{k},\nu) \\ \sqrt{m_2}U_x(2,\boldsymbol{k},\nu) \\ \vdots \\ \sqrt{m_n}U_z(n,\boldsymbol{k},\nu) \end{pmatrix}.$$

Equation 20

In this expression m_1 is the mass of atom 1 and so on up to atom *n*, $U_x(1,\boldsymbol{k},\nu)$ is the displacement vector in direction *x* of atom 1. *n* is the number of atoms per unit cell. ***D*** is the dynamical matrix which is a $3n\ x\ 3n$ which is written as a $n\ x\ n$ matrix of $3\ x\ 3$matrices. The elements of the $3\ x\ 3$ matrices are given by[48]

$$D_{\alpha\beta}(j,j',\boldsymbol{k}) = \frac{1}{(m_j m_{j'})^{\frac{1}{2}}}\sum_{l'} \phi_{\alpha\beta}\begin{pmatrix} jj' \\ 0l' \end{pmatrix} \exp(i\boldsymbol{k}[\boldsymbol{r}(j'l') - \boldsymbol{r}(j0)]),$$

Equation 21

where *α, β* is the cartesian directions *x, y, z*, $\phi\begin{pmatrix} jj' \\ 0l' \end{pmatrix}$ is the force constant of atom *j* in the reference unit cell 0 and atom *j'* in unit cell *l'*.

2.8. Canonical configurations

The canonical configurations are snapshots of the supercell at a given temperature[46]. The distribution of the atoms was first given by West and Estreicher[49] and is found by using a harmonic normal mode transformation to generate positions u_i and velocities $\dot{u}_i$ given by[46]

$$u_i = \sum_{s=1}^{3N_a} \epsilon_{is}\langle A_{is}\rangle\sqrt{-2\ln\xi_1}\sin 2\pi\,\xi_2,$$

Equation 22

$$\dot{u}_i = \sum_{s=1}^{3N_a} \omega_s\epsilon_{is}\langle A_{is}\rangle\sqrt{-2\ln\xi_1}\cos 2\pi\xi_2.$$

Equation 23

Here ω_s^2 and ϵ_{is} are eigenvalues and eigenvectors of the dynamical matrix corresponding to mode s and atom i. ξ_n represent uniform random variables between zero and one, and $\langle A_{is}\rangle$ are the thermal average of the normal mode amplitudes[49]:

$$\langle A_{is}\rangle = \frac{1}{\omega_s}\sqrt{\frac{k_B T}{m_i}},$$

Equation 24

where $\hbar\omega \ll k_B T$ is in the classical limit and this approximation for the amplitude is valid.

2.9. Force constants from canonical configurations

The following description of TDEP comes from Hellman's articles about TDEP[6-8]. In the TDEP method, a model Hamiltonian is introduced,

$$H_{model} = U_0 + \sum_i \frac{\boldsymbol{p}_i^2}{2m_i} + \frac{1}{2!}\sum_{ij\sigma\rho} \phi_{ij}^{\sigma\rho} u_i^\sigma u_j^\rho + \frac{1}{3!}\sum_{ijk\sigma\rho\xi} \psi_{ijk}^{\sigma\rho\xi} u_i^\sigma u_j^\rho u_k^\xi,$$

where U_0 is the potential of the static lattice. $\boldsymbol{p}_i$, u_i and m_i are the momentum, the displacement and the mass of the i'th atom respectively. σ, ρ and ξ denotes cartesian directions, and φ and ψ are the second and third order force constants respectively. This model Hamiltonian can be set equal to the Hamiltonian from Born-Oppenheimer molecular dynamics at a given temperature. This is done within TDEP by minimizing the difference of the forces from the model Hamiltonian and the forces from Born-Oppenheimer. Since there is a lot of force constants, symmetry reduction is vital, at least for force constants of higher order. The symmetry relations are[7, 50]

$$\phi_{ij}^{\sigma\rho} = \phi_{ji}^{\rho\sigma}$$

Equation 25

$$\psi_{ijk}^{\sigma\rho\xi} = \psi_{ikj}^{\sigma\xi\rho} = \psi_{jik}^{\rho\sigma\xi} = \psi_{jki}^{\rho\xi\sigma} = \psi_{kij}^{\xi\sigma\rho} = \psi_{kji}^{\xi\rho\sigma}.$$

Equation 26

For tensors that are related by symmetry operation S, their components are related by

$$\phi_{ij}^{\sigma\rho} = \sum_{\alpha\beta} \phi_{kl}^{\alpha\beta} S^{\alpha\sigma} S^{\beta\rho}$$

Equation 27

$$\psi_{ijk}^{\sigma\rho\xi} = \textstyle\sum_{\alpha\beta\gamma} \psi_{lmn}^{\alpha\beta\gamma} S^{\alpha\sigma} S^{\beta\rho} S^{\gamma\xi}.$$

Equation 28

The acoustic sum rules will also be obeyed by the force constants

$$\sum_j \boldsymbol{\phi}_{ij} = 0,$$

Equation 29

and

$$\sum_{k} \boldsymbol{\psi}_{ijk} = 0,$$

Equation 30

where $\boldsymbol{\phi}_{ij}$ and $\boldsymbol{\psi}_{ijk}$ are the force tensors which consist of all directional components.

The forces resulting from the model Hamiltonian can be expressed as

$$F_i^{\sigma} = \sum_{j\rho} \phi_{ij}^{\sigma\rho} u_j^{\rho} + \frac{1}{2} \sum_{jk\rho\xi} \psi_{ijk}^{\sigma\rho\xi} u_j^{\rho} u_k^{\xi}$$

Equation 31

and by introducing θ_k as the irreducible force constants the forces are

$$F_i^{\sigma} = \sum_{k} \theta_k c_{ki}^{\sigma} (\boldsymbol{U})$$

Equation 32

where $c_{ki}^{\sigma}(\boldsymbol{U})$ is a polynomial function of all the atoms within a cutoff radius r_c and depends on the atoms and the structure of the material. For a supercell of the material, the forces can be collected into a matrix and represented as a matrix equation:

$$\boldsymbol{F}_{model} = \boldsymbol{C}(\boldsymbol{U})\boldsymbol{\Theta}.$$

Equation 33

C is a matrix that holds the elements of c_{ki}^{σ} in Equation 32 and is then a function of all the displacements in the supercell, while $\boldsymbol{\Theta}$ is a vector that consists of all the θ_k. $\boldsymbol{F}_{model}$ is the matrix that consists of all the forces from the model Hamiltonian. As the forces from the model Hamiltonian are expressed, it can be compared to the forces from the Born-Oppenheimer molecular dynamics. The forces from the molecular dynamics are calculated from different canonical configurations of the supercell[46]. All these along with the displacements will be used to overdetermine the force constants from the model. They are determined by minimizing the difference between the forces from molecular dynamics and the forces from the model:

$$\Delta \boldsymbol{F} = \frac{1}{N_c} \sum_{c=1}^{N_c} |\boldsymbol{F}_{MD}^{c} - \boldsymbol{F}_{model}^{c}|^2 = \frac{1}{N_c} \sum_{c=1}^{N_c} |\boldsymbol{F}_{MD}^{c} - \boldsymbol{C}(\boldsymbol{U}_{MD}^{c})\boldsymbol{\Theta}|^2 = \frac{1}{N_c} \left\| \begin{pmatrix} \boldsymbol{F}_{MD}^{1} \\ \vdots \\ \boldsymbol{F}_{MD}^{N_c} \end{pmatrix} - \begin{pmatrix} \boldsymbol{C}(\boldsymbol{U}_{MD}^{1}) \\ \vdots \\ \boldsymbol{C}(\boldsymbol{U}_{MD}^{N_c}) \end{pmatrix} \boldsymbol{\Theta} \right\|^2 .$$

Equation 34

In Equation 34, N_c is the number of configurations used, and the subscript c corresponds to configuration c. Differentiating with respect to $\boldsymbol{\Theta}$ gives that

$$\boldsymbol{\Theta} = \begin{pmatrix} \boldsymbol{C}(\boldsymbol{U}_{MD}^{1}) \\ \vdots \\ \boldsymbol{C}(\boldsymbol{U}_{MD}^{N_c}) \end{pmatrix}^{+} \begin{pmatrix} \boldsymbol{F}_{MD}^{1} \\ \vdots \\ \boldsymbol{F}_{MD}^{N_c} \end{pmatrix}$$

Equation 35

is the $\boldsymbol{\Theta}$ that minimizes the forces. By substituting back to $\boldsymbol{\phi}_{ij}$ and $\boldsymbol{\psi}_{ijk}$ the quadratic and cubic force constants are determined. So, both orders of force constants can be determined at the same time.

2.10. Quasiharmonic approximation

In the quasiharmonic approximation the Helmholtz free energy F which is the free energy at constant volume is given by[51]

$$F = E_0 + \frac{1}{2}\sum_{\boldsymbol{k},\nu} \hbar\omega(\boldsymbol{k},\nu) + k_B T \sum_{\boldsymbol{k},\nu} \ln\left[1 - exp\left(-\frac{\hbar\omega(\boldsymbol{k},\nu)}{k_B T}\right)\right].$$

Equation 36

Here E_0 is the potential energy of the crystal, $\boldsymbol{k}$ is the wavevector, v is the mode of the wavevector, ω is the frequency of wavevector $\boldsymbol{k}$ and mode v and T is the temperature. The two last terms are referred to as the vibrational free energy.

2.11. Birch-Murnaghan equation of state

The Birch-Murnaghan equation of state relates the volume and pressure of a body using strain components up to third order[52]. The equation is given by[52]

$$P(V) = \frac{3B}{2}\left[\left(\frac{V_0}{V}\right)^{\frac{7}{3}} - \left(\frac{V_0}{V}\right)^{\frac{5}{3}}\right]\left[1 + \frac{3}{4}(B' - 4)\left(\left(\frac{V_0}{V}\right)^{\frac{2}{3}} - 1\right)\right]$$

Equation 37

where P is the pressure, B is the bulk modulus, V_0 is the reference volume, V is the volume caused by the pressure and B' is the derivative of the bulk modulus with respect to pressure. The Helmholtz free energy, $E(V)$, can be found by integrating the pressure and is given by[52]

$$E(V) = E_0 + \frac{9V_0B_0}{16}\left[\left(\left(\frac{V_0}{V}\right)^{\frac{2}{3}} - 1\right)^3 B_0' + \left(\left(\frac{V_0}{V}\right)^{\frac{2}{3}} - 1\right)^2 \left(6 - 4\left(\frac{V_0}{V}\right)^{\frac{2}{3}}\right)\right].$$

Equation 38

2.12. Gibbs free energy

The pressure can be calculated by[53]

$$P = -\left(\frac{\partial F}{\partial V}\right)_T,$$

Equation 39

where F is the Helmholtz free energy. This expression for pressure is equivalent to Equation 37 setting the Helmholtz free energy equal to Equation 38. From this the Gibbs free energy, G, can be calculated from[54]

$$G = F + PV.$$

Equation 40

From this it is seen that at zero pressure the Gibbs free energy equals the Helmholtz free energy. The Gibbs free energy decides what phase is stable at the given temperature and pressure. For two phases of a material it is the one with lowest Gibbs free energy that is the stable one and the phase the material goes to if it is not hindered.

2.13. Pyroelectric coefficient

The pyroelectric vector represents how the macroscopic dipole moment $\boldsymbol{P}$ changes with respect to temperature[10]. This can be expressed at constant stress σ as[10]

$$\left(\frac{dP^{\beta}}{dT}\right)_{\sigma} = \left(\frac{\partial P^{\beta}}{\partial T}\right)_{\rho} + \sum_{i}\left(\frac{\partial P^{\beta}}{\partial s_{\alpha}}\right)_{T}\left(\frac{\partial s_{\alpha}}{\partial T}\right)_{\sigma} = p_1^{\beta}(T) + p_2^{\beta}(T),$$

Equation 41

where P^{β} is the β component of the macroscopic dipole moment, ρ indicates constant strain, s_{α} is the α component of the macroscopic strain tensor that have full crystalline symmetry, α and β are the cartesian directions, T is the temperature, p_1 is the primary pyroelectricity and p_2 is the secondary pyroelectricity. The primary part is the contribution at constant strain and is given to first order by[20, 55]

$$p_1^{\beta}(T) = \frac{e}{\Omega}\sum_{j,\kappa\alpha} Z_{\kappa}^{\beta\alpha}\left(\frac{\langle \partial u_{\kappa\alpha}(\boldsymbol{0}\nu)\rangle}{\partial T}\right),$$

Equation 42

where e is the elementary charge, Ω is the temperature dependent volume of the unit cell, Z_{κ} is the Born effective charge of the κ atom, $u(\boldsymbol{0}j)$ is the displacement given mode ν of the phonon momentum at $\boldsymbol{q} = \boldsymbol{0} = (0,0,0)$. The derivative factor can further be written as[20, 56]

$$\left(\frac{\langle \partial u_{\kappa\alpha}(\mathbf{0}\nu)\rangle}{\partial T}\right) = \frac{2}{\hbar\omega_{\mathbf{0}\nu}}\sqrt{\frac{\hbar}{2M_{\kappa}\omega_{\mathbf{0}\nu}}}\,\epsilon_{\kappa\alpha}(\mathbf{0}\nu)\sum_{\boldsymbol{q}\lambda} V_3\begin{pmatrix}\mathbf{0} & \boldsymbol{q} & -\boldsymbol{q}\\ \nu & \lambda & \lambda\end{pmatrix}\frac{\partial\left(2n_{\boldsymbol{q}\lambda}+1\right)}{\partial T},$$

Equation 43

where $\hbar$ is Planck's constant divided by 2π, $\omega_{\boldsymbol{0}\nu}$ is the frequency of the phonon at momentum point $\mathbf{0}$ and mode ν, M_{κ} is the mass of atom κ, $\epsilon_{\kappa\alpha}(\boldsymbol{0}j)$ is the normalized α component of the $(\boldsymbol{0}\nu)$ eigenvector of the harmonic dynamical matrix of atom κ, $n_{\boldsymbol{q}\lambda}$ is the Bose occupation factor and V_3 is[20, 56]

$$V_3\begin{pmatrix}\mathbf{0} & \boldsymbol{q} & \boldsymbol{q}\\ \nu & \lambda & \lambda\end{pmatrix} = \sum_{\kappa_0\kappa_1\kappa_2,\alpha_0\alpha_1\alpha_2,l_1l_2}\sqrt{\frac{\hbar^3}{8M_{\kappa_0}M_{\kappa_1}M_{\kappa_2}\omega_{\mathbf{0}\nu}\omega_{\boldsymbol{q}\lambda}\omega_{-\boldsymbol{q}\lambda}}}\,\epsilon_{\kappa_0\alpha_0}(\mathbf{0}j)\epsilon_{\kappa_1\alpha_1}(\boldsymbol{q}\lambda)\epsilon_{\kappa_2\alpha_2}(-\boldsymbol{q}\lambda)\left(\frac{\partial^3 E}{\partial u_{\kappa_0\alpha_0}^{l_0}\partial u_{\kappa_1\alpha_1}^{l_1}\partial u_{\kappa_2\alpha_2}^{l_2}}\right)e^{i\boldsymbol{q}(\boldsymbol{\tau}_{l_1}-\boldsymbol{\tau}_{l_2})}$$

Equation 44

where E is the energy and its third derivatives are the third order force constants, and $\boldsymbol{\tau}_{l_1}$ and $\boldsymbol{\tau}_{l_2}$ are position vectors of the two atoms in the triplet that is not atom zero. The second order primary part which is the electron-phonon renormalization contribution is not considered in this study[21].

The secondary part is caused by the unit cell expanding, and is given as[20, 21, 56]

$$p_2^{\beta}(T) = \gamma_{\beta\alpha}\frac{ds_{\alpha}}{dT}$$

Equation 45

where $\gamma_{\beta\alpha}$ is the $\beta\alpha\alpha$ component of the piezoelectric tensor and $\frac{ds_{\alpha}}{dT}$ equals the CTEs of material.

2.14. Summary of the formalism

The theory behind the methods is now presented. The idea is to use VASP and TDEP to calculate the free energy as a function of temperature and lattice parameters. From there, by minimizing the energy as a function of lattice parameters at each temperature, the lattice parameters are found as a function of temperature. TDEP calculates the phonon eigenfrequencies at a given temperature, then uses the quasiharmonic approximation to calculate the vibrational free energy at all temperatures. The CTEs is straight forwardly calculated from the lattice parameters vs temperature. The piezoelectric tensor and born effective charges are calculated in the calculations where DFPT is used. The force constants are calculated from TDEP. From this the pyroelectric vector can be calculated.

3. Method

The method started with finding a proper energy cutoff for the plane wave basis set and the k-point density. Then the equilibrium structures were found and used for further calculations. Calculations to find the elastic and piezoelectric tensors amongst others were done. From the elastic tensor the Debye temperature was found, and the first set of canonical configurations were made with TDEP. From VASP calculations of these configurations, the assumed correct force constants of the equilibrium structure were found. The vibrational free energy was converged with respect to number of configurations, cutoff radius of atoms included in the calculations and the Debye temperature. From the assumed correct force constants, canonical configurations of cells with expanded and compressed lattice parameters were made and total energy calculations of these were performed. The vibrational free energy and the heat capacity as a function of temperature for each lattice parameters were found. Total energy calculations of the expanded and compressed unit cells were also done. From the total energy calculations and the vibrational free energy, the energy as a function of volume were minimized to find the lattice parameters and CTEs as a function of temperature. The number of volumes needed to find the CTEs was reduced drastically. The third order force constants were investigated, and the heat capacity was also minimized at each temperature. The Gibbs free energy as a function of pressure was found from Birch-Murnaghan equation of state and the secondary pyroelectric vector was found from Equation 45.

3.1. Convergence with respect to energy cutoff

First convergence of relative energy, pressure, force and bandgap were checked with respect to energy cutoff for the planewave basis set in eV and k-point density. By relative energy it means the absolute value of the difference of the energies from two comparable species. For the $TiFe_2Si$ system it was between one formula unit of Heusler $TiFe_2Si$ and one formula unit of orthorhombic $TiFeSi_2$. $TiFeSi_2$ was used because it is a material with cheap atoms to do calculations for. For diamond it was between one carbon atom in its original structure and one carbon atom in a structure with the atom at the origin slightly displaced 0.02 Å along the first translation vector. For $GaNaTe_2$ it was between α-$GaNaTe_2$ and β -$GaNaTe_2$. For tetragonal $GaCuSe_2$ it was between one formula unit of the original structure and one formula unit of the structure with a cupper atom displaced 0.02 Å along the first translation vector. For cubic $GaCuSe_2$ it was between one formula unit of its structure and one formula unit of the tetragonal phase. The convergence criterions for TiFeSi system, $GaNaTe_2$ and $GaCuSe_2$ was that relative energy should change less than 1 meV, pressure less than 3 kbar, force less than 0.005 eV/Å and band gap less than 0.01 eV. For diamond the convergence criterions were the same for relative energy and force, but pressure should change less than 17.5 kbar and bandgap less than 0.02 eV. These changes are for a change in energy cutoff of 50 eV.

The convergence criterion was fulfilled for diamond with energy cutoff at 400 eV, while it was fulfilled when the energy cutoff was at 450 eV for the TiFeSi system. For $GaNaTe_2$ all criterions were fulfilled for a cutoff value at 400 eV, for tetragonal $GaCuSe_2$ they were fulfilled for an energy cutoff at 450 eV and for cubic $GaCuSe_2$ they were fulfilled for an energy cutoff at 500 eV. For the TiFeSi system, the $GaNaTe_2$ system and $GaCuSe_2$ the k-point density was set to 4 during these calculations while it was set to 5 for diamond. For TiFeSi normal Ti, Si and Fe pseudopotentials were used, for diamond normal C potential was used, for $GaNaTe_2$ Ga_d, Na_pv and Te pseudopotentials were used and for $GaCuSe_2$ Ga_d, Cu_pv and Se pseudopotentials were used. These pseudopotentials were used for all other calculations of these materials too, unless for the TiFeSi system which used Ti_pv, Fe_pv and Si for the other calculations except convergence of k-point density. In Appendix A the parameters in the INCAR file for all materials during these calculations are shown.

3.2. Convergence with respect to k-point density

Relative energy, pressure, force and bandgap should also be converged with respect to k-point density. The convergence criterions for TiFeSi system, $GaNaTe_2$ and $GaCuSe_2$ was that relative energy should change less than 1 meV, pressure less than 3 kbar, force less than 0.005 eV/Å and band gap less than 0.01 eV. For diamond the convergence criterions were the same for relative energy, pressure and force, but bandgap should change less than 0.02 eV. These changes are for a change in k-point density of 1 $Å^{-1}$. These parameters were converged for the TiFeSi system when the k-point density was at 4 $Å^{-1}$, and for diamond when the k-point density was at 3 $Å^{-1}$. For the $GaNaTe_2$ system the parameters were only converged for these criterions when the k-point density was at 13 $Å^{-1}$. This is a very high k-point density. Therefore, the convergence criterion for bandgap was raised to 0.1 eV so the convergence criterions were satisfied for a k-point density of 4 $Å^{-1}$. For tetragonal $GaCuSe_2$ a k-point density of 3 was sufficient. For cubic $GaCuSe_2$, convergence considering the relative change in energy between the two phases was very hard to get. Therefore, the relative energy was between the original structure and the structure with the copper atom displaced 0.02 Å in the negative x-direction. Using this relative energy, a k-point density of 7 $Å^{-1}$ was needed for convergence of all parameters and even then, it was not stably converged. Meaning the convergence criterion was not fulfilled for a k-point density of 8 $Å^{-1}$ and 9 $Å^{-1}$. Anyway, for a k-point density of five the change in bandgap was around 0.3 eV, the change in pressure at 3.22 and the change in relative energy was below the convergence criterion. So, a k-point density of five were considered to be good enough. The parameters in INCAR were the same as for the energy cutoff test with the converged energy cutoff value.

After convergence all further calculations were done with energy cutoff and k-point density at least as big as the lowest converging value.

3.3. Relaxation of the structures

The next step was relaxation of the structure. That is to find the lattice constant and atomic positions that lead to lowest energy. This is done by specifying more parameters in the INCAR file. This was done twice, first for the initial POSCAR, then with the relaxed POSCAR as the initial lattice constants. This is because artificial forces and pressures can remain if the initial lattice constants change a lot after the first relaxation[57].

Parameter values in the INCAR file during relaxation are shown in Appendix A. For the $TiFe_2Si$ structure the POTCAR file was made with Ti_pv, Si and Fe_pv pseudopotentials as this seemed to be necessary to get real phonon frequencies, and in the INCAR file GGA was set to PS to use the Perdew-Burke_Ernzerhof revised for solids exchange-correlation potential.

The relaxed lattice constant of the different materials is shown in Table 1. All materials have at most two different lattice parameters.

Table 1: The relaxed lattice parameters of the materials.

Material:	Lattice parameter a:	Lattice parameter c:
Diamond	3.572 Å	a
$TiFe_2Si$	5.632 Å	a
α-$GaNaTe_2$	7.181 Å	10.173 Å
β- $GaNaTe_2$	8.079 Å	6.7504 Å
Tetragonal $GaCuSe_2$	5.573 Å	11.075 Å
Cubic $GaCuSe_2$	6.506 Å	a

3.4. Calculation by density functional perturbation theory

After convergence and relaxation, the DFPT calculations were done to calculate the elastic tensor, the piezoelectric tensor and the Born effective charge. This was done by specifying the parameters of the DFPT calculations as tabled in Appendix A. The Debye temperature calculated from the elastic tensor was zero for cubic $GaCuSe_2$. Therefore, the phonon eigenfrequencies of this material was checked, and they were imaginary, which means that cubic $GaCuSe_2$ is unstable.

3.5. Calculations of canonical configurations

The elastic parameters were then used to calculate the Debye temperature as described in theory by the program Elastic_debye.py. A supercell of each material was created by the program generate_structure which is in the TDEP package, with 200 as the desired number of atoms in the cell. Diamond got a supercell of 216 atoms, $TiFe_2Si$ got a supercell of 56 formula units, both $GaNaTe_2$ stuctures got supercells of 60 formula units and $GaCuSe_2$ got a supercell of 54 formula units. The program canonical_configuration, also in the TDEP package, used the supercell and force constants derived from the Debye temperature to create configurations that were canonical ensembles of the supercell at 300 K. It created 20 configurations for diamond, $TiFe_2Si$ and $GaCuSe_2$. For each of these configurations, a standard total energy calculation was done using VASP. For $GaNaTe_2$, 100 configurations were made for each structure. However, for the α-structure, the total energy was only calculated for eight of the configurations. For the β-structure, the total energy was only calculated for five of the configurations. The parameters of the INCAR files are tabled in Appendix A. Parameters for electronic relaxation are the only parameters needed for these calculations. When these calculations were finished, the program process_outcar_5.3.py from the TDEP package was used to evaluate the OUTCAR files and create input files for the another TDEP program, extract_forceconstants. This program then used those files, with a cutoff radius for the atoms included in the calculations for the second order force constants at 7 Å, to find the correct second order force constants. These force constants were used by phonon_dispersion_relations to calculate the phonon dispersions and the vibrational free energy at 300 K. The dispersion relations were then plotted to see that there were no imaginary phonon frequencies. If there were, the material is dynamically unstable.

3.6. Convergence of phonon free energies

For $TiFe_2Si$ and $GaNaTe_2$ convergence of phonon free energy at 300 K, 1500 K and 3000 K with respect to number of configurations were done to ensure that the free energies were converged at the whole temperature specter. For $GaCuSe_2$ the convergence was checked at 300 K, 1500 K and 2000 K. The convergence criterion was that the free energy should change less than 1 meV/formula unit for one more configuration. This was fulfilled for 3 configurations used for $TiFe_2Si$ and for 4 configurations for β-$GaNaTe_2$. Difference in free energy vs number of configurations is shown in Appendix B. For $GaCuSe_2$ it was problematic to make the phonon free energy converge with this criterion at 1500 K and 2000 K. Therefore, the relative convergence was checked at the different temperatures. The relative change going from five configurations to six at 300 K was bigger than the relative change at this step for the other temperatures. At five configurations the original convergence criterion was fulfilled at 300 K. Therefore, five configurations were considered to be sufficient. For α-$GaNaTe_2$, the force constants corresponded to imaginary phonon frequencies even when they were extracted from 19 canonical configurations which means that the structure is dynamically unstable for this material. To check if it was stable at 100 K or 1000 K, 20 canonical configurations were made at these temperatures too and used to calculate force constants in the same approach as at 300 K. These force constants also corresponded to imaginary phonon frequencies. Therefore, there was done no further calculations on this structure. Convergence of free energy at 300 K with respect to the cutoff radius of the second order force constants were also done for $TiFe_2Si$. The cutoff values were chosen so that they exactly included the next layer of neighbor atoms in the calculations. From Appendix B it can be seen that the free energy is converged under 1 meV/formula unit for a cutoff value at 2.81594 Å, which is far below the value used here. So, these calculations are well converged with respect to cutoff value of the second order force constants. This convergence test was based on information from the calculations of all 20 configurations. How much the final free energies changed with respect to the Debye temperature were also explored for primitive rhombohedral $TiFe_2Si$. That means the Debye temperature used to create the first configurations was varied and the final free energies originating from different Debye temperatures were compared. The dependence is shown in Appendix B.

3.7. Volume grid

Five new unit cells were created for diamond, one where the lattice parameter was one percent longer than the lattice parameter at 0 K, one where it was two percent longer, one where it was three percent longer, one where it was one percent shorter and one where it was two percent shorter. For $TiFe_2Si$ nine new unit cells were made, those as for diamond and in addition four that were four to seven percent longer. For each of the different sizes of the unit cell, including the original one, a supercell was made as before. From these supercells 20 canonical configurations were made for diamond and three for $TiFe_2Si$ as the convergence test showed that three were sufficient. These canonical configurations were not made using the Debye temperature, but with the extracted force constants used to find phonon dispersions and free energies as described earlier. They were extracted from information about all 20 configurations for both $TiFe_2Si$ and for diamond and a cutoff value of 7 Å for the second order force constants. Then the same method as above was used for each of these lattice parameters to calculate free energies in the range from 0 K to 3000 K with steps at 1 K. The total energy calculations for each canonical configuration were done with the INCAR values from table 7 for these materials. Also, a standard total energy calculation was done for each of the different sizes of each material at the small unit cells that the supercells were made from, also these with INCAR parameters from table 7. Then for both materials, the program read_data.py read these total energies at 0 K, the free energies from 0 K to 3000 K and the lattice parameters of the different sizes of the material in for further analysis as described below.

3.8. Finding the lattice parameter and coefficient of thermal expansion

For each temperature, the total energy, that is the energy from the 0 K calculation plus the free energy, was plotted as a function of size. These points were then used to fit a Birch-Murnaghan equation of state expression for the energy and decide the lattice parameter at that temperature based on the minimum energy. For a reliable fit it was required that the minimum of the curve was within the range of the expanded lattice parameter. This was ensured for all materials within in temperature range used. The lattice parameter could then be plotted as a function of temperature and further the coefficient of thermal expansion from the derivative of it. To get a continuous CTE, the natural logarithm of the lattice parameter had to be interpolated by polynomials that matched on their endpoints. For diamond this interpolation was from 0 K to 3000 K with steps at 100 K for each polynomial. For $TiFe_2Si$, the interpolation was from 0 K to 3000 K with steps at 30 K. For both materials, polynomials of third order were used. Both polynomial degree and their range were tested to find those which gave lowest mean squared error. These interpolations gave a high accuracy, with a mean squared error of $7.14202 \cdot 10^{-15}$ for diamond and of $2.51678 \cdot 10^{-15}$ for $TiFe_2Si$.

3.9. Reduction of volumes

For more complicated lattice systems, such as tetragonal and orthorhombic, there are, respectively two and three lattice parameters to find as a function of temperature. To find the lattice parameters, canonical configurations must be made for the different sizes of the unit cell. However, the number of unit cells needed to span the whole temperature scale for a material with one lattice parameter, will now be to the power of two and three for materials with two and three independent lattice parameters respectively. That means for a material with two or three lattice parameters that expands like $TiFe_2Si$, where ten unit cells were needed, 100 and 1000 unit cells are now needed. And from these, several canonical supercell configurations have to be made and calculated for. It would be nice if not all different sizes of the lattice parameters were needed. This was checked for $TiFe_2Si$, including the unit cell with lattice parameter three percent shorter than the lattice parameter at 0 K. As 3000 K probably is outside the temperature range of interest, 2000 K was the highest temperature included in this test. In this temperature range, lattice parameters from -2 percent to 5 percent should be more than enough to get good Birch-Murnaghan equation of state fit at all temperatures. It was found that only using the lattice parameter that was three percent shorter, one percent shorter, one percent longer, three percent longer and five percent longer, gave a coefficient of thermal expansion which differed below 2 % except for the very lowest temperatures as shown in Figure 7. At the lowest temperatures the values are very small, so the percentage difference is not a good measurement of the error. Therefore, starting at compression of 3 % and increasing the volume with 2 % of the 0 K structure for each step, was considered to be a sufficient approximation.

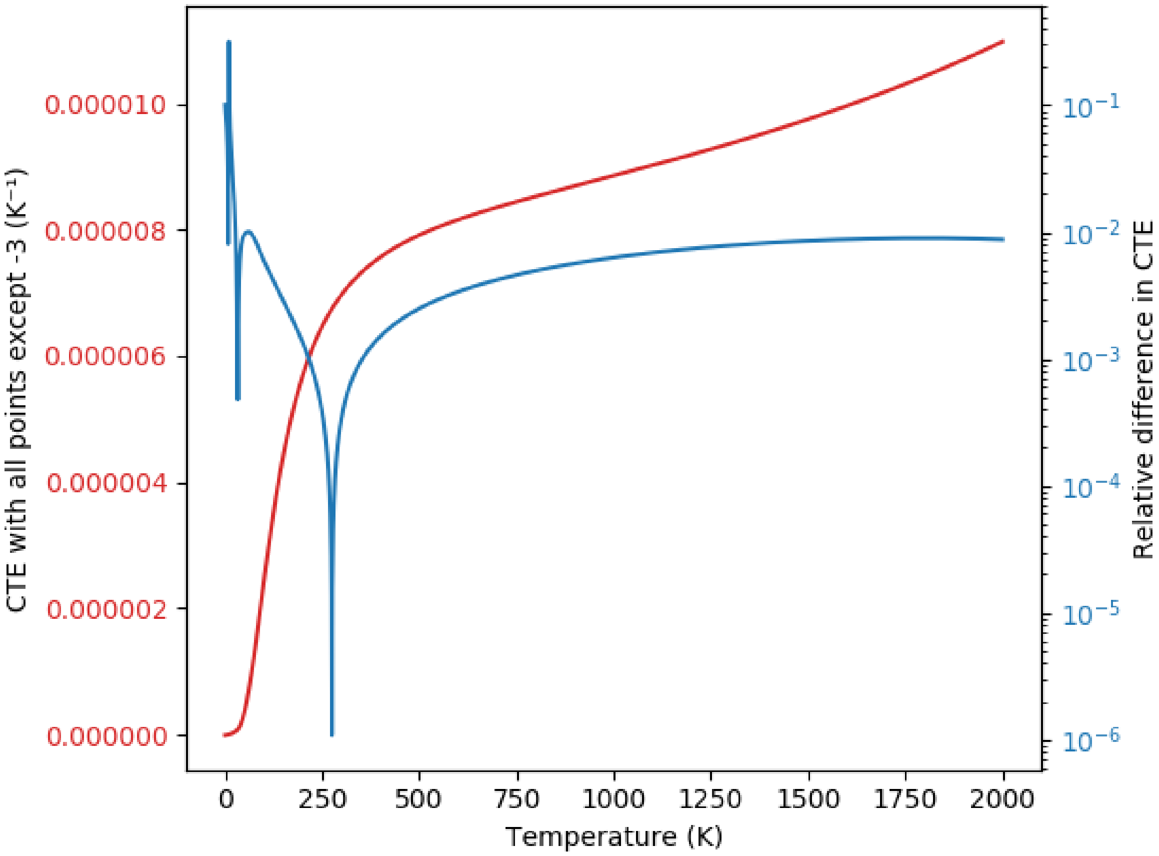

Figure 7: Difference between CTE calculated using the eight original unit cell sizes from -2 % to 5 %, and CTE calculated using the selected five sizes for $TiFe_2Si$.

3.10. Volume grid for β-$GaNaTe_2$

For β-$GaNaTe_2$, unit cells with lattice parameters from minus three percent to three percent with two percent between each step were made. That gives four different lengths of each independent lattice parameter. β-$GaNaTe_2$ has a tetragonal crystal system, which means that four to the power of two different unit cells were needed to find the free energy as a function of the two independent lattice parameters. For each of these unit cells a supercell was created, and from them the six canonical configurations were created at first because the total energy calculations of them were sometimes hard to converge. The canonical configurations were made with force constants extracted from four of the canonical configurations of the supercell made from the relaxed structure. With six cells and expecting only four to be needed, it should be possible to get enough equations for the force constants even if not all calculations did converge. The result was that three calculations did not converge, all corresponding to different volumes. That means the phonon free energies for each volume originated from at least five configurations, which should be sufficient. For those which all six calculations converged, all six configurations were used. However, for the unit cell with three percent longer a-lattice vector and one percent longer c-lattice vector, five configurations were not enough to get only real phonon frequencies. So, eleven new configurations were made for it and calculated for. Out of the eleven new configurations, nine converged successfully. It was sufficient with six configurations to get proper free energies, so six configurations were used. These total energy calculations were done with INCAR values from table 7 for this material. Then the free energies for each unit cell were found as before in the range from 0 K to 1500 K. Total energy calculations were done on the original unit cells with different sizes of this material. These calculations were also done with INCAR values from table 7 for this material. Then the program CTE.py read these total energies at 0 K and phonon free energies in, to get the total energy for each size at each temperature. At each temperature the total energies were fitted to a polynomial with all combinations of the two lattice parameters to second order. From this polynomial the total energy was minimized as a function of lattice parameters using scipy.optimize's function minimize. From this the lattice parameters as a function of temperature was found. The natural logarithm of the lattice parameters as a function of temperature was interpolated by third order polynomials from 0 K to 1500 K with steps at 50 K. This gave a mean squared error of $6.205*10^{-11}$ for the fit of the a-lattice parameter and of $6.626*10^{-11}$ for the fit of the c-lattice parameter. From these interpolations the CTE of each lattice parameter was found.

3.11. Volume grid for $GaCuSe_2$

For $GaCuSe_2$ the independent lattice parameters varied from minus three percent to five percent with two percent between each step. As this structure also is tetragonal, it has two independent lattice parameters, which gives 25 different unit cells needed to find the lattice parameters as a function of temperature. For each of these unit cells, a supercell was made as usual. Before making canonical configurations of these supercells, they were relaxed with respect to the atomic positions with fixed lattice parameters. Most of the supercells were able to be relaxed using 64 cpu's from SAGA with time limit of three days. However, for four cells this was not sufficient, neither with the blocked Davidson algorithm (ALGO = Normal in INCAR). These cells were the one with three percent shorter a-lattice parameter and three percent longer c-lattice parameter, the one with one percent longer a-lattice parameter and five percent longer c-lattice parameter, the one with three percent longer a-lattice parameter and three percent longer c-lattice parameter and the one with three percent longer a-lattice parameter and five percent longer c-lattice parameter. Therefore, they were tried relaxed using lighter convergence parameters in the INCAR first. That is lowering the energy cutoff to 400 eV and setting PREC to normal instead of accurate. Using these parameters in the INCAR, these cells were relaxed successful too. Then these structures were relaxed with the INCAR values that were used for all supercells shown in Appendix A. For the supercell with three percent shorter a-lattice parameter and three percent longer c-lattice parameter, this did not work immediately. SYMPREC, which determines the accuracy the atomic positions, had to be specified to 10^{-8}. Then it did work.

After relaxation of the atomic positions in the supercells, the position of the atoms in the original sized cells did no longer correspond to the position of the atoms in the supercells. Therefore, the correct position of the original sized cells had to be found. This was done by combining the different directionally positions in the non-relaxed supercell and multiplying with an integer. Then for the correct combination and integer, the position in the x-direction of the first and last selenium atom in the original structure was found. The idea behind this is that by the correct combination, the original shape of the unit cell was restored, and at least one of the atoms should be positioned at a fraction of the atoms mentioned position in the original cell. Combining the directions can for example be the z-position minus the y-position. Once the combination and integer were found, the atomic position in the relaxed supercell that corresponded to the atomic position in the non-relaxed supercell, was combined and multiplied by the combination and integer found. The result of this was then the correct relaxed position in the original sized cell. After that the usual procedure could be performed, where the supercells were made from the original cells with the new correct positions. For each of these supercells, five canonical configurations were made, and their total energies were calculated. Some of these cells needed more than 60 electronic self-consistency steps to converge, which is the standard limit of steps in VASP. Therefore, this limit was set to 300. However, this did not make the cells converge. Therefore, the limit was put back to 60 and other configurations were run until at least five configurations were converged for each volume. From these configurations, force constants and free energies were calculated as before. Using the program CTE.py again, the CTEs could be plotted by using a spline interpolation of the natural logarithm of the lattice constants and take the derivative of these. The interpolation was done by using third order polynomials with steps of 100 from 0 K to 2000 K. This gave a mean squared error of $4.289*10^{-11}$ for the fit of the a-lattice parameter and a mean squared error of $2.034*10^{-10}$ for the fit of the c-lattice parameter.

3.12. Calculation of third order force constants

To calculate the third order force constants, the same method as when calculating the second order force constants was used, except two deviations. One, more configurations were needed since there are many more third order force constants than of second order. For $TiFe_2Si$, 150 configurations were created to check convergence of the third order force constants with respect to number of configurations used. Two, extract_forceconstants were used to calculate third order force constants too with a cutoff value at 5 Å. The INCAR values when calculating the total energy of the configurations used to calculate the third order force constants are the same as when calculating the total energy of the supercell configurations of the 0 K structure for this material. The third order force constants were only calculated for $TiFe_2Si$.

Maximum of the absolute difference of the third order force constants with respect to number of configurations used, is shown in Figure 8 for $TiFe_2Si$. It shows that the absolute difference is very small at 40 K. The relative difference was also considered. However, it was very high for the lowest force constants and those will probably give less contribution because they are small. To investigate this, the third order force constants were sorted from highest to lowest and their values were plotted alongside their relative differences, extracting the third order force constants from ten more configurations. This is shown in Figure 9 using 40 configurations of $TiFe_2Si$. It shows that the highest values are well converged under 2 % using 40 configurations. The smaller values are probably less important. Therefore, 40 configurations were considered sufficient for this material.

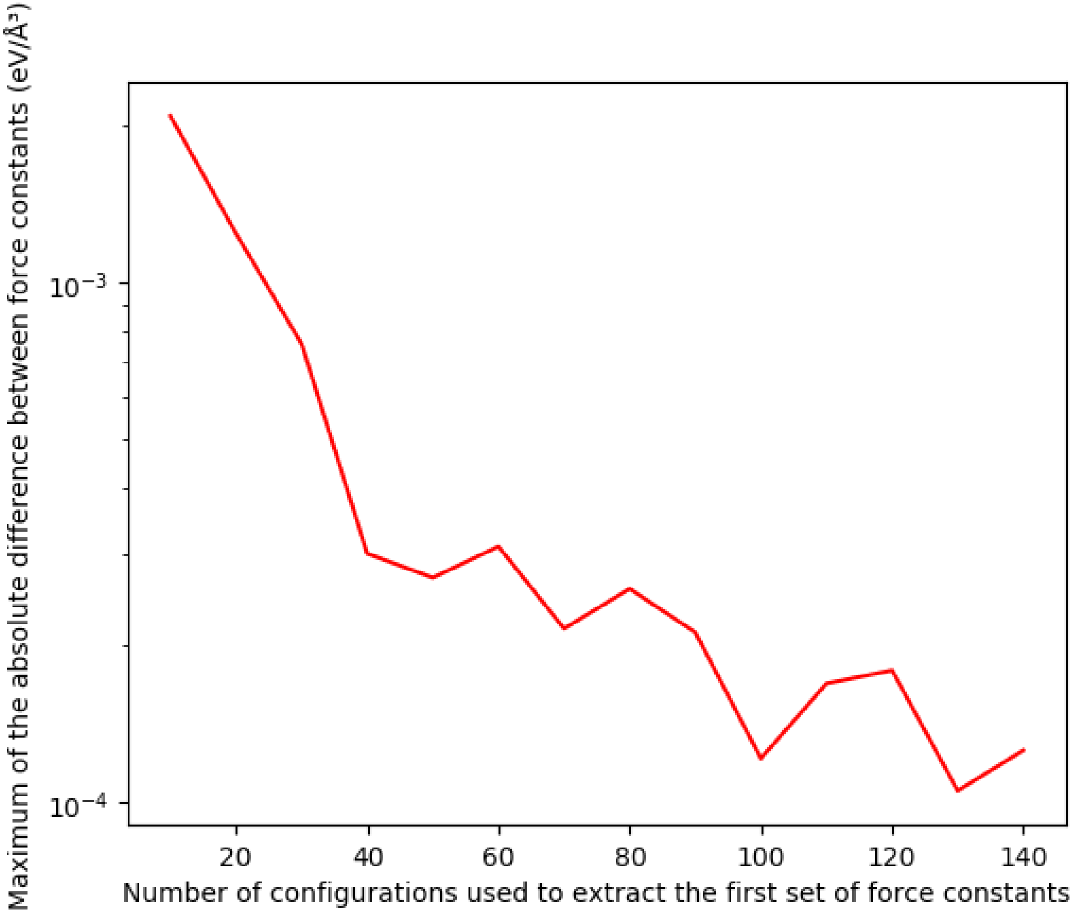

Figure 8: The maximum of the absolute difference between the third order force constants extracted from the number of configurations corresponding to the x-axis and extracted from ten more configurations for $TiFe_2Si$*. The first point is at 10 and goes up to 140. That means that the last force constants compared are extracted from 150 configurations.*

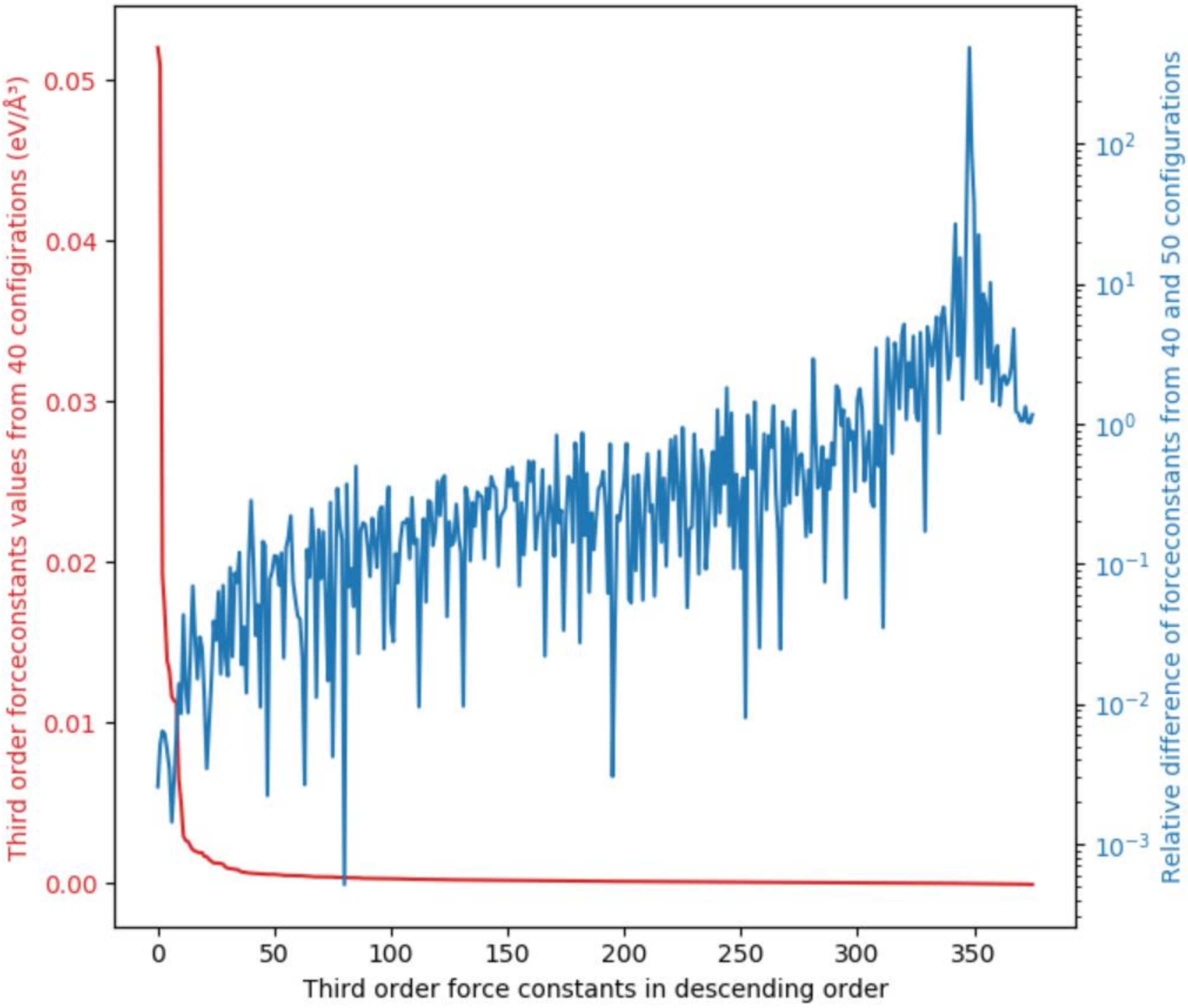

Figure 9: Third order force constants in descending order extracted from 40 configurations of $TiFe_2Si$. The red line shows their value while the blue line shows the relative difference extracting them using ten more configurations.

3.13. Method of heat capacity

When the free energies were found, TDEP automatically also calculated the heat capacity per atom at constant volume at all temperature steps specified. Therefore, the heat capacity could also be plotted. This was done by investigating how the heat capacity depended on the volumes at constant temperature. For almost all volumes, this dependency was approximated well by a cubic polynomial. Therefore, for each temperature step, the heat capacity was found by constructing a cubic fit of the heat capacity as a function of the lattice constant and selecting the heat capacity from this fit given the optimized lattice constant which was found as before. The cubic fit seems to be a good approximation at all temperatures for both cubic materials. For the tetragonal materials, polynomials which depended on all combinations of the two lattice parameters up to third order were considered to be sufficient from the investigation of the cubic materials. It was also checked that this fit gave a decent mean squared error and r2 score also for the tetragonal materials. The mean squared error for $GaNaTe_2$ was at $4.995*10^{-18}$ and the r2 score at 0.9999558. Figure 10 shows the real points and cubic fit at 1 K for diamond, Figure 11 at 50 K and Figure 12 at 500 K. The maximum mean squared error of these fits is at $5.727*10^{-17}$ and the smallest r2 score is at 0.9997691, and these do not get much better by more complex fits. When the heat capacity was found for each temperature a spline which consisted of cubic polynomials, was used to smoothen the curve. For all materials the polynomial intervals were at 10 K, which gave a mean squared error of 0.3242 for diamond, 0.1172 for $TiFe_2Si$, 0.0008292 for $GaNaTe_2$ and 0.0005894 for $GaCuSe_2$.

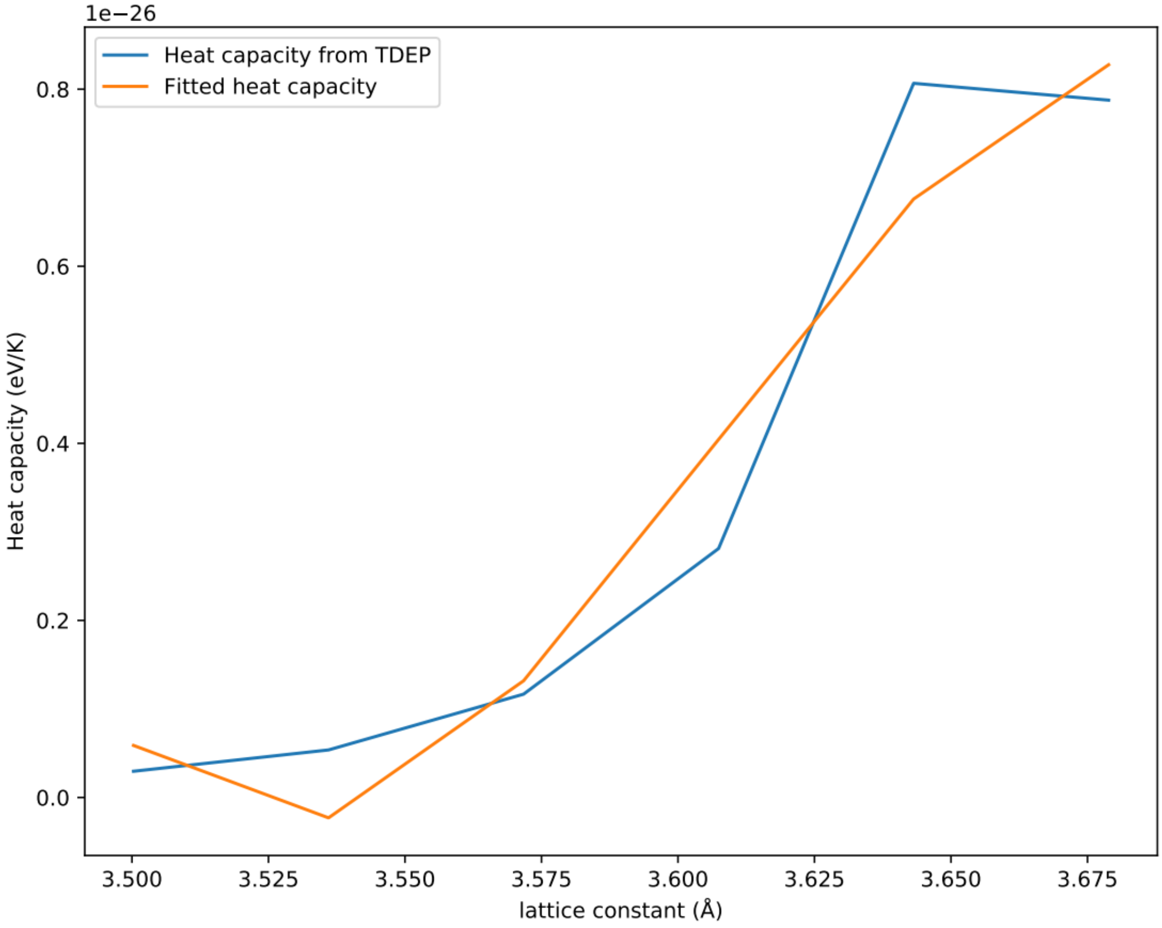

Figure 10: Heat capacity calculated within TDEP and the cubic fit at 1 K for diamond.

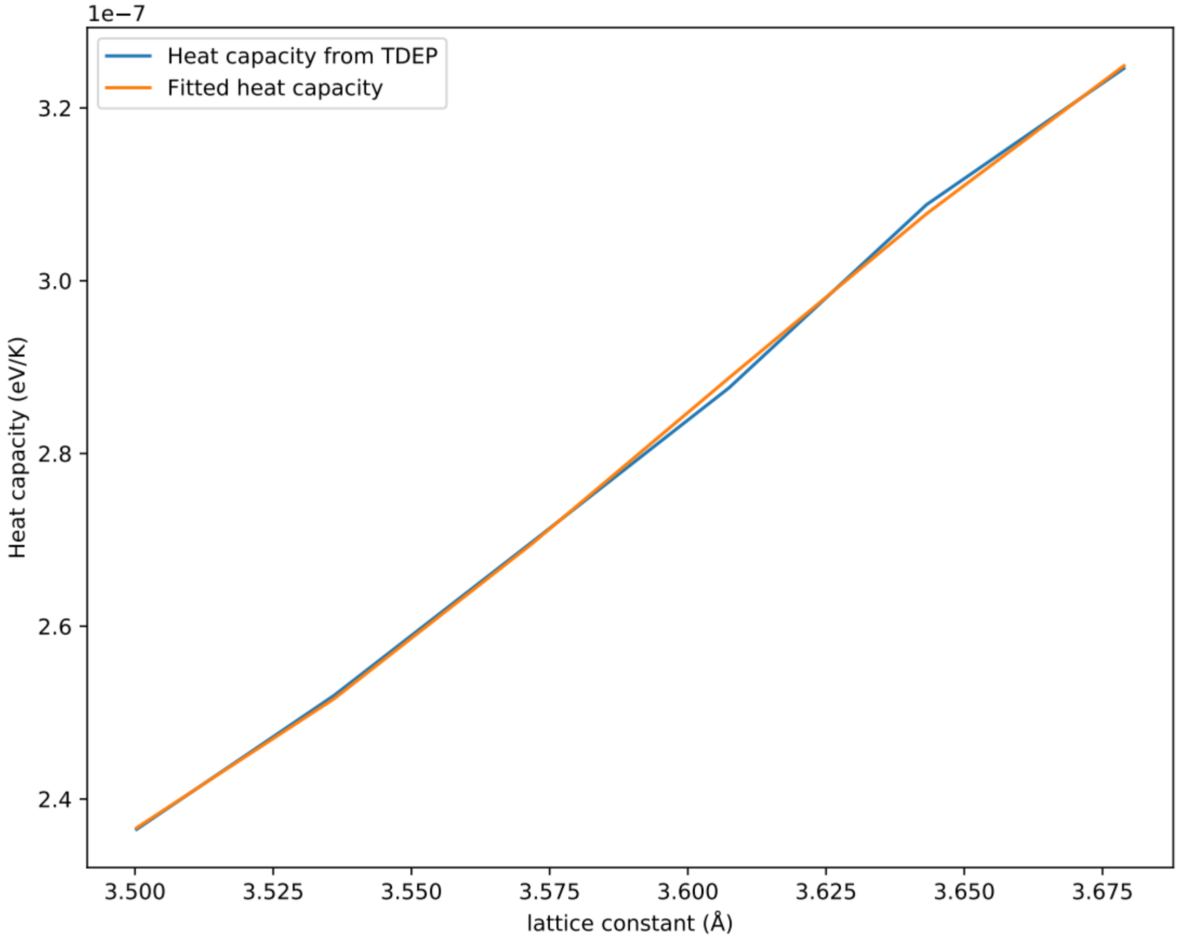

Figure 11: Heat capacity calculated within TDEP and the cubic fit at 50 K for diamond.

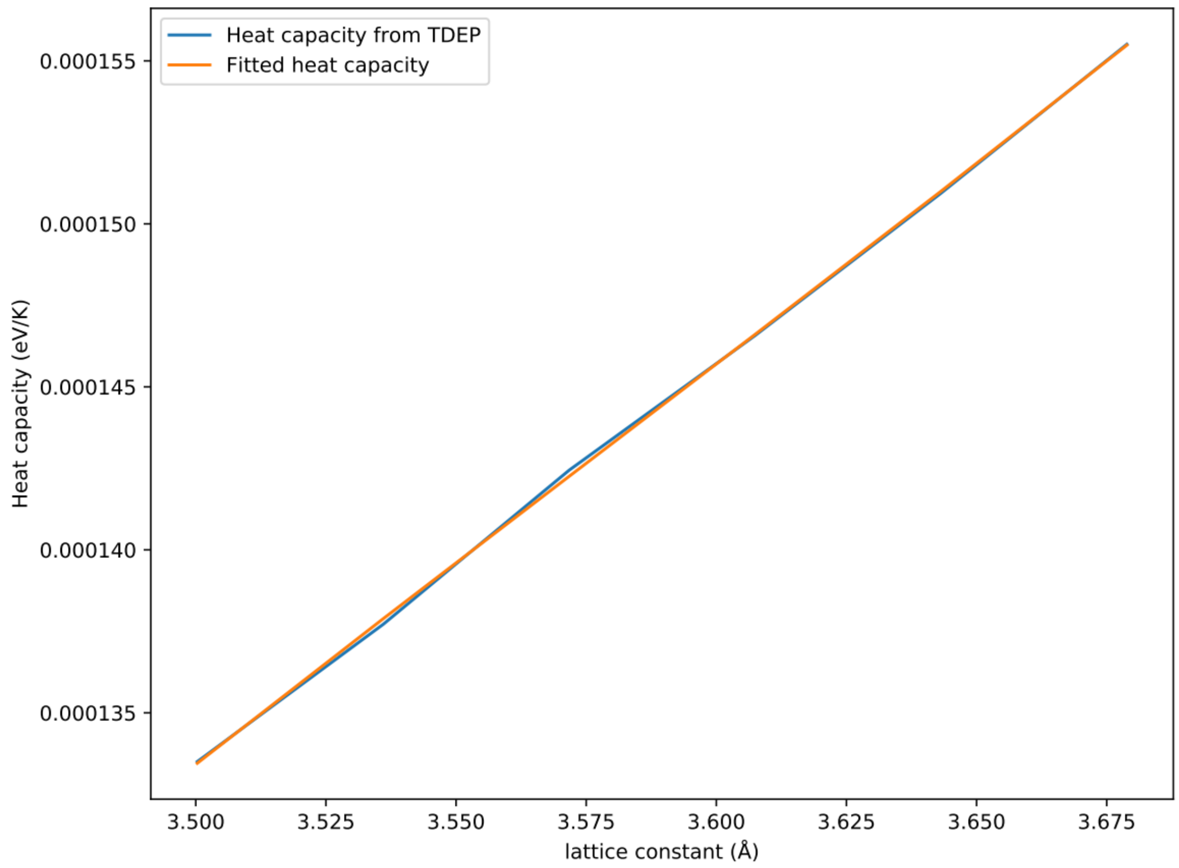

Figure 12: Heat capacity calculated within TDEP and the cubic fit at 500 K for diamond.

3.14. Gibbs free energy as a function of temperature and secondary pyroelectric vector

The Gibbs free energy as a function of temperature and pressure was found by compressing the volume from 0 % to 10 % for cubic materials, while from 0 % to 30 % for the tetragonal materials with hundred steps between. From this the pressure was calculated from Equation 37 and the Gibbs free energy from Equation 40 at each temperature. The secondary pyroelectric vector was directly calculated from Equation 45 after the CTEs were found for $GaCuSe_2$.

3.15. Summary of method

The method which has led to the results has been demonstrated. In this method the calculation of the primary pyroelectric vector is not included. What goes again for each material are:

1. Convergence of VASP parameters.
2. Relaxation of structure.
3. Calculation of elastic parameters and finding the Debye temperature.
4. Calculate "fake" force constants from Debye temperature.
5. Make a supercell of the material and generate canonical ensembles from it and the fake force constants and calculate their total energy.
6. Calculate "correct" force constants from these configurations.
7. Make unit cells with expanded and compressed lattice parameters.
8. For each of these, do step 5 with correct force constants.
9. Calculate the vibrational free energy as a function of temperature for each combination of lattice parameters. The heat capacity will also be calculated.

10. For the unit cells in step 7, do a total energy calculation.
11. Add the total energy of the small cell and the vibrational free energy to get the Helmholtz free energy as a function of temperature for each volume. By minimization the CTEs will be found.
12. Use Birch-Murnaghan to calculate the Gibbs free energy as a function of temperature and pressure. This can predict a phase change if there are more phases to compare.
13. Use Equation 45 to calculate the secondary pyroelectric vector.

4. Results

The main results of each material are presented here. Those are the CTEs as a function of temperature, the lattice parameters as a function of temperature, the Helmholtz free energy as a function of temperature (Gibbs free energy at zero pressure), the heat capacity and Gibbs free energy as a function of temperature and pressure. The secondary pyroelectricity is also presented for $GaCuSe_2$. Uncertainty origins are given in tables, and the resulting uncertainties for each result are included in all results except for the Gibbs free energy vs temperature and pressure.

4.1. Results of diamond

For diamond the coefficient of thermal expansion is shown in Figure 13 with error bars. The uncertainty originates from the uncertainty of the total energy at 0 K due to the final energy cutoff and the final k-point density. The uncertainty of the total energy at 0 K is shown in Table 2. The uncertainty also comes from the uncertainty in the vibrational free energy due to the uncertainty in the Debye temperature, variation with number of configurations used and final cutoff value of the second order force constants. The uncertainty of the vibrational free energies is shown in Table 3. The uncertainty in the phonon free energy due to uncertainty in the Debye temperature and due to the final cutoff value of the second order force constants is only calculated for $TiFe_2Si$, and the relative uncertainty from this is considered to be universal for all materials in this study. For diamond convergence with respect to configurations is not done, so the uncertainty in phonon free energy due to number of configurations for $TiFe_2Si$ is considered to hold for diamond too. Considering that 20 configurations are used for diamond which is a more symmetric material than $TiFe_2Si$ with less force constants, this uncertainty is definitively not too small.

Further the relative uncertainty of the phonon free energy for $TiFe_2Si$ is calculated at 300 K, which seems to represent the relative uncertainty well at all temperatures. For all these, the convergence criterion is that the change in relative energy or the total phonon free energy should be less than 1 meV per change specified to the parameter looked at. However, sometimes the change is less and then this smaller change has been used in calculating the relative change. The change in total energy due to energy cutoff is 0.4519 meV for a raise in energy cutoff from 400 eV to 450 eV. This is then the absolute change considered, and the total energy at 450 eV was -9091.18 meV, while it gives an absolute relative energy change of $4.97*10^{-5}$ using the formula $\sigma = \frac{\mathrm{E_{end}} - \mathrm{E_{start}}}{E_{end}}$, where σ is the uncertainty, E_{end} is the energy after the raise and E_{start} is the energy before the raise. This is how the uncertainty is calculated for the uncertainties named above. Then the total uncertainty in total energy and free energy is calculated by adding the squares of each uncertainty and taking the square root of this sum. The uncertainty in the CTE in the positive direction will be the absolute difference in the CTE calculated using the calculated energies at 0 K and phonon free energies vs the CTE from the maximum deviated energy at 0 K and the maximum deviated phonon free energy in the positive direction. The uncertainty in the CTE in the negative direction is the same, but here the compared CTE originates from the maximum deviated energies in the negative direction. The uncertainty for other properties is calculated in the same way, just considering the maximum deviations for that property.

Since the structure of diamond has inversion symmetry, its piezoelectric tensor is zero and following the second term of the piezoelectric coefficient zero at all temperatures. The lattice parameter as a function of temperature is shown in Figure 14. The Gibbs free energy at zero pressure per atom is shown in Figure 15, the heat capacity at constant volume per atom is shown in Figure 16 and the Gibbs free energy per atom as a function of temperature and pressure is shown in Figure 17.

Table 2: Uncertainties in the static lattice for diamond.

Uncertainty origin:	Energy cutoff	K-point density	Total uncertainty in the static lattice
Uncertainty (%):	0.00497	0.00368	0.00619

Table 3: Uncertainties in the phonon free energy of $TiFe_2Si$. The uncertainty due to the uncertainty in Debye temperature and cutoff value of second order force constants are universal for all materials.

Uncertainty origin:	Debye temperature	Number of configurations	Second order force constants cutoff value	Total uncertainty in phonon free energy
Uncertainty (%):	1.511	0.0846	0.147	1.520

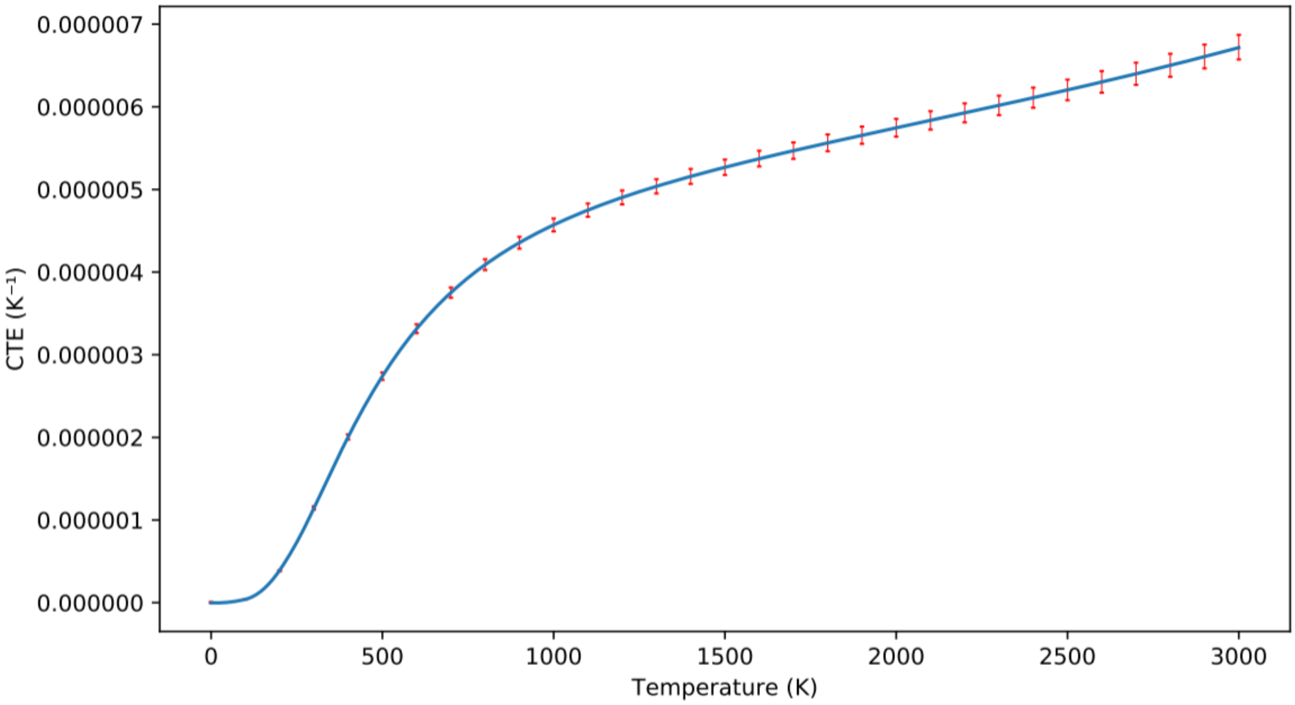

Figure 13: Coefficient of thermal expansion for diamond plotted with error bars.

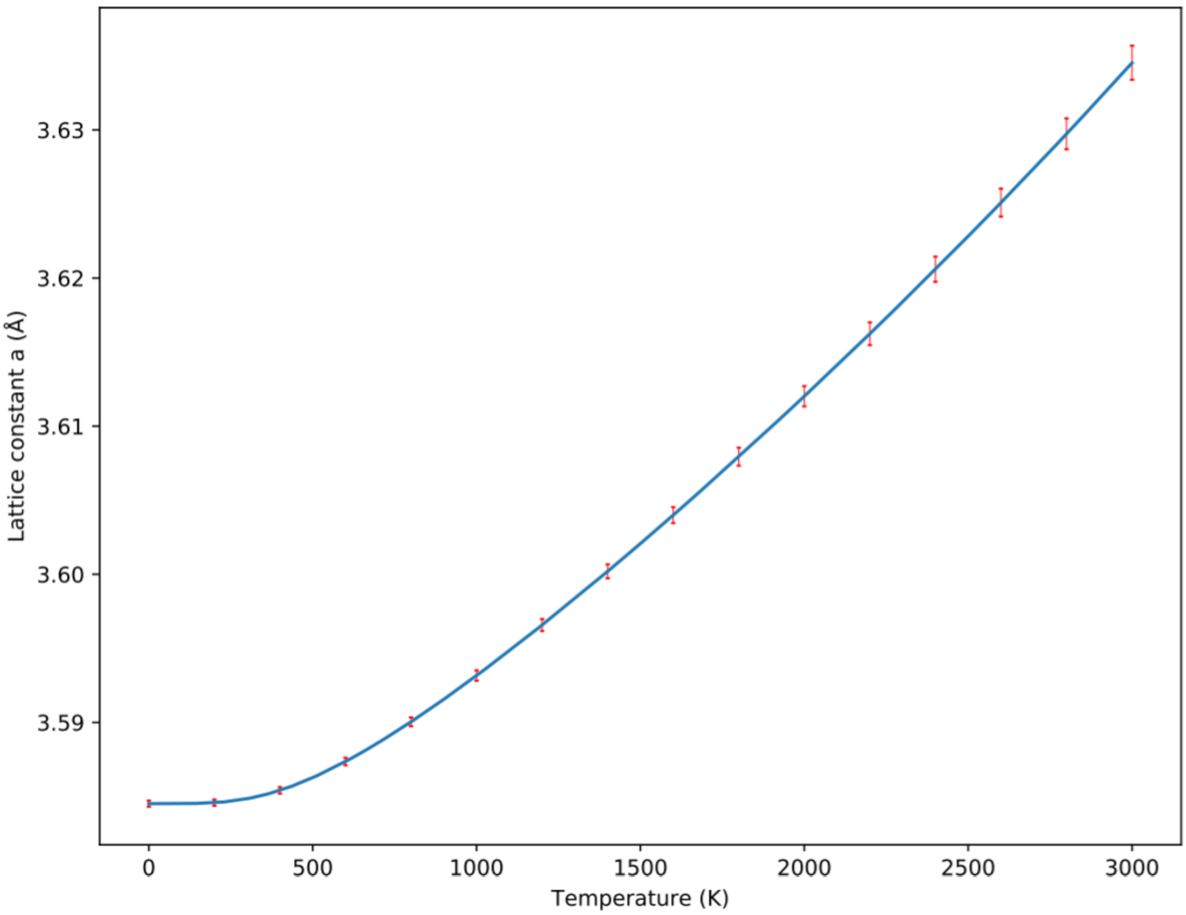

Figure 14: The lattice constant of diamond as a function of temperature with error bars.

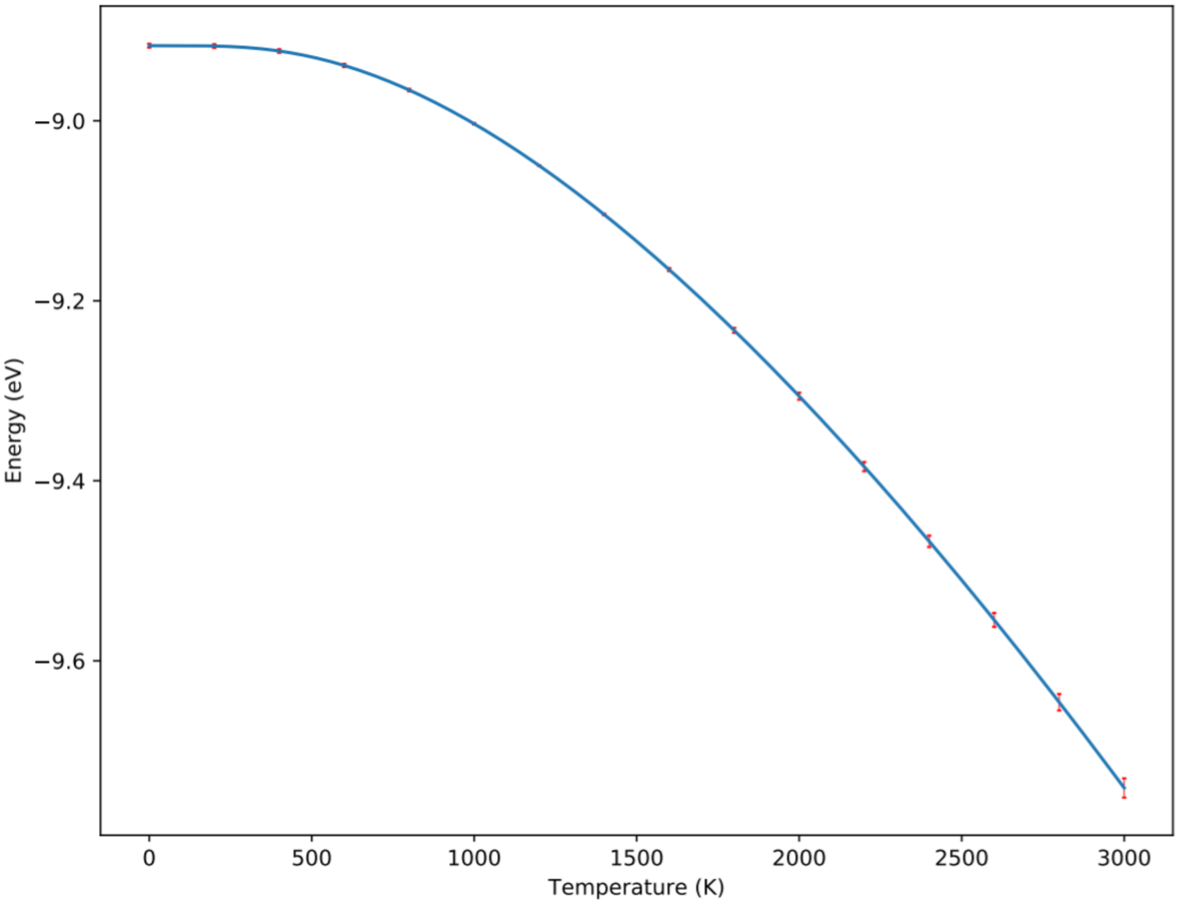

Figure 15: Gibbs free energy at zero pressure per atom as a function of temperature for diamond.

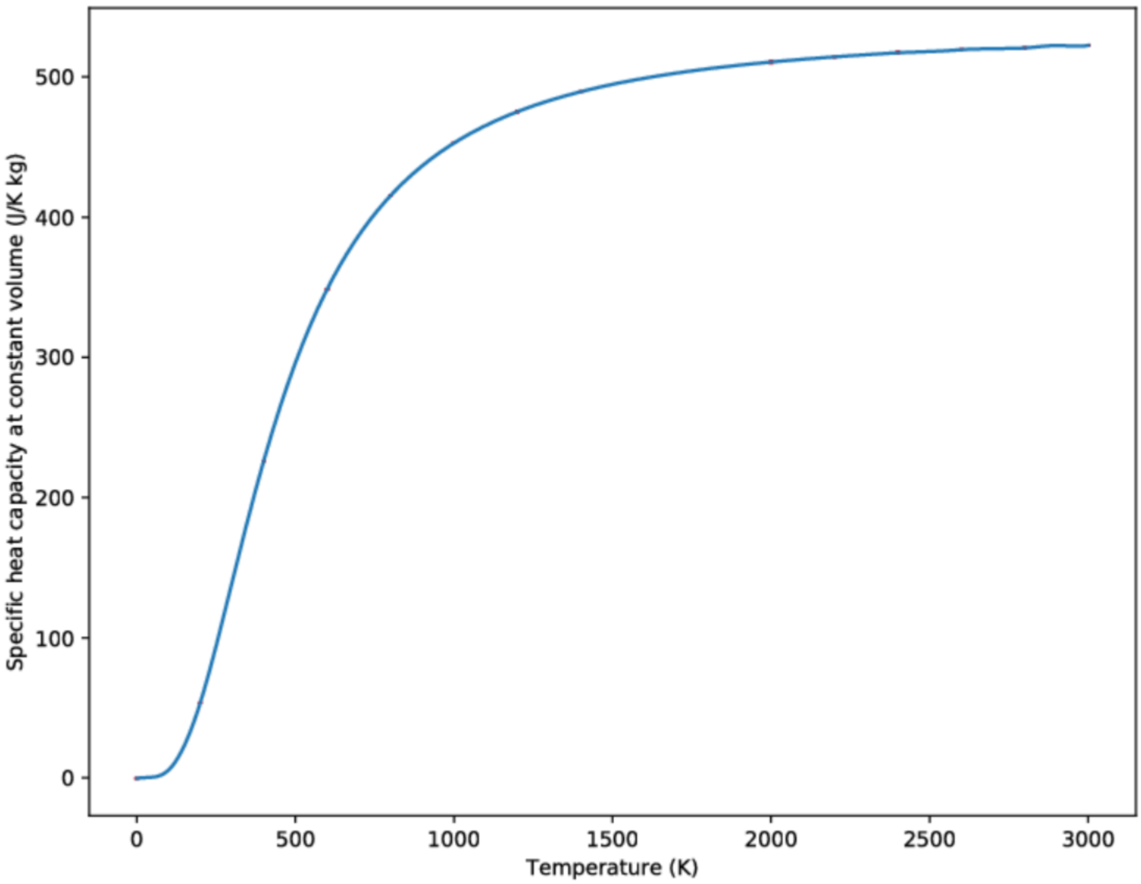

Figure 16: Specific heat capacity at constant volume per atom for diamond.

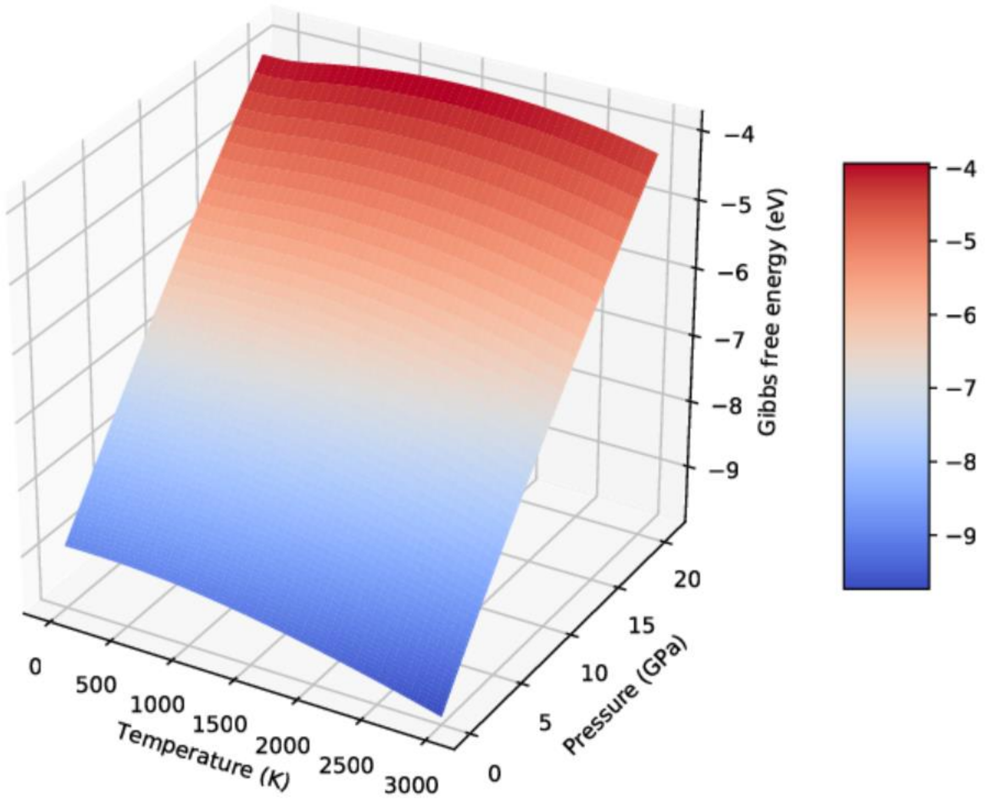

Figure 17: Gibbs free energy per atom as a function of temperature and pressure for diamond.

4.2. Results of $TiFe_2Si$

The CTE of $TiFe_2Si$ is shown in Figure 18 with error bars resulting from the uncertainties in Table 3 and Table 4, except that free energies from the volume with 7 % longer lattice constant was calculated using information from only two configurations as only two of the calculations of the configurations converged for this volume. This makes the uncertainty in the free energy originating from number of configurations go from 0.0846 % to 1.24 % which makes the total uncertainty in the free energies from this volume go from 1.52 % to 1.96 %. This was accounted for by using this uncertainty only for the free energies from that volume, and resulted in a significant larger uncertainty at the highest temperatures. $TiFe_2Si$ has inversion symmetry so its pyroelectric second term is zero just as for diamond.

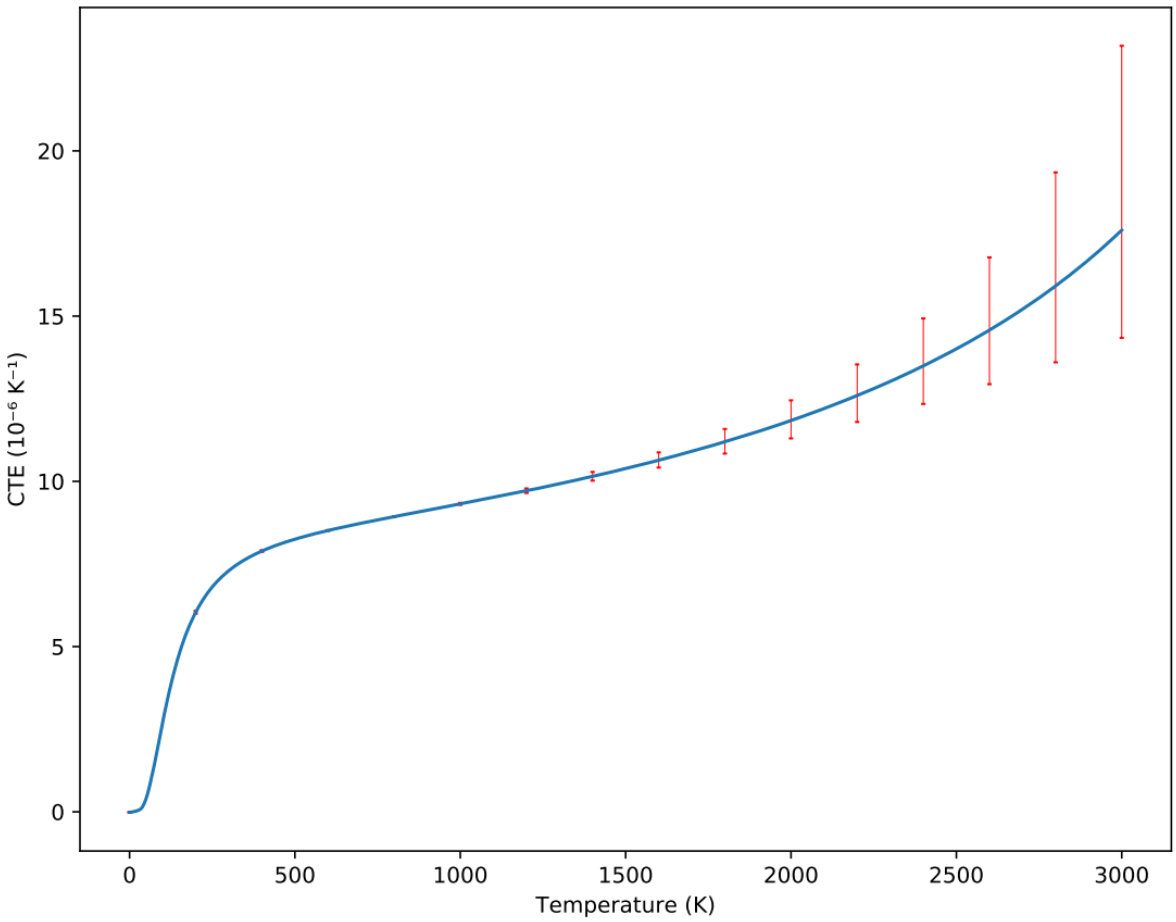

Figure 18: Coefficient of thermal expansion for $TiFe_2Si$ plotted with error bars. The uncertainty becomes very large at high temperatures due to the free energies of the 7 % larger volume only being calculated from two configurations.

Table 4: Uncertainties in the static lattice of $TiFe_2S$ which is used to calculate the uncertainties of the other properties.

Uncertainty origin:	Energy cutoff	K-point density	Total uncertainty in the static lattice
Uncertainty (%):	0.00413	0.0490	0.0492

Since the structure of $TiFe_2Si$ has inversion symmetry its piezoelectric tensor is zero and following the second term of the pyroelectric coefficient zero at all temperatures. The lattice parameter as a function of temperature is shown in Figure 19, the Gibbs free energy as a function of temperature at 0 pressure in Figure 20, the heat capacity as a function of temperature in Figure 21 and the Gibbs free energy as a function of temperature and pressure in Figure 22.

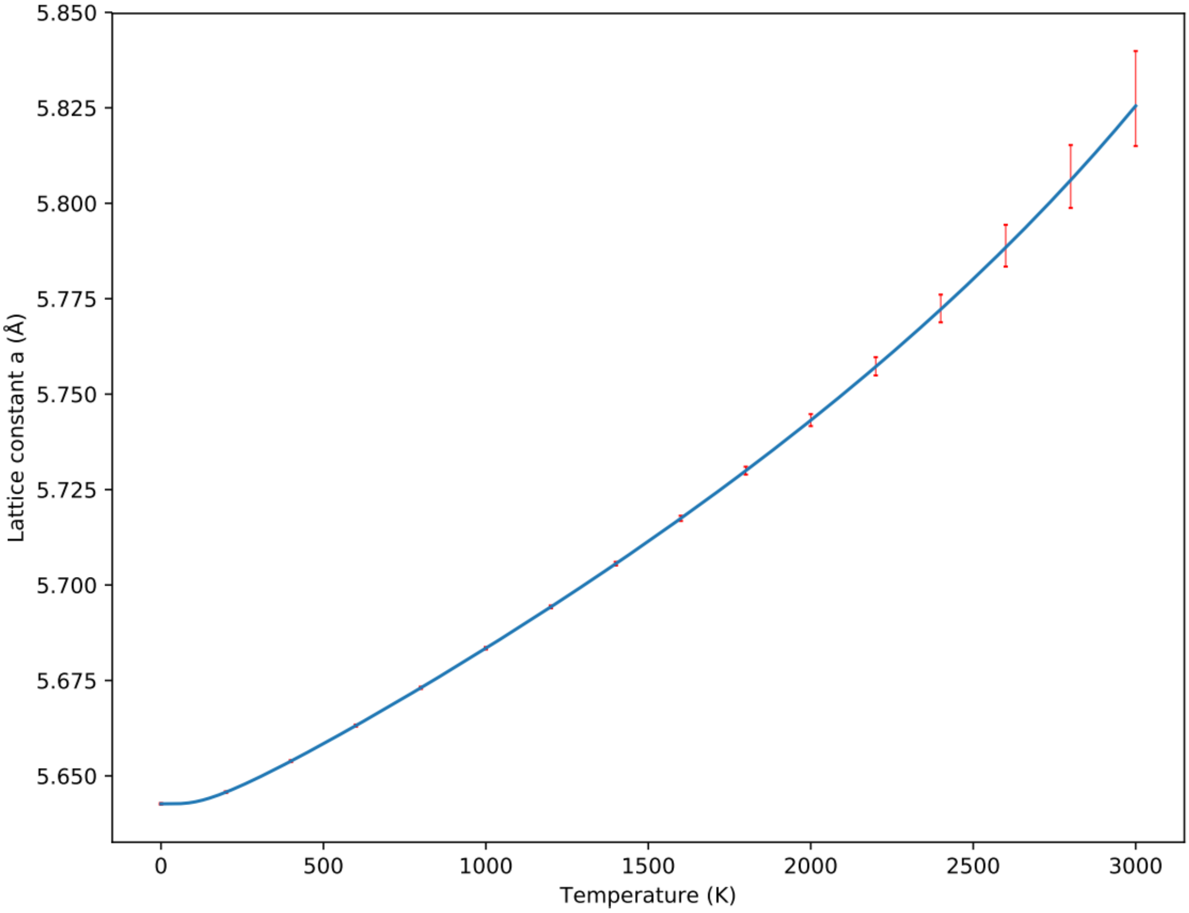

Figure 19: The lattice constant of $TiFe_2Si$ as a function of temperature with error bars. The uncertainty gets very big at high temperatures resulting from the free energies from the 7 % larger volume which were only calculated from two canonical configurations.

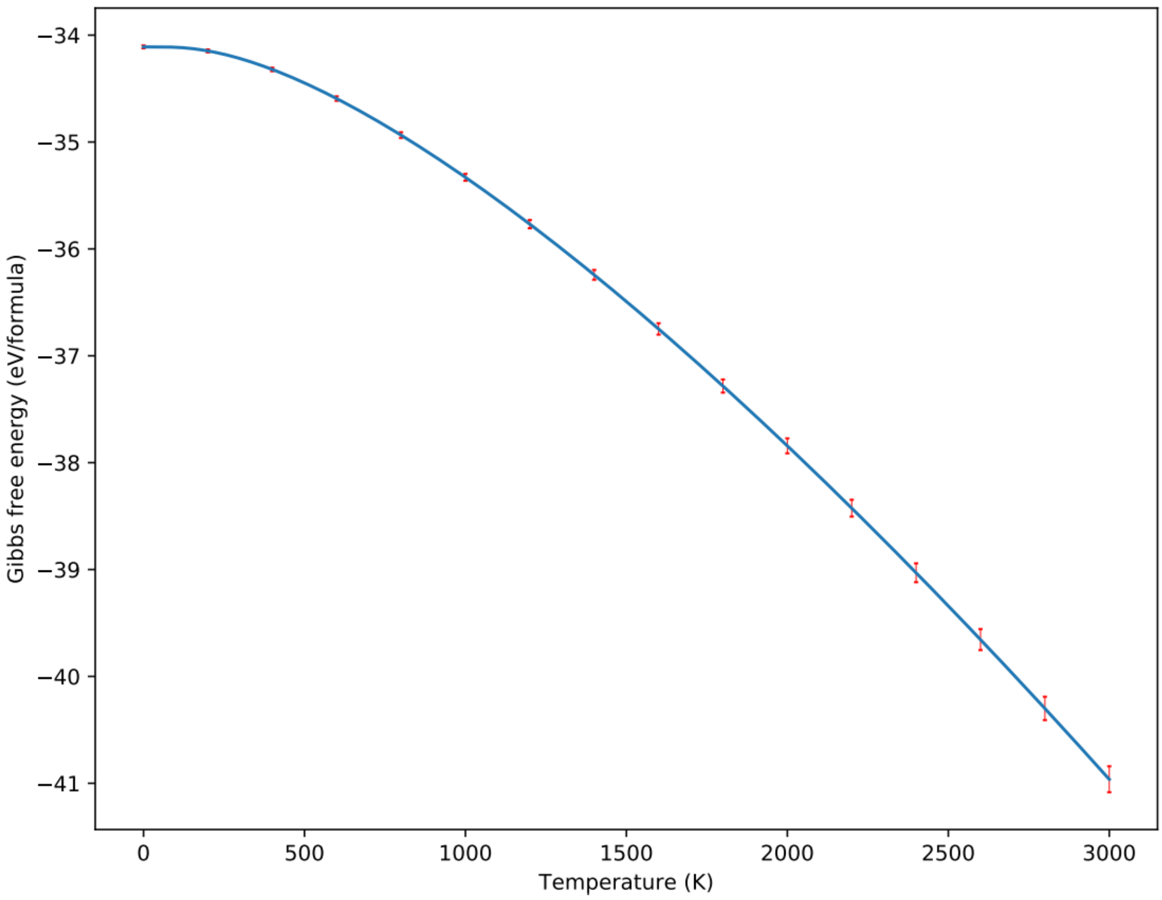

Figure 20: Gibbs free energy per formula unit at 0 pressure as a function of temperature for $TiFe_2Si$.

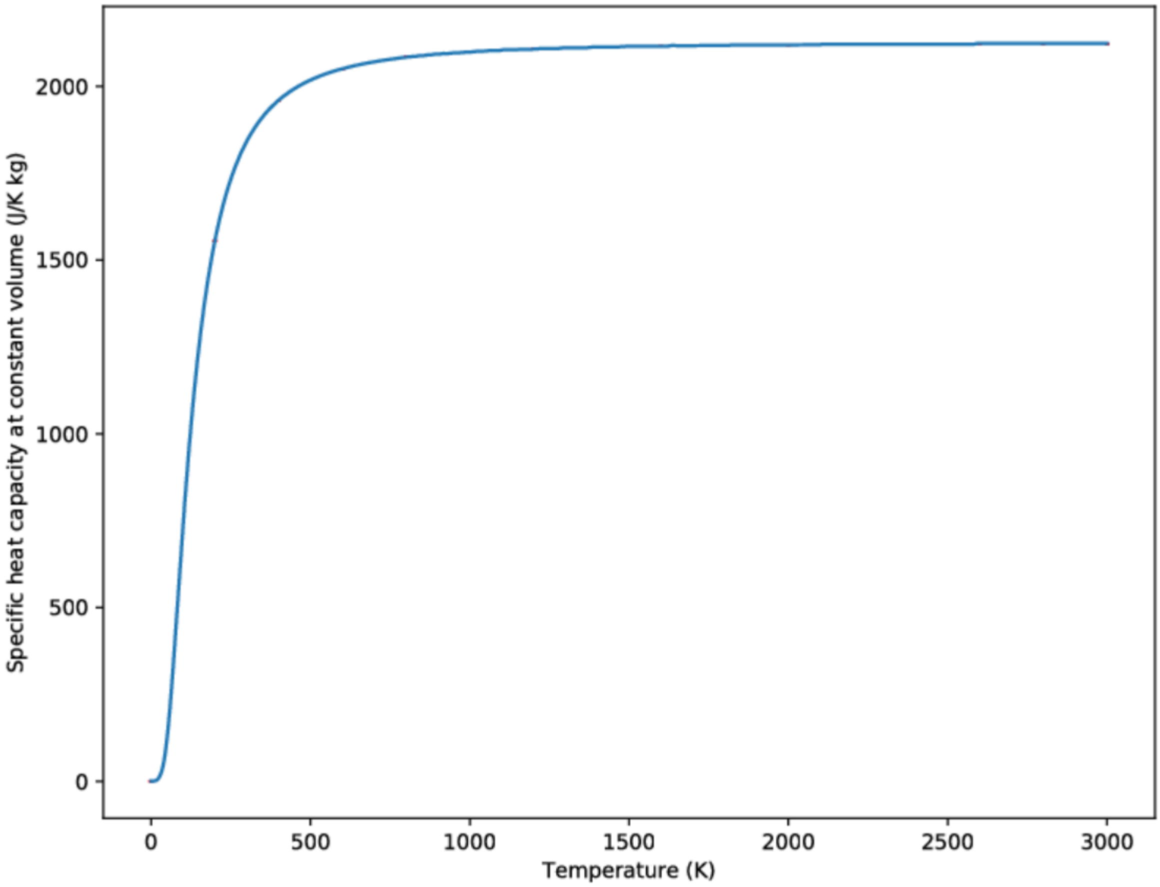

Figure 21: Specific heat capacity at constant volume for $TiFe_2Si$.

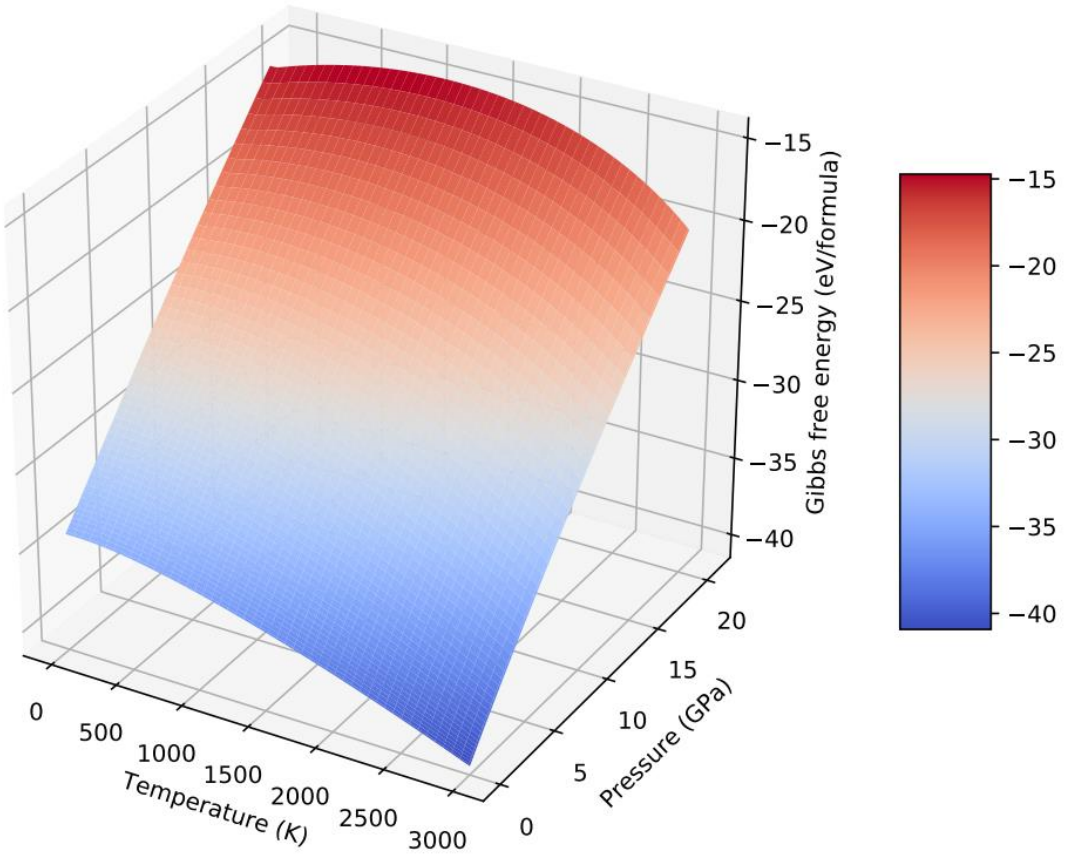

Figure 22: Gibbs free energy as a function of temperature and pressure for $TiFe_2Si$.

4.3. Results of $GaNaTe_2$

The CTE of β-$GaNaTe_2$ is shown in Figure 23 and Figure 24. As this material is tetragonal, the CTE is different in the direction of the a-lattice parameter and the c-lattice parameter. The uncertainty origins are shown in Table 5. This was the structure of $GaNaTe_2$ which did have inversion symmetry and therefore the second term of the pyroelectric coefficient equal to zero. These CTEs only goes up to 600 because the unit cells only were expanded up to 3 percent, while the expansion started to exceed this around 600 K. The lattice parameters and the Gibbs free energy at 0 pressure are shown as functions of temperature in Figure 25, Figure 26 and Figure 27 respectively. The heat capacity as a function of temperature and the Gibbs free energy as a function of temperature and pressure are shown in Figure 28 and Figure 29 respectively.

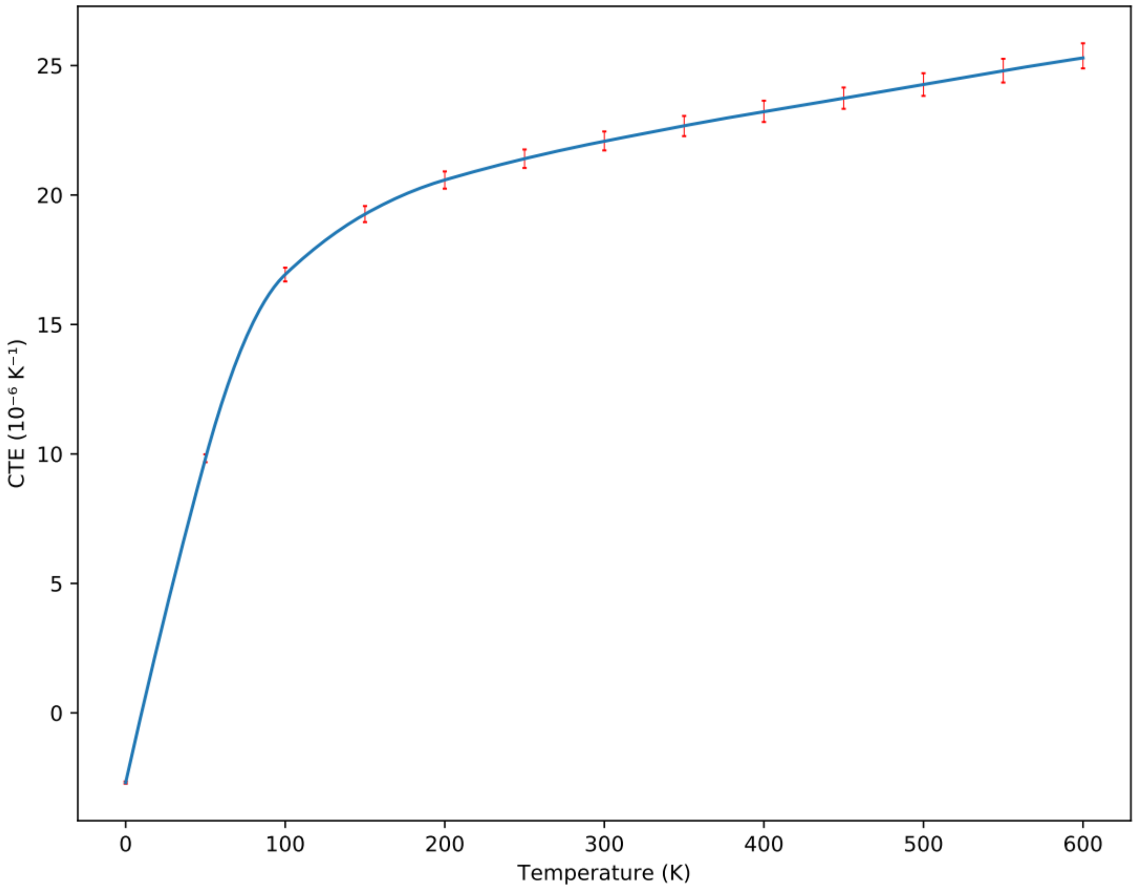

Figure 23: Coefficient of thermal expansion for β-$GaNaTe_2$ along the a-lattice parameter plotted with error bars.

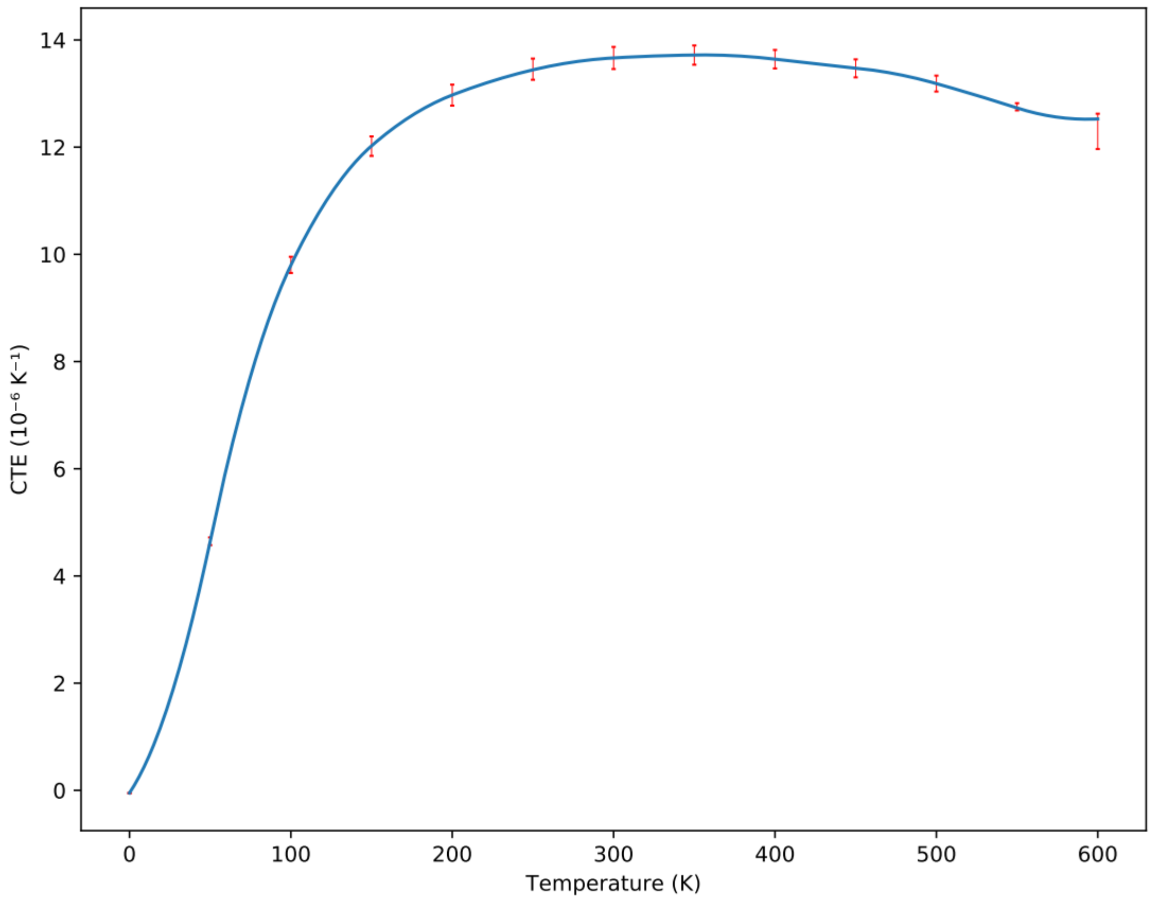

Figure 24: Coefficient of thermal expansion for β-GaNaTe₂ along the c-lattice parameter plotted with error bars.

Table 5: Uncertainties in the energy of β-GaNaTe₂ which are used to calculate the uncertainties of the other properties.

Uncertainty origin:	Energy cutoff	K-point density	Total uncertainty in the static lattice	Number of configurations	Total uncertainty in phonon free energy
Uncertainty (%):	0.0114	0.00340	0.0188	0.0773	1.520

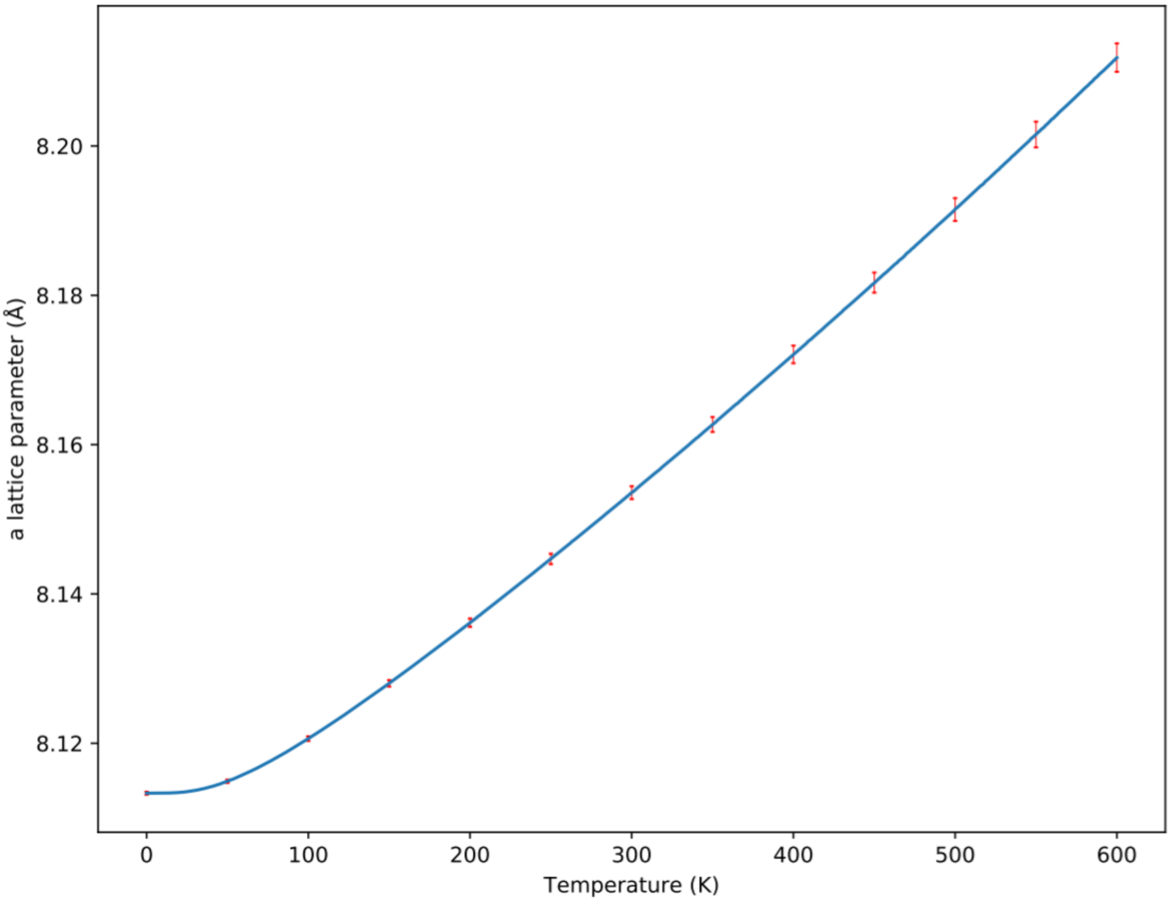

Figure 25: The a-lattice parameter of β-$GaNaTe_2$ as a function of temperature with error bars.

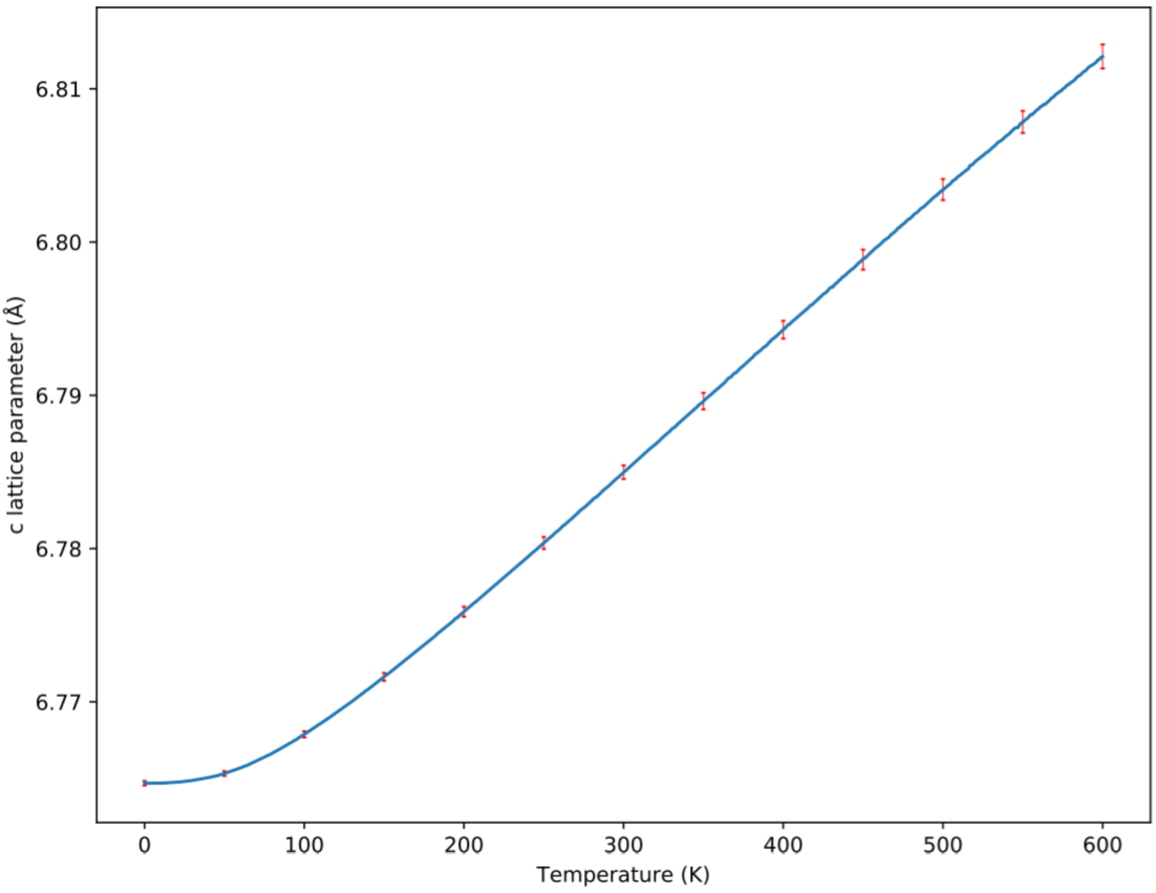

Figure 26: The c-lattice parameter of β-GaNaTe$_2$ as a function of temperature with error bars.

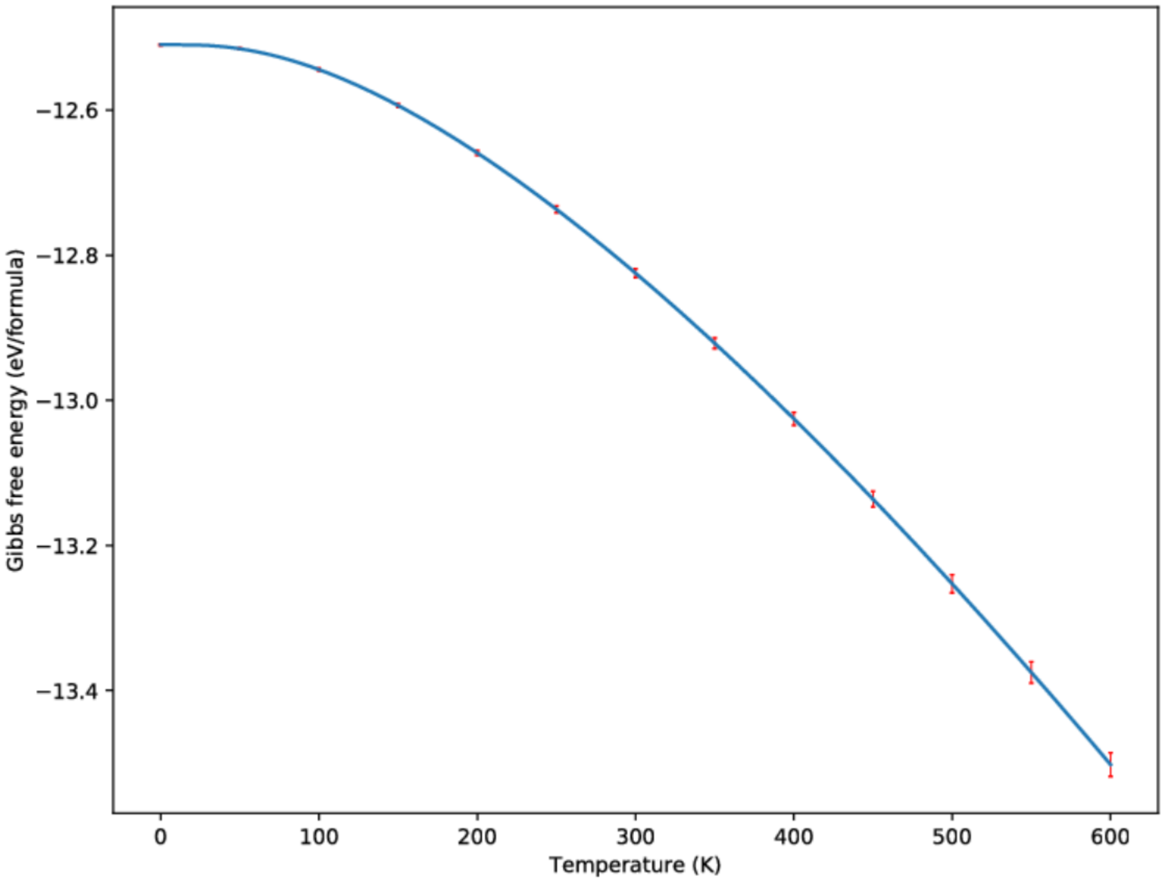

Figure 27: Gibbs free energy at 0 pressure as a function of temperature for β-GaNaTe$_2$.

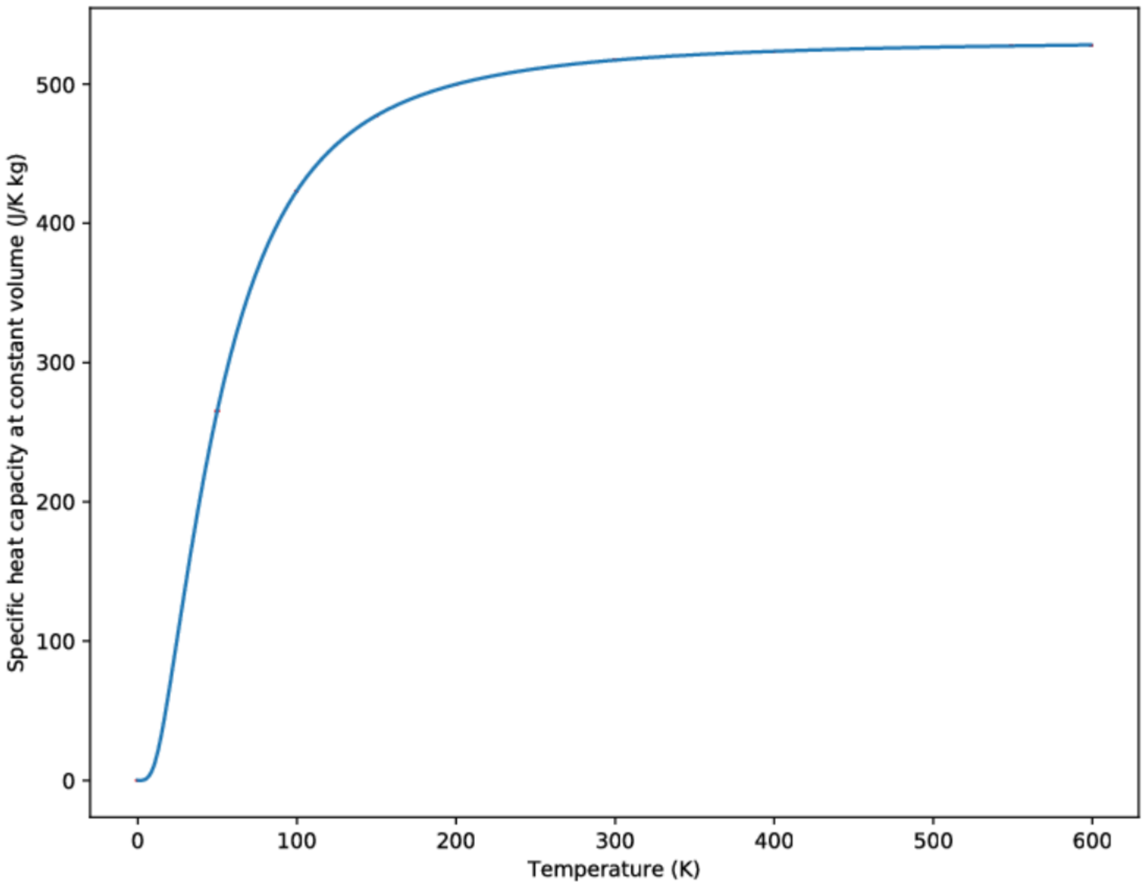

Figure 28: Specific heat capacity at constant volume for β-$GaNaTe_2$.

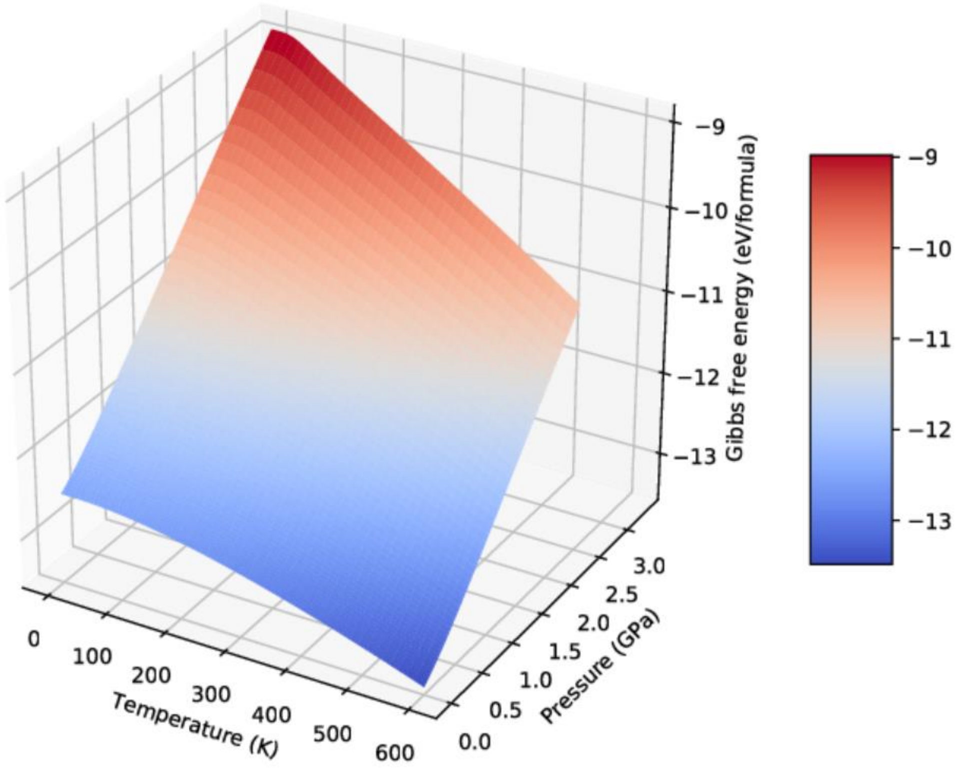

Figure 29: Gibbs free energy as a function of temperature and pressure for β-GaNaTe$_2$.

4.4. Results for GaCuSe$_2$

The CTE with respect to the a-lattice parameter and the c-lattice parameter as a function of temperature is shown in Figure 30 and Figure 31 respectively. The error bars are calculated using the uncertainties in Table 6. The lattice constants as a function of temperature are shown in Figure 32 and Figure 33. The Gibbs free energy as a function of temperature at 0 pressure is shown in Figure 34. The heat capacity as a function of temperature is shown in Figure 35. The Gibbs free energy as a function of temperature and pressure is shown in Figure 36. The components of the pyroelectric vector are shown in Figure 37. The piezoelectric tensor is shown in Table 7.

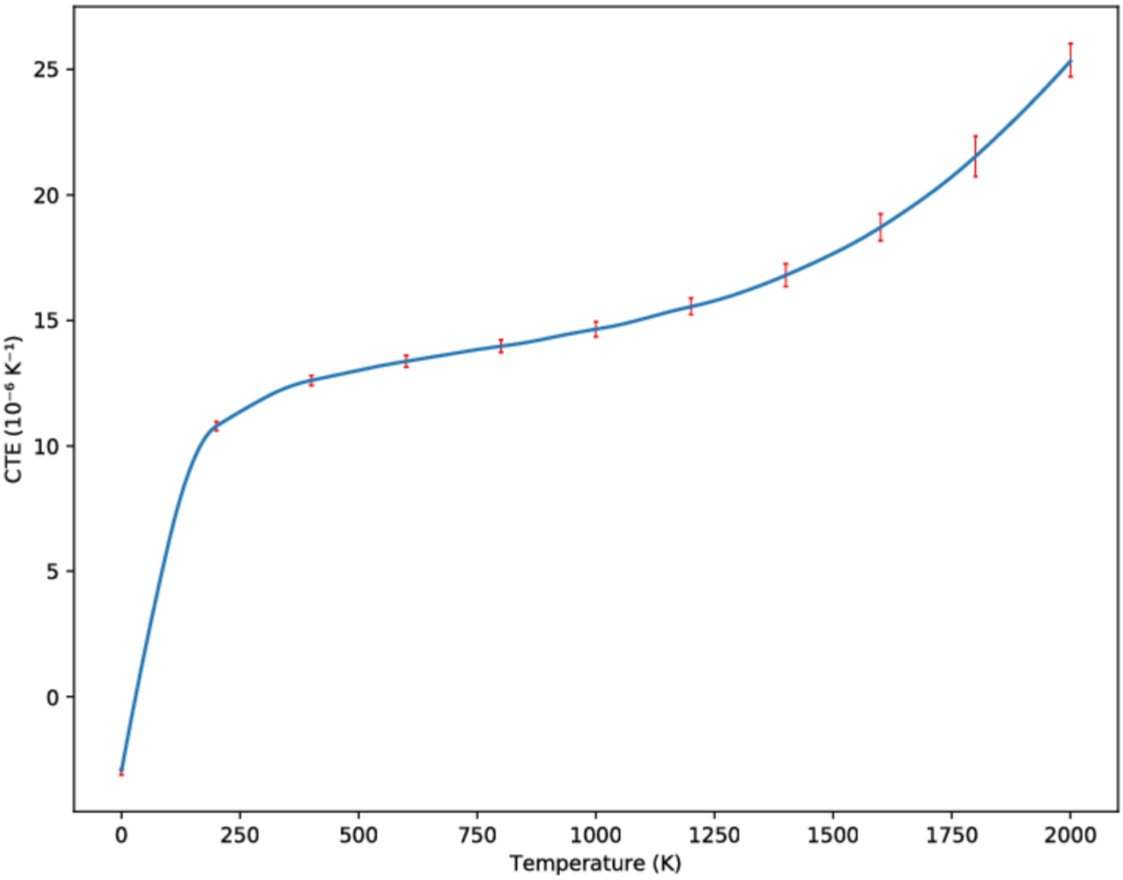

Figure 30: Coefficient of thermal expansion for $GaCuSe_2$ *along the a-lattice parameter plotted with error bars.*

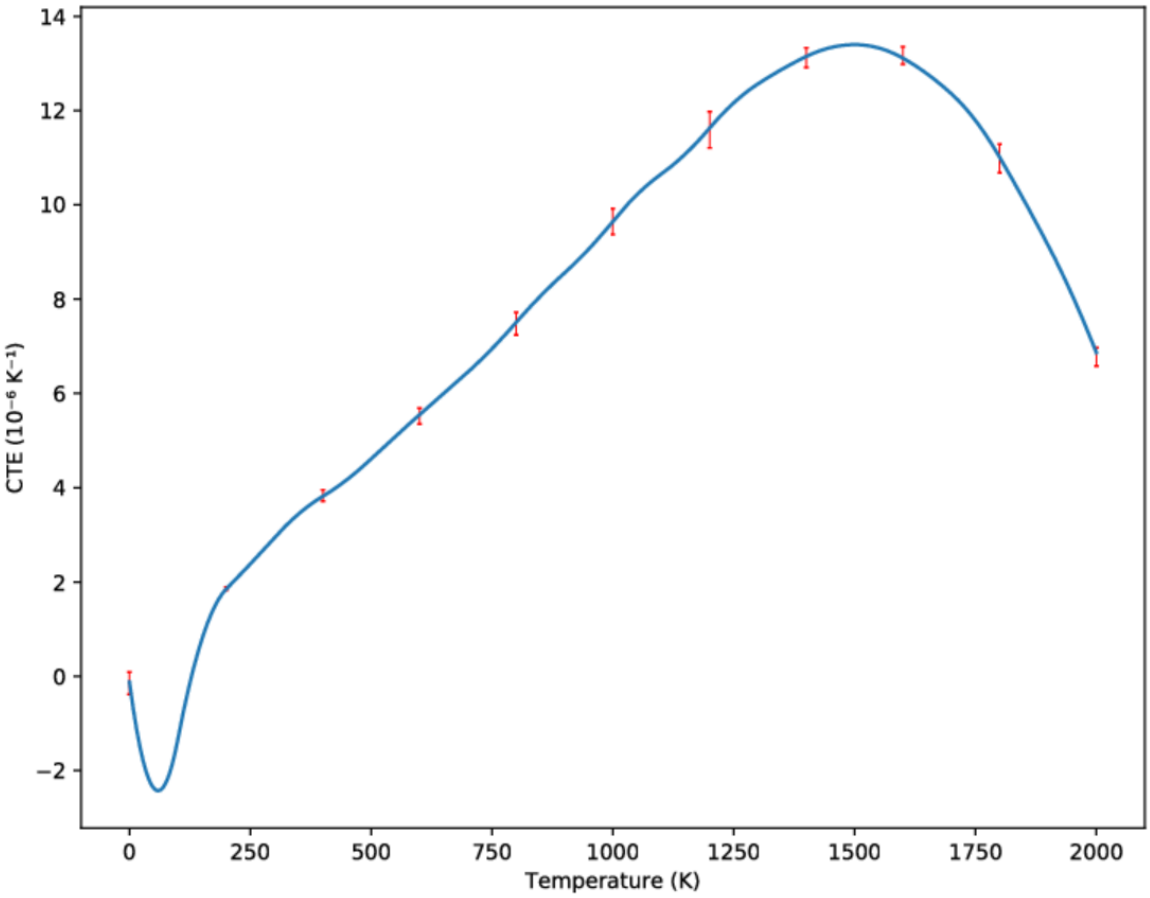

Figure 31: Coefficient of thermal expansion for $GaCuSe_2$ along the c-lattice parameter plotted with error bars.

Table 6: Uncertainties in the energy of $GaCuSe_2$ which is used to calculate the uncertainties of the other properties.

Uncertainty origin:	Energy cutoff	K-point density	Total uncertainty in the static lattice	Number of configurations	Total uncertainty in phonon free energy
Uncertainty (%):	0.0193	0.0424	0.0466	0.479	1.592

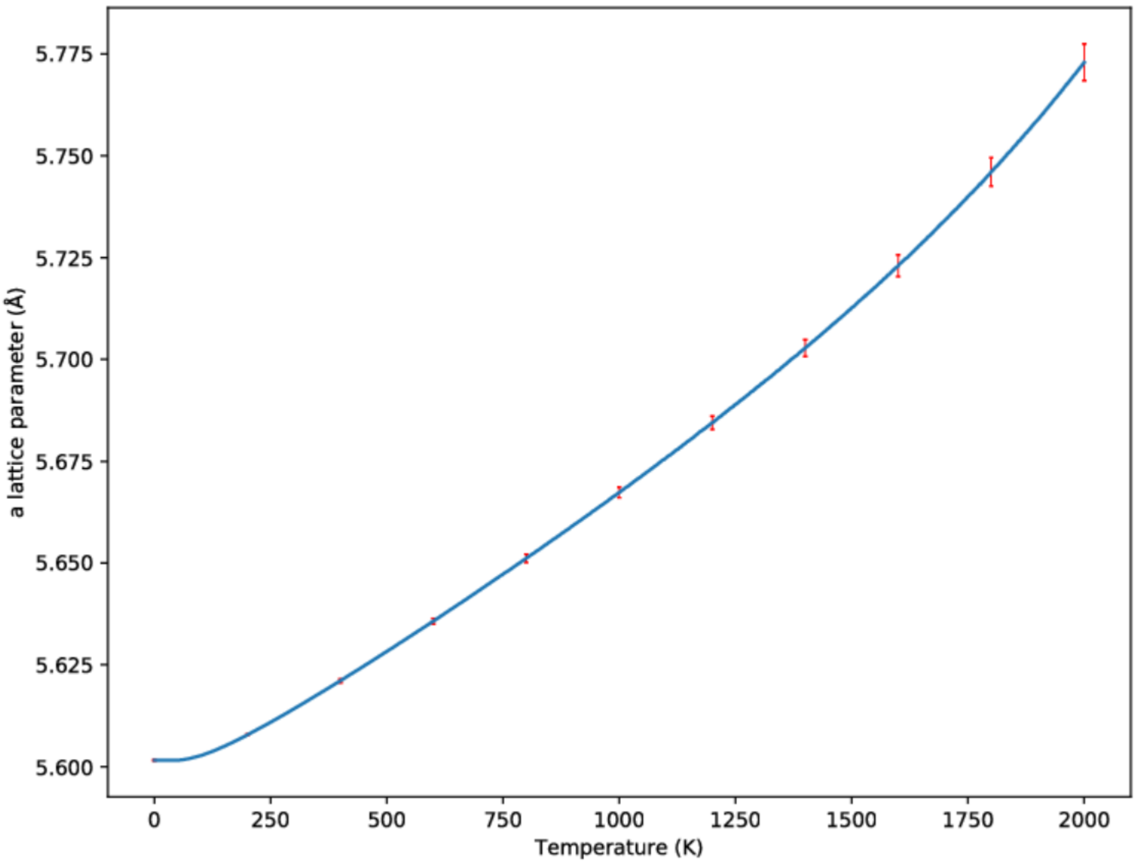

Figure 32: The a-lattice parameter of $GaCuSe_2$ as a function of temperature with error bars.

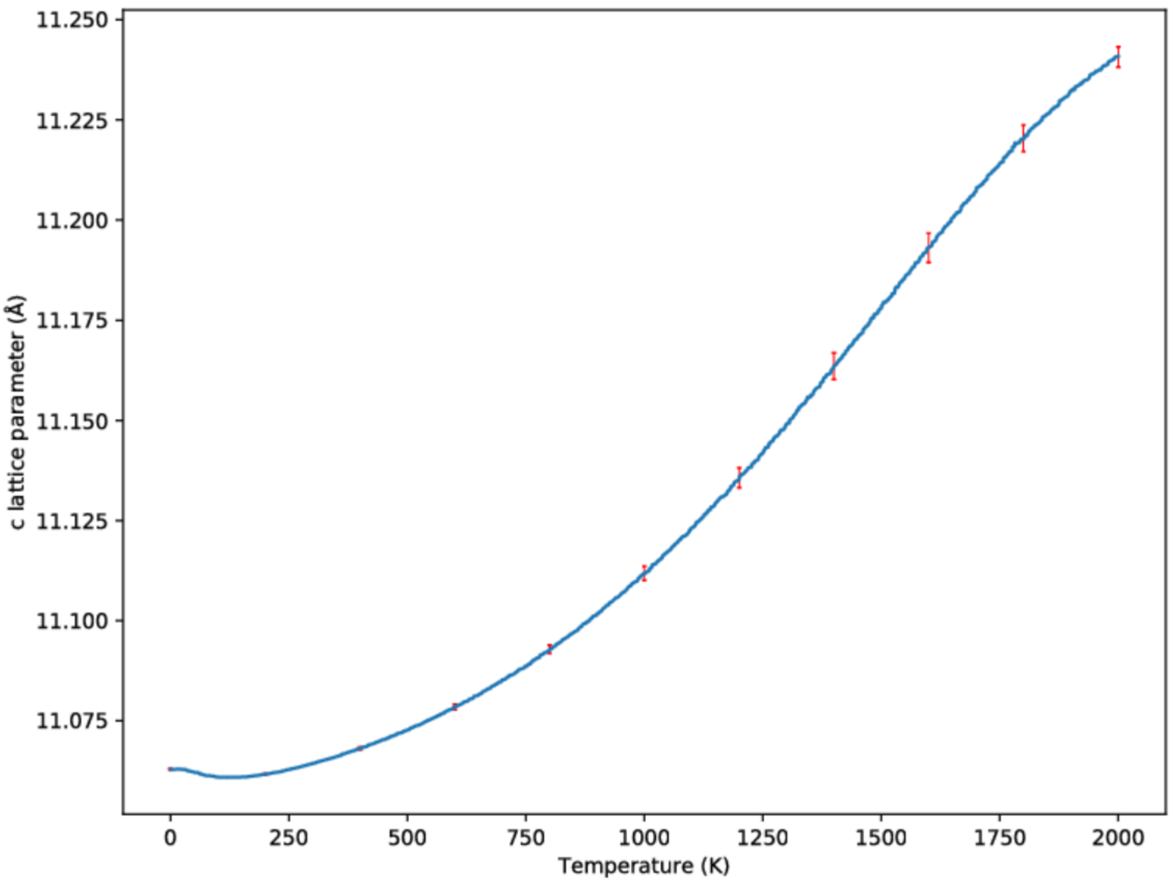

Figure 33: The c-lattice parameter of $GaCuSe_2$ as a function of temperature with error bars.

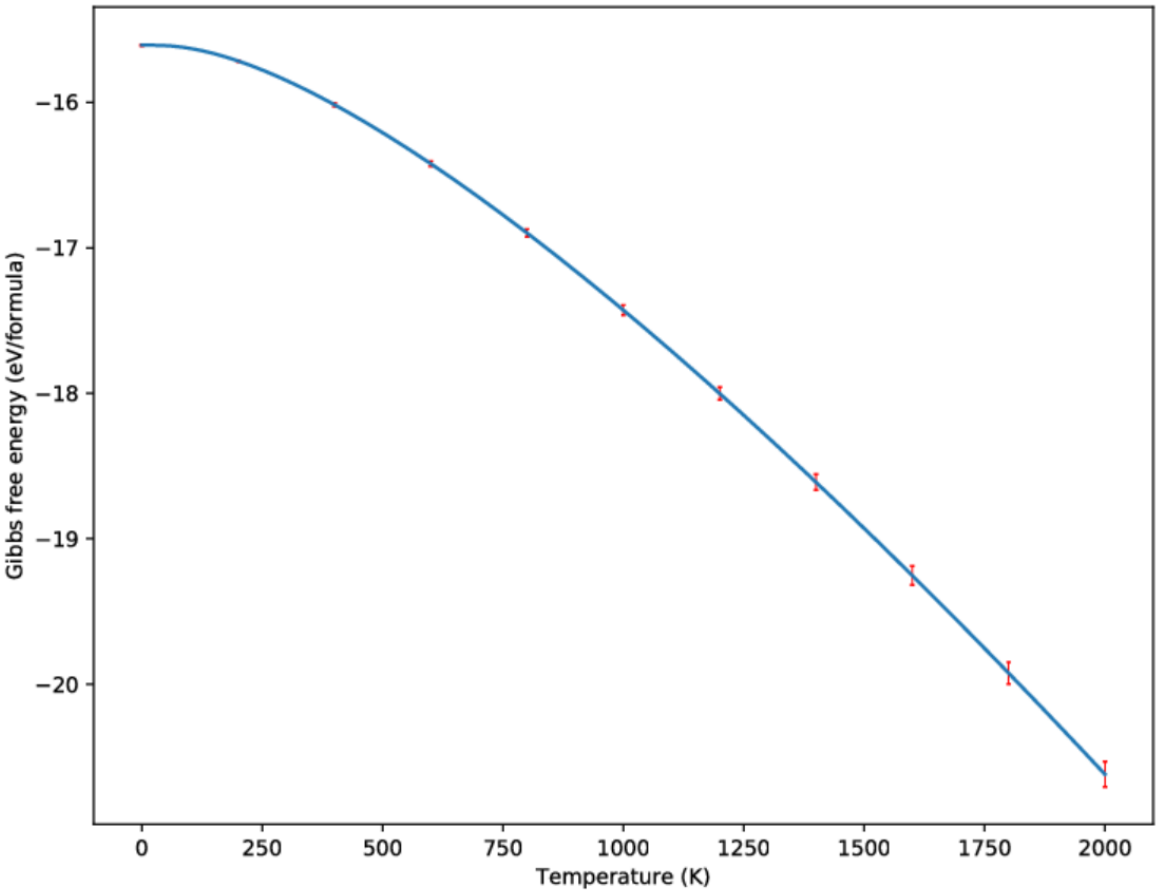

Figure 34: Gibbs free energy at 0 pressure as a function of temperature for $GaCuSe_2$.

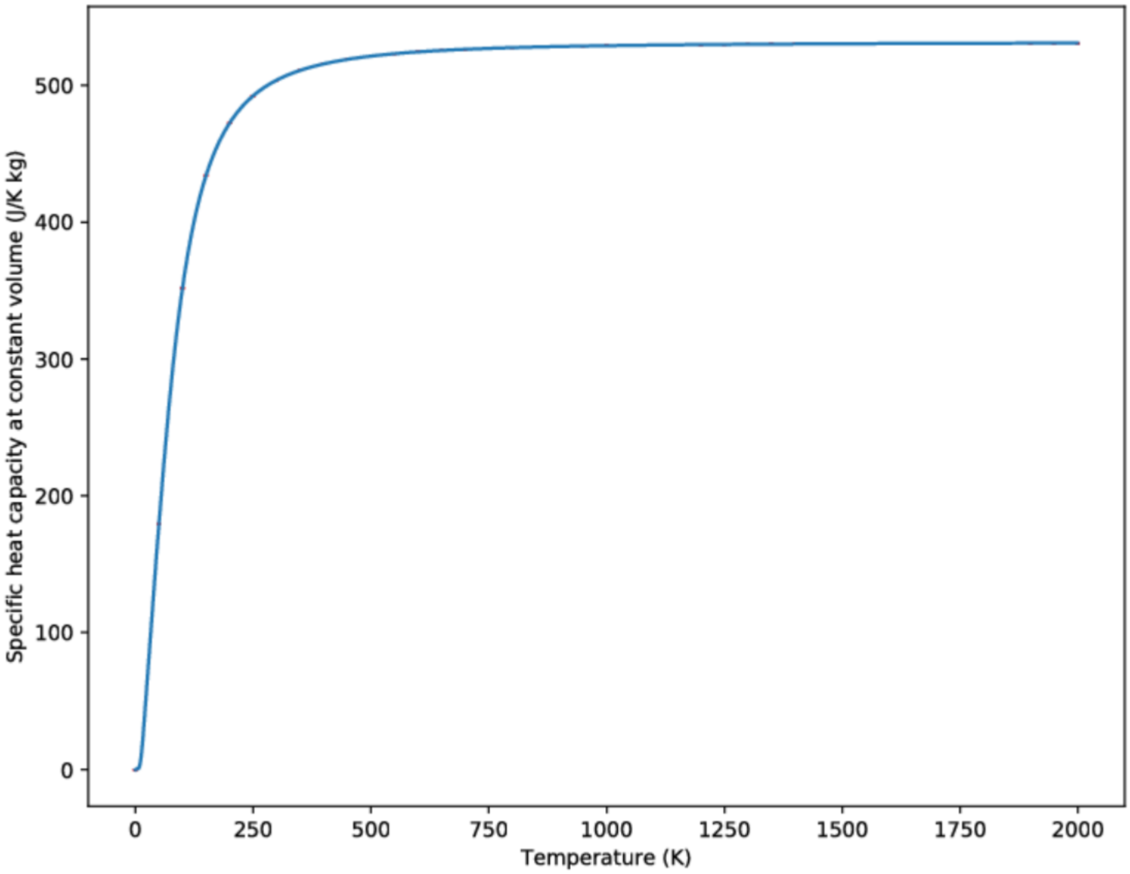

Figure 35: Specific heat capacity at constant volume for GaCuSe$_2$.

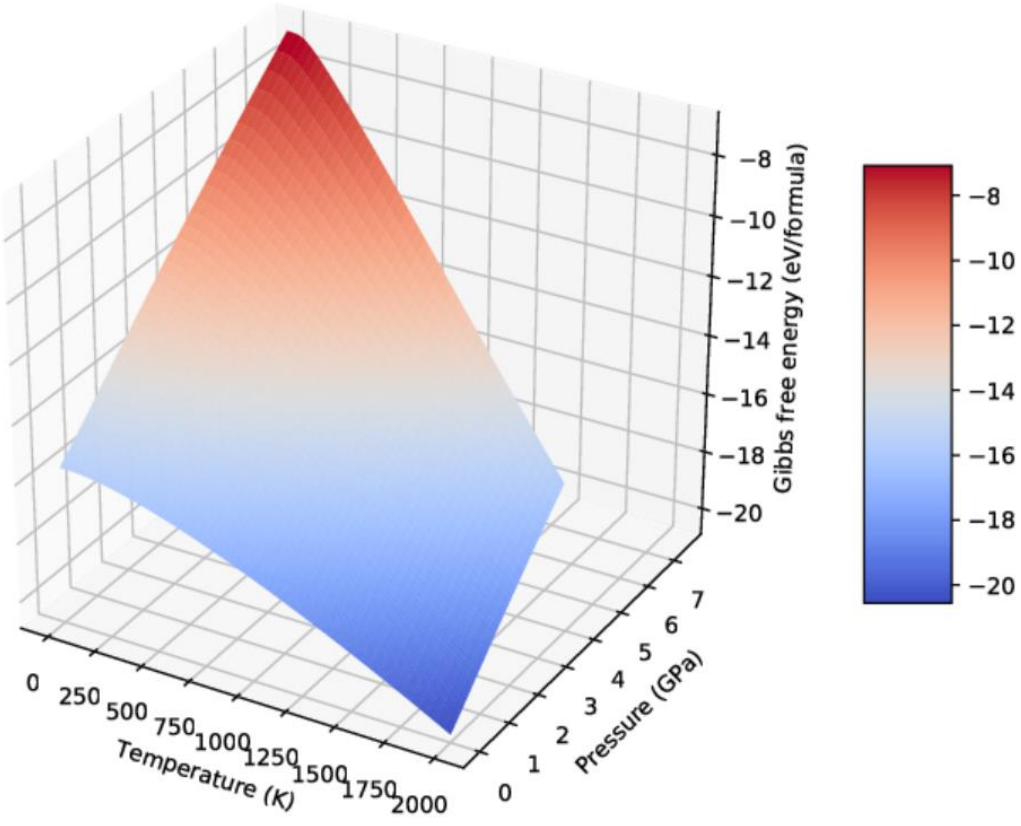

Figure 36: Gibbs free energy as a function of temperature and pressure for GaCuSe₂.

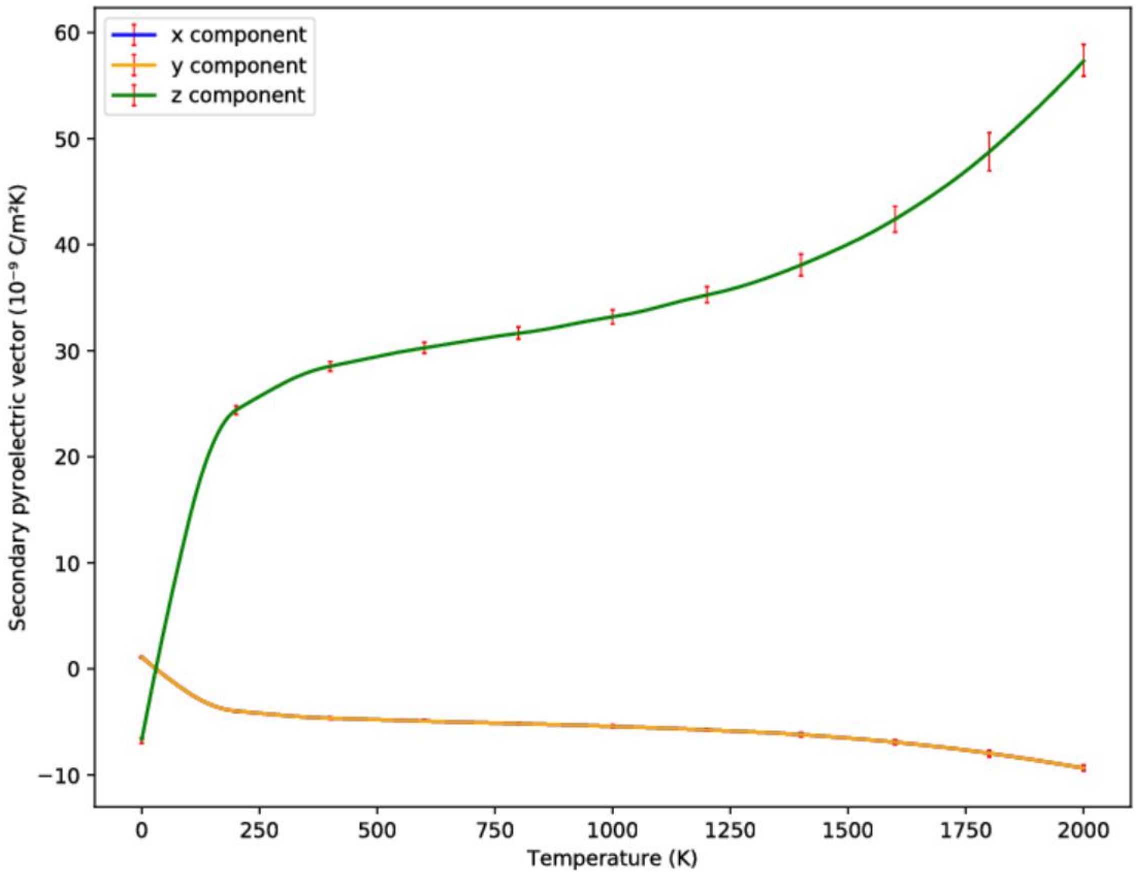

Figure 37: The components secondary pyroelectric vector for $GaCuSe_2$ as a function of temperature. The X and Y components are completely overlapping.

Table 7: The piezoelectric tensor of $GaCuSe_2$.

	XX	YY	ZZ	XY	YZ	ZX
X	-0.00072	0.00035	0	0	-0.74916	0
Y	0.00037	-0.00074	0	0	0	-0.74915
Z	0.00113	0.00113	0.00001	-2.59009	0	0

4.5. Summary of the results

The main results are plotted as a function of temperature, and in addition as a function of pressure for the Gibbs free energy. The cubic structures do only have one CTE and lattice parameter, while the tetragonal has two which gives more results. The only material with nonzero secondary pyroelectricity is $GaCuSe_2$.

5. Discussion

Diamond is the only material that had comparable data for the CTE and will be discussed first to demonstrate how well the method works. Its Gibbs free energy will be discussed briefly. The CTE of the other materials will be discussed, and their Gibbs free energy will be discussed briefly. The secondary pyroelectricity of $GaCuSe_2$ will be discussed as it was the only material with nonzero secondary pyroelectricity. The lattice parameters and the heat capacity will also both be discussed short for each material. In the end, the central processing unit (CPU) time used by each calculation will be looked at.

5.1. Discussion of coefficient of thermal expansion of diamond

Jacobsen and Stoupin have collected experimental data on the coefficient of thermal expansion for diamond and fitting models based on them to create Figure 38[58]. Their data only goes up to 2000, which is actually a little overdoing because the bulk structure of diamond only is intact up to 1800 K[58]. That means the coefficient of thermal expansion above that temperature is only a theoretical result that would have existed if the structure was unchanged. The experimental data and fitting of them in Figure 38 and the coefficient of thermal expansion from this work are put together in Figure 39 for the whole temperature range plot and Figure 40 for the low temperature plot.

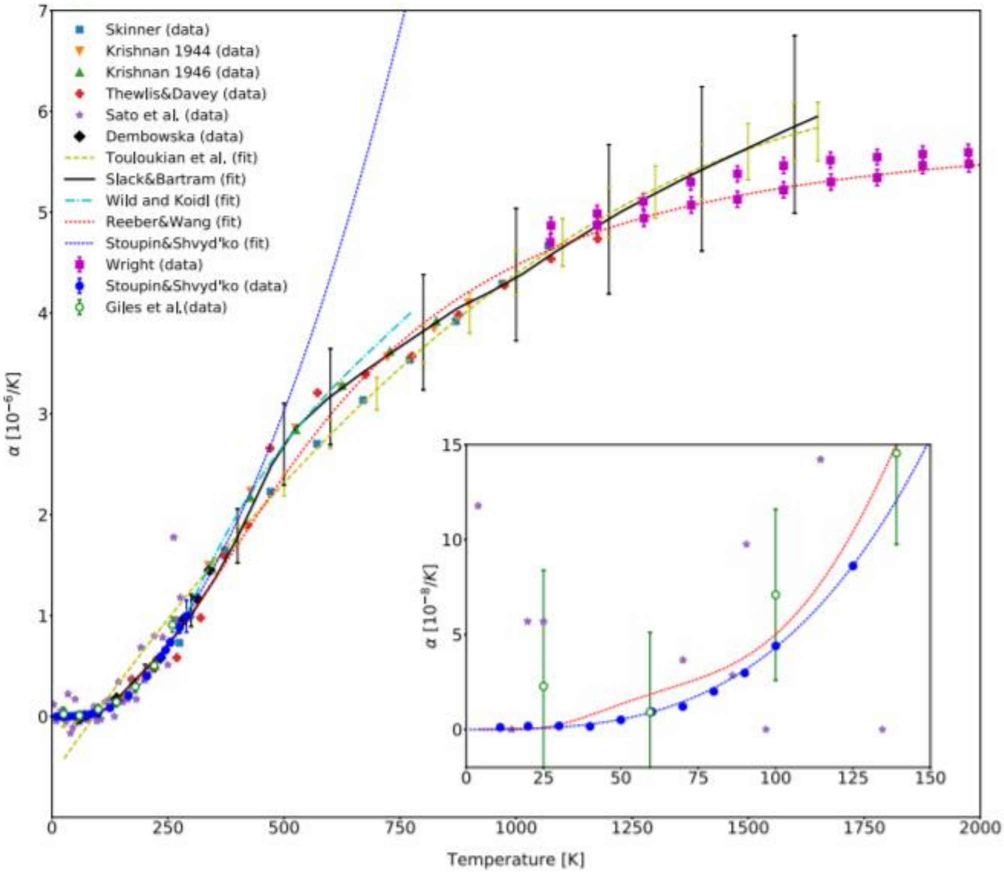

Figure 38: Collection of experimental data on the coefficient of thermal expansion for diamond and fitting models based on them[58].

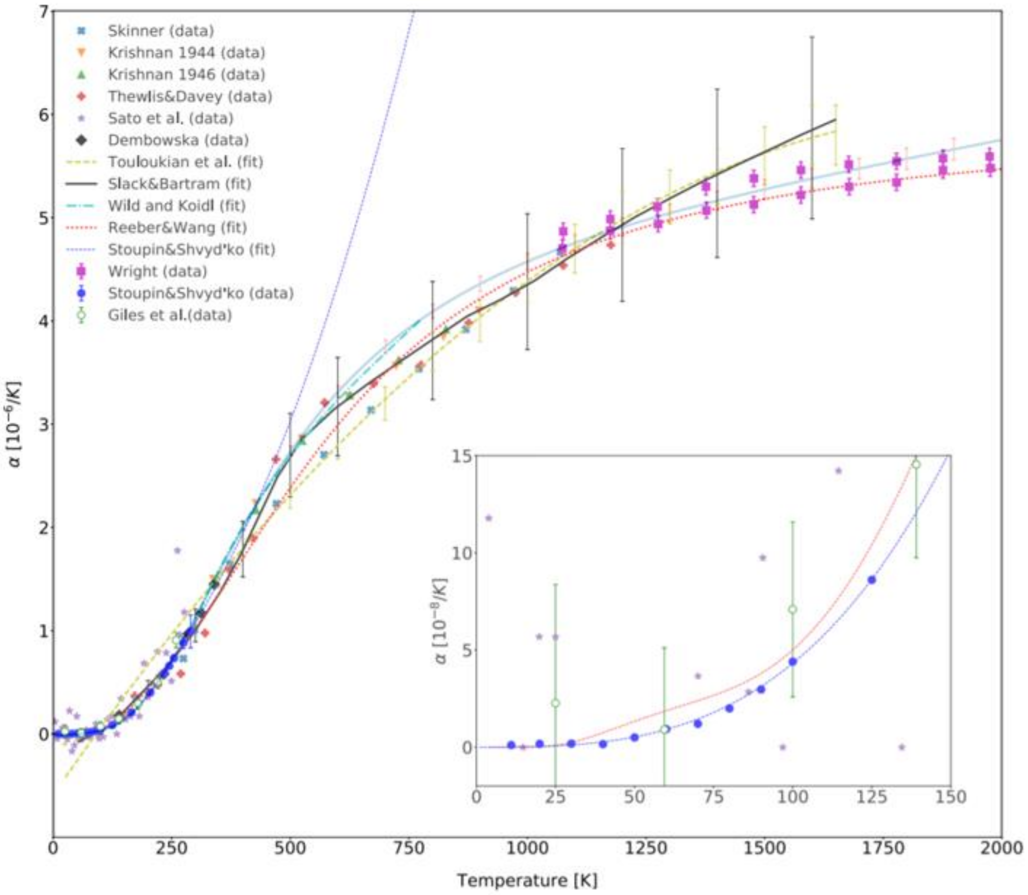

Figure 39: The collection of experimental data and fitting models shown in Figure 38[58], and the coefficient of thermal expansion for diamond from this work shown as the blue coherent line with red error bars.

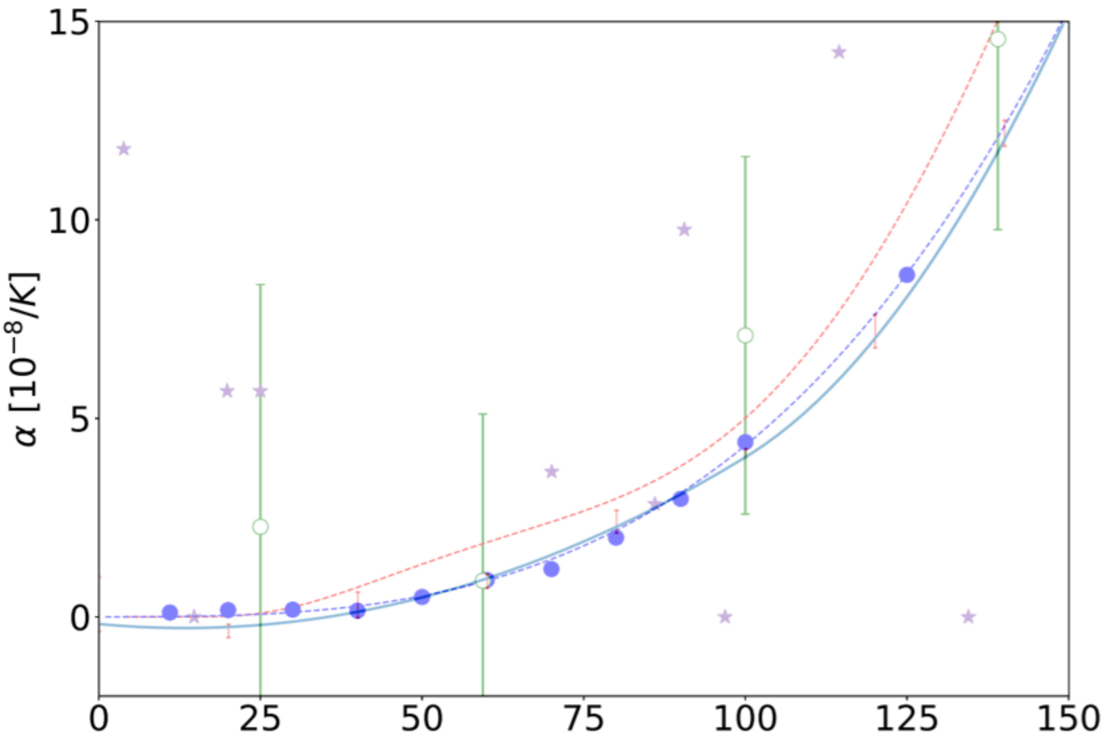

Figure 40: The low temperature plot in Figure 38 compared with the CTE from this study shown as the blue coherent line with red error bars.

5.1.1. Low temperature discussion

From Figure 39 it seems like the coefficient of thermal expansion from first principles calculated in this work agrees very well with the experimental data in the range 0 K to 300 K. The data from Stoupin and Shvyd'ko ranges from 10 K to 300 K and have an accuracy of less than or equal to $4*10^{-9}$ and was performed on synthetic diamond of type IIa that was nearly perfect with nitrogen impurities below 1 ppm and on synthetic diamond of type Ia that has impurities of nitrogen clusters with concentration in the range from 10 ppm to 3000 ppm[59, 60]. The differences in the coefficient of thermal expansion for the different diamond samples were within the measurement accuracy[59, 60]. The plotted points from these measurements in Figure 38 are the average value from the four samples[58]. The coefficient of thermal expansion of diamond in this study is based on a perfect diamond structure with no impurities, so the data from Stoupin and Shvyd'ko are good for comparison and will be used as the reliable points in its temperature range. Having a closer look at Figure 40, it is seen that the CTE from this study is not right on the points from Stoupin and Shvyd'ko at all temperatures, but it seems like they are inside or at least not far from the accuracy range. The blue stippled line which is the fit of the experimental points from Stoupin and Shvyd'ko is almost inside the shown error bars of this study for all temperatures, except below 40 K. There the CTE from this thesis is negative from 10 K to 29 K with uncertainty considered, which is not in agreement with theory[59, 61], which says that diamond should always have positive thermal expansion since it only has positive Gruneisen parameters.

Reasons that this study and the Stoupin and Shvyd'ko data do not fit perfectly can origin from multiple reasons. First, there is always an uncertainty in the calculations from VASP that is due to numerical error and an approximated energy functional which is not included in the error bars. Second, for diamond a lower energy cutoff than the converging energy cutoff limit was used, the same for the k-point density. The energy at 0 K should not be very much affected by this as it is well converged for the used energy cutoff and k-point density, but the force constants might have been more affected. Third, the method within TDEP calculates the force constants at 300 K and then uses the quasi harmonic approximation to calculate the phonon free energy at all temperatures from 0 K to 3000 K. This is beyond the normal quasi harmonic approximation as the force constants normally originates from 0 K calculations. However, to go even further, the force constants could have been calculated at more temperatures, and been interpreted between the points by the quasi harmonic approximation e.g. Even more, the force constants could have been calculated at all temperatures. Fourth, the materials in the present study are in a completely perfect structure, which does not exist in reality.

5.1.2. Middle temperature discussion

In the temperature range from about 300 K to 1000 K, the spread in the points is less than 10 %[58]. The coefficient in this study seems to be bit larger than these points, at least after 600 K, but well inside the spread of 10% comparing the error bars from Slack and Bartram's[62] fit which is at 15%. The Skinner data and the Thewlis and Davey data do at least have one point in the range of Stoupin and Shvyd'ko data. Comparing these points, the Skinner data and the Thewlis and Davey data are a little bit lower than the Stoupin and Shvyd'ko data and outside their accuracy range. Stoupin and Shvyd'ko claim to use a very pure diamond structure[59, 60] which makes it very comparable to this study. Skinner used two different samples, one that was a commercial grade that consisted of many corns less than one micron from many different diamonds[63]. The purity of this sample is not stated, however, the other sample was a colourless piece from an south west African diamond and described as exceptionally pure[63] although the diamond stuctures used in Stoupin and Shvyd'ko's studies are a lot purer. The content of the south west African diamond piece is shown in Table 8. The data are from 5 spectrographic analysis of the one area of the sample, each independent of each other[63]. The Skinner data have an accuracy of 0.3 % for each sample[63], that means the thermal expansion obtained here is out of the accuracy range. It is not stated if the points from Skinner in Figure 38 are from the commercial grade diamond, the south west African diamond or an average of these. The variation in the coefficient of thermal expansion for those samples is as big as 10 %[63].

Table 8: Impurities in the south west African diamond from Skinner's studies[63].

Analysis number	Impurities in ppm.					
	Mg	Si	Fe	Al	Cu	Ca
1	2	20	1	10	<1	2
2	1	10	1	<10	<1	4
3	15	40	2	<10	<1	<0.5
4	4	<10	<0.5	<10	<1	<0.5
5	2	150	5	<10	<1	<0.5

The first three points of Krishnan's studies in the range from 300 K to 1000 K, seem to be close to or on the line from the present studies in Figure 39. There is found no information about the purity of the diamond used in the studies published in 1944[64], either because it is not stated or because part of the article is not accessible. In Krishnan's article from 1946 it is stated that the diamond used is opaque to ultra-violet radiation and has the least fluorescence[65]. Further it is stated that these diamonds are shown to have the least angular divergence, which is just a little higher than that of the ideal crystal[65]. However, the exact pureness of the diamond used is not stated. The coefficient of thermal expansion Krishnan's study is a mean from a range of 100 K, which starts at about 300 K and ends at about 878 K, which also raises the uncertainty of the points actual value. The uncertainty in the points from Krishnan's articles is not stated, but the points from his two studies corresponds very well.

5.1.3. Critic of most samples' pureness

Sato et al.[66] also ask questions to the investigations of diamond's lattice parameter performed before Skinner's study in 1957. They state that the samples used at that time were not chemically analysed and if they were it was not investigated if the impurities were macroscopic clusters or spread out as vacancies. Further they compared the thermal expansion between a diamond of the same type as Stoupin and Shvyd'ko's diamond, which they also investigated with infrared spectroscopy to verify that the nitrogen concentrations was below a few ppm, with two less pure diamonds in the temperature range from 4.2 K to 300 K. One with nitrogen impurity of about 100 ppm, and the other with boron impurity of about 100 ppm. From about 160 K and above, their thermal expansion of pure diamond was larger than the thermal expansion of both the less pure diamonds as shown in Figure 41. This can be an explanation to why the thermal expansion obtained here is larger than the compared ones for temperatures above 300 K. The accuracy of Sato et al.'s lattice parameter was 10^{-6}, and the accuracy of the temperature was within 0.1 K.

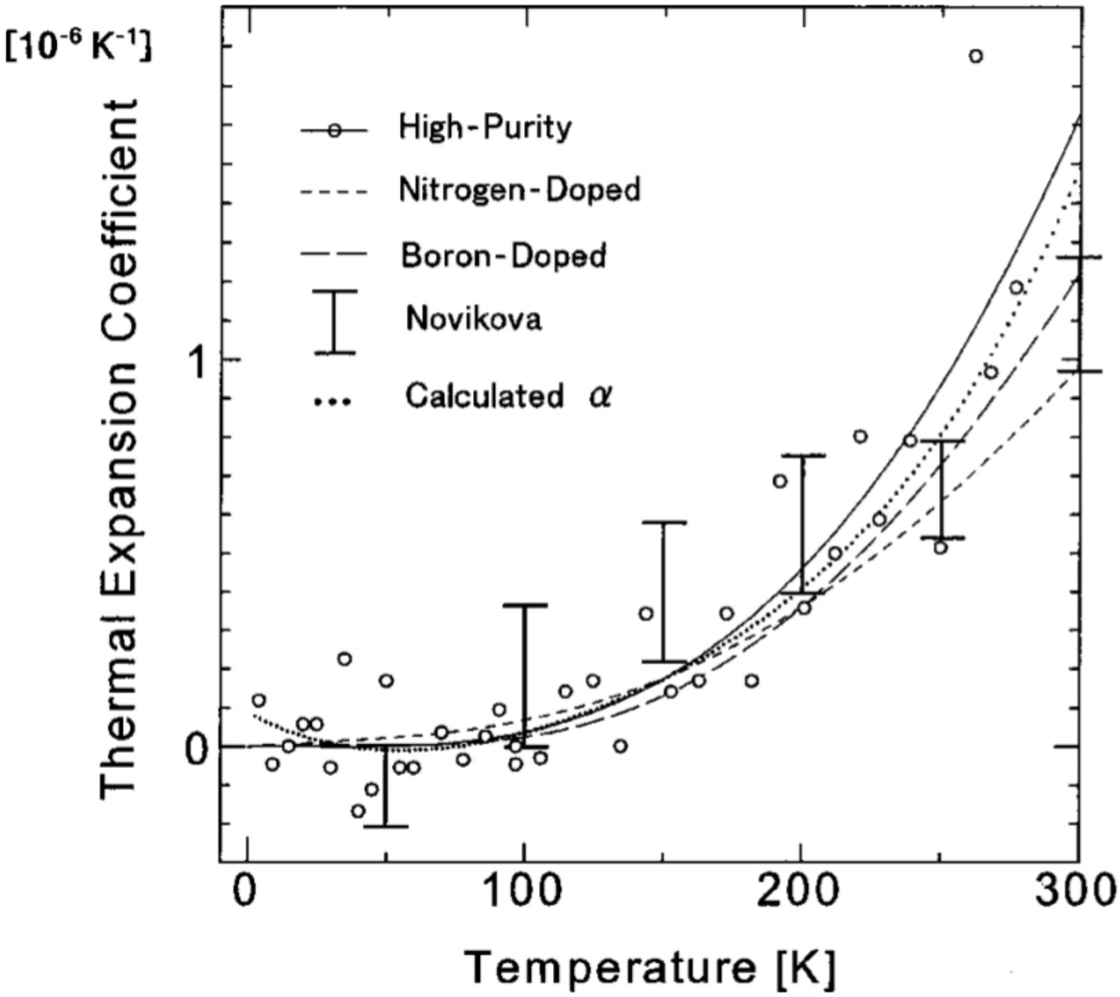

Figure 41: Thermal expansion coefficient of diamond from Sato et al.'s studies[66].

For temperatures above 1000 K, this study's coefficient of thermal expansion seems to fit well with the experimental data.

5.1.4. Discussion of other theoretical methods

There have been other theoretical attempts to calculate the coefficient of thermal expansion of diamond. Pavone et al.[38] used density functional perturbation theory with LDA as the exchange correlation potential along with plane waves as the basis set and nonlocal pseudopotentials to calculate the lattice constant of diamond at 0 K, as well as the phonon dispersion curves and phonon eigenvectors. The force constants were calculated considering displacements of an atom as a periodic perturbation. Further the quasiharmonic approximation was used to calculate the thermal expansion, using the expression $\alpha(T)=\frac{1}{3V}\frac{\partial V}{\partial T}\approx\frac{1}{B_0}\sum_{\boldsymbol{q},j}\gamma_j(\boldsymbol{q})c_{vj}(\boldsymbol{q},T)$ where B_0 is the bulk modulus at equilibrium, $c_{vj}(\mathbf{q},T)$ is the contribution of the mode **q**j to the specific heat at constant volume and $\gamma_j(\mathbf{q})$ is the mode Gruneisen parameter, for the coefficient of thermal expansion from 0 K to 1600 K as shown in Figure 42. Compared to the slope from this study it seems to be below already at around 150 K with the distance between the slopes becoming bigger and bigger as the temperature raises. After 750 K it deviates more and more even from the lowest experimental values. At lower temperatures it is very similar to the CTE of this study except, it does not have negative CTE below 40 K which is in agreement with theory and experiment[59-61].

Another study used almost the same approach as Pavone et al. to calculate the coefficient of thermal expansion of diamond with quite different results. Mounet and Marzari[67] used a combination of DFT and DFPT with GGA as the exchange correlation potential with plane waves as the basis set and ultrasoft pseudopotentials from Vanderbilt[68] to calculate the lattice constant at 0 K, the phonon dispersion curves and interatomic force constants. PBE[69] was the type of GGA used. The quasiharmonic approximation was used to calculate the coefficient of thermal expansion from 0 K to 3000 K. However, the method in finding the coefficient of thermal expansion differs from Pavone et al.'s method. Mounet and Marzari calculated the Helmholtz free energy and the phonon frequencies as a function of the lattice parameter. Then the free energy could be minimized directly as a function of the lattice parameter to find its length at any temperature. The coefficient of thermal expansion was found through numeric differentiation.

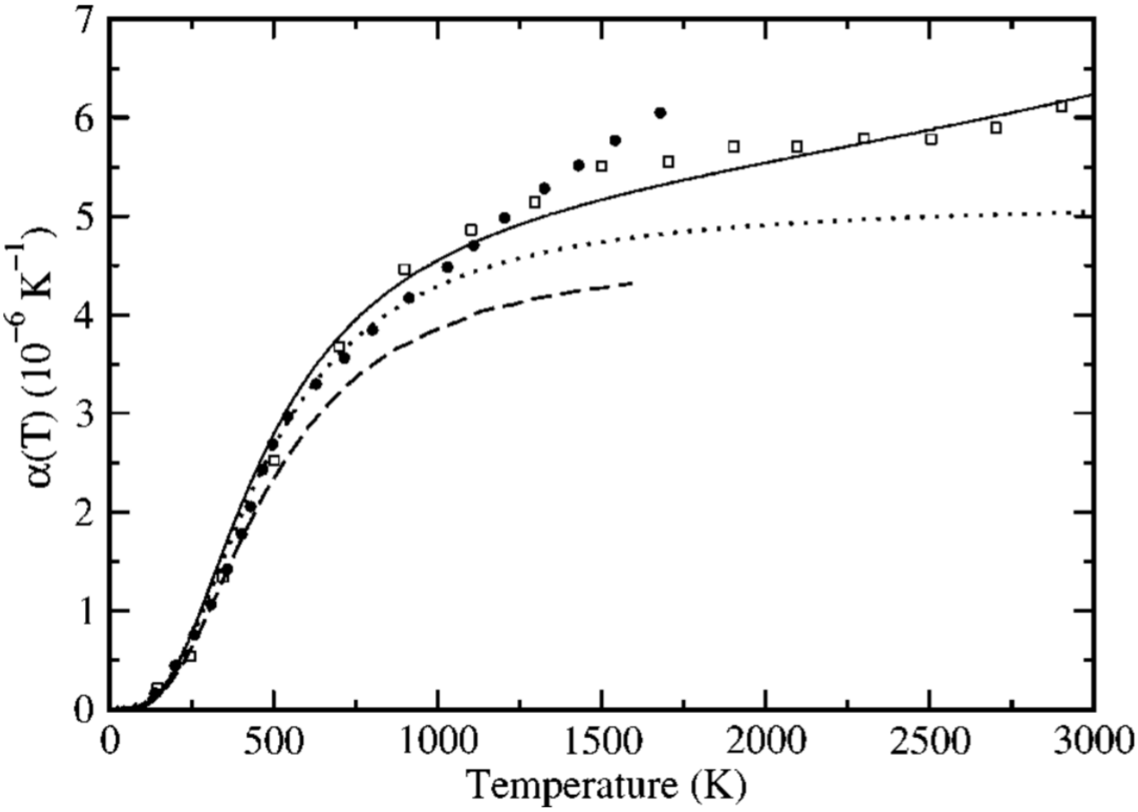

Figure 42: CTE of diamond from Pavone et al.’s[38] *study as the dashed line, Mounet and Marzari’s*[67] *as the solid line, experimental points from Slack and Bartram*[62] *as the filled circles, a path integral Monte Carlo study from Herrero and R. Ramírez*[70] *as the open squares and the dotted line is Mounet and Marzari’s study as well calculated from the analytical expression Pavone et al. used.*

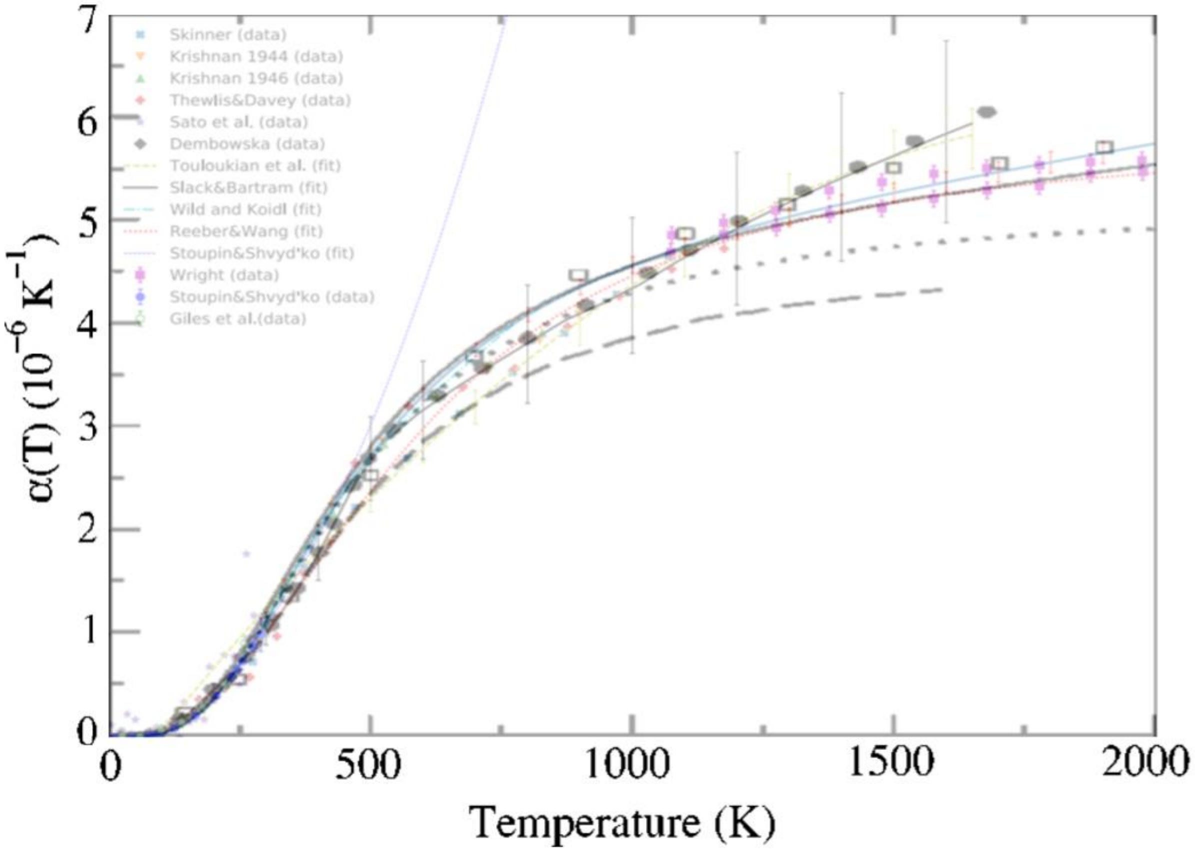

Figure 43: The collection of theoretical CTEs of diamond in Figure 42 in the same plot as the CTE of diamond from this study, and the experimental collection of from Jacobsen and Stoupin[58], in the temperature range from 0 K to 2000 K.

From Figure 43 it is seen that the CTE from Mounet and Marzari is very close to the CTE of this study all the way. From about 1500 K it goes outside the accuracy range of this study. Also it does not have a negative CTE even at the lowest temperatures, which is in agreement with theory and experiments[59-61].

5.2. Discussion of Gibbs free energy of diamond

From Figure 15 it is seen that the Gibbs free energy of diamond becomes lower and energetically more favorable as the temperature increases. Figure 17 also shows that the Gibbs free energy generally gets lower at lower pressures and higher temperatures. It also shows that when the pressure increases the Gibbs free energy gets a local minimum with respect to temperature between 0 K and 500 K.

5.3. Discussion of $TiFe_2Si$

The CTE of $TiFe_2Si$ is large as the temperature grows compared to diamond. The shape of the curve is however very similar to the curve of diamond. It is small close to 0 K then grows fast from about 40 K to about 300 K. This behavior is seen clear from Figure 44. After 300 K it grows more slowly while it grows faster and faster as it reaches higher temperatures. From Figure 45 it is seen that even though the curve is negative for the lowest temperatures, the uncertainty goes very close up to 0 K^{-1}. Checking the uncertainties from 0 K to 10 K more closely, it is seen that the maximum uncertainty is slightly above 0 K^{-1} also in that range. Therefore, it cannot be concluded if the CTE of $TiFe_2Si$ is negative at the lowest temperatures according to this study. Note that the uncertainty is relatively big for the smallest temperatures. This is probably the first study of CTE of $TiFe_2Si$, therefore there is no data of this material to compare with. However, similar materials will be used for comparison. The material was reported metastable by V. Raghavan[28], so it was decided that it was not worth to try to find another phase that was pyroelectric.

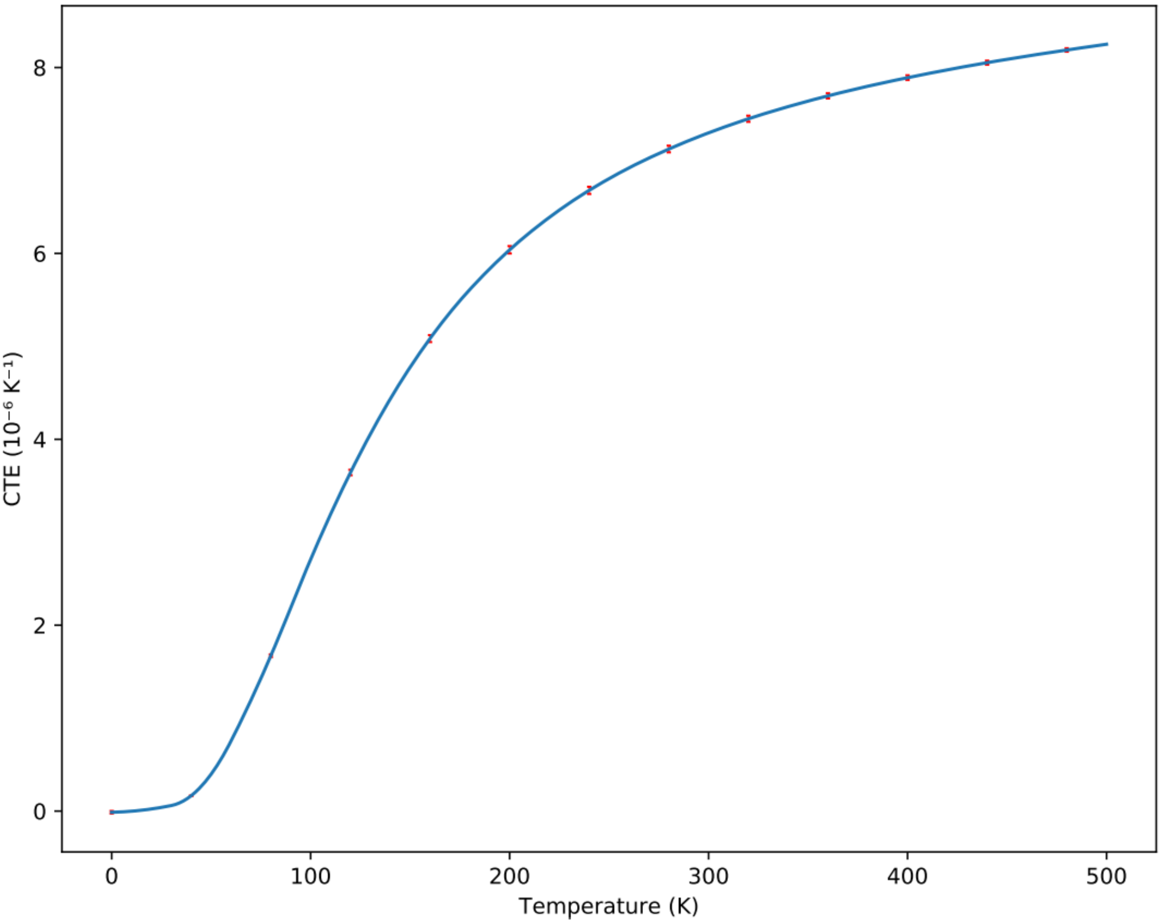

Figure 44: Coefficient of thermal expansion for $TiFe_2Si$ *with error bars in the temperature range from 0 K to 500 K.*

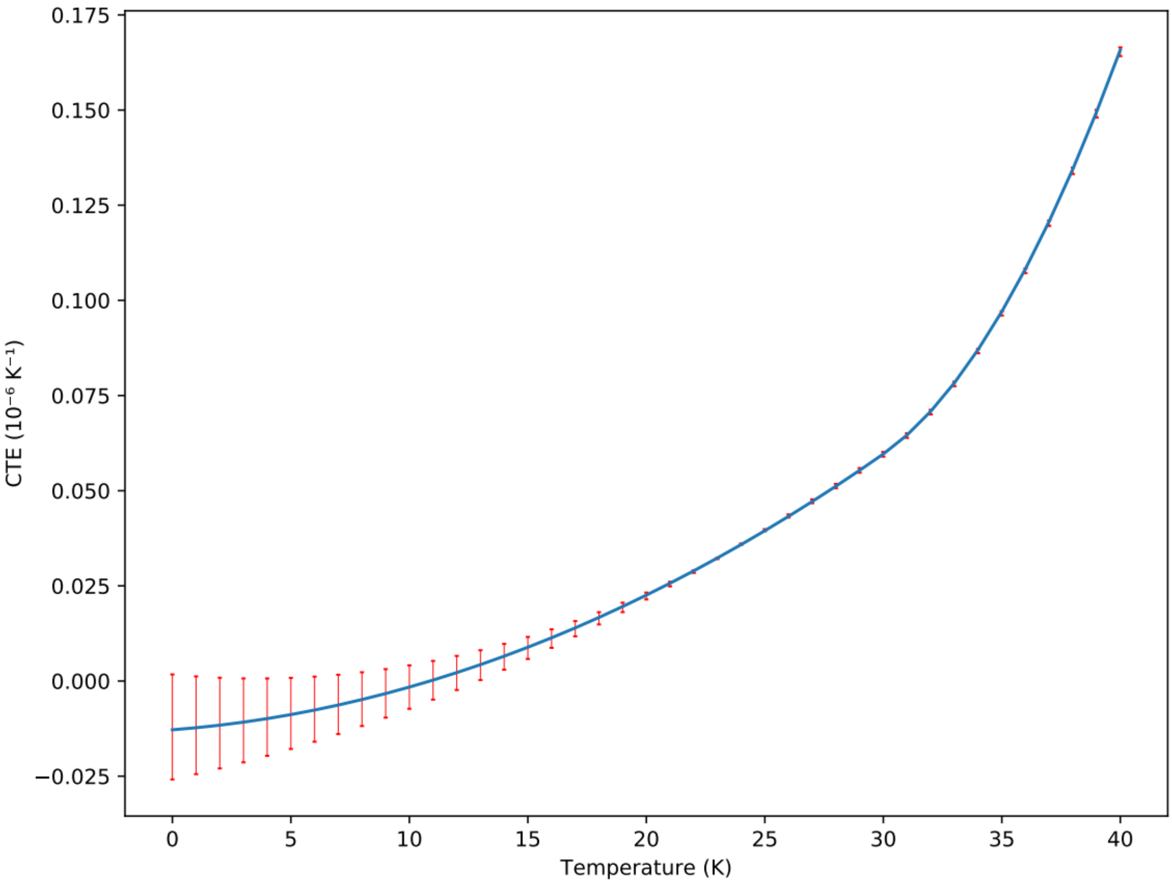

Figure 45: Coefficient of thermal expansion for $TiFe_2Si$ with error bars in the temperature range from 0 K to 40 K.

Five other materials with similar structures and containing both iron and silicon have been studied through ab initio calculations using DFT recently by Noui et al[71]. They used the linearized augmented plane wave (LAPW) method that is in Wien2k[72], local spin density approximation (LSDA)[73] and the quasi-harmonic Debye model[74, 75] to calculate the CTE. The materials are $Fe_2Mn_xNi_{1-x}Si$ where x = [0,0.25,0.5,0.75,1]. In addition, Noui et al. investigated the same compositions in a very similar structure as they explain in their article. The structure investigated in this thesis have the iron atoms at sites with similar chemical surroundings. However, there is also the possibility for having the iron atoms at sites with different chemical surroundings. That is, the atoms are ordered such that the space group will be $F\bar{4}3m$, where the iron atoms occupy the 4a and 4c Wyckoff positions. That space group has the symmetry to be piezoelectric. Figure 46 shows the CTE from this study in the same plot as the CTE of the Noui et al.'s material with the same structure. This CTE is with respect to volume, not lattice constant as the other CTE's have been. This CTE is just three times the CTE with respect to lattice constant for a cubic cell. From Figure 46 it is seen that the behaviour of the curves is very similar. Since Noui et al.'s study only includes every 100 temperature it is hard to compare the CTE below 200 K which is the area where the CTEs is least linear. Still it is seen that the characteristics from the CTE of $TiFe_2Si$ are present in the CTE of $Fe_2Mn_xNi_{1-x}Si$ with the quick increase from 0 K to around 200 K and then a slowly linear increase for higher temperatures. It is also seen that the CTE of these materials seems to be of equal size to the CTE of $TiFe_2Si$ below 200 K, but above this temperature the CTE of $Fe_2Mn_xNi_{1-x}Si$ is higher. Figure 47 shows the CTE from this study in the same plot as the CTE of the Noui et al.'s material with the iron atoms at sites with different chemical surroundings. The discussion for Figure 46 holds for the CTEs in Figure 47 too. The material that seems to have the overall closest CTE to the CTE of this material is the structure which have the iron atoms at the same positions and with x = 0.75. The uncertainties in Noui et al.'s studies are not stated. The Bulk modulus of this material is 2477.8 kbar and the Debye temperature is 647.85 K at 0 K for both properties. This is not so far from the Bulk modulus of this material which is at 2537.24 kbar from this study. The Debye temperature is more different as it is 494.03 from this study. There are some differences in Noui et al.'s study and this thesis. Noui et. Al uses the LAPW method and the LDSA to calculate the ground state properties of the materials, while this study uses the PAW method and PBEsol GGA to calculate properties of $TiFe_2Si$ in the ground state and at 300 K. When finding the volume as a function of temperature, the benchmarked method uses the phonon density of states or phonon frequencies at 0 K to calculate the free energy, while this method uses the phonon frequencies at 300 K. The benchmarked method used the Debye-Slater model to calculate the free energy as a function of temperature on a volume grid and found the minimum volume from this, while this study used to quasi harmonic approximation which is stated to be more accurate[75]. Also, the CTE is found by the analytical expression for CTE, while it is found by direct differentiation in this study. Since Noui et al. uses different methods than in this thesis it cannot be concluded if the higher CTE of their materials is due to the materials they use or due to the method.

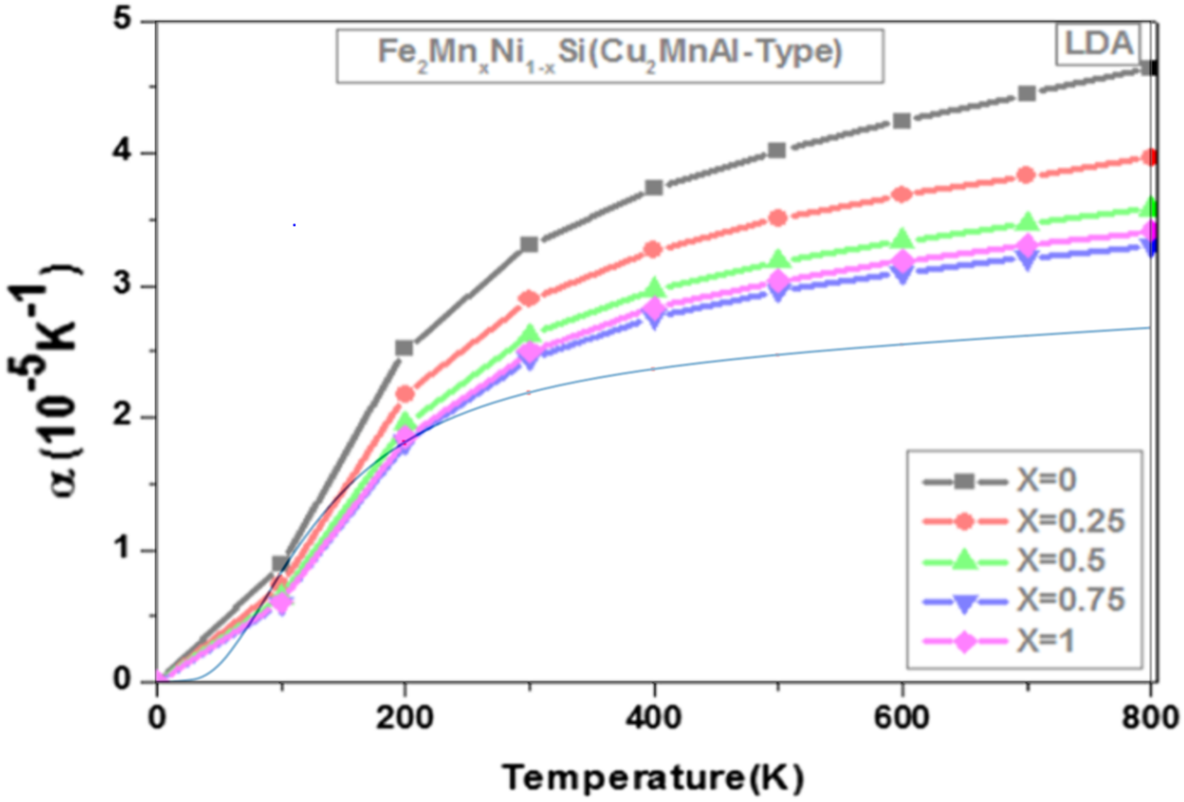

Figure 46: CTE with respect to volume for $Fe_2Mn_xNi_{1-x}Si$ from Noui et al.'s study[71] and the CTE of $TiFe_2Si$ from this study as the solid light blue line with red error bars. This plot is when the atoms are ordered in the same way as for $TiFe_2Si$ in this study.

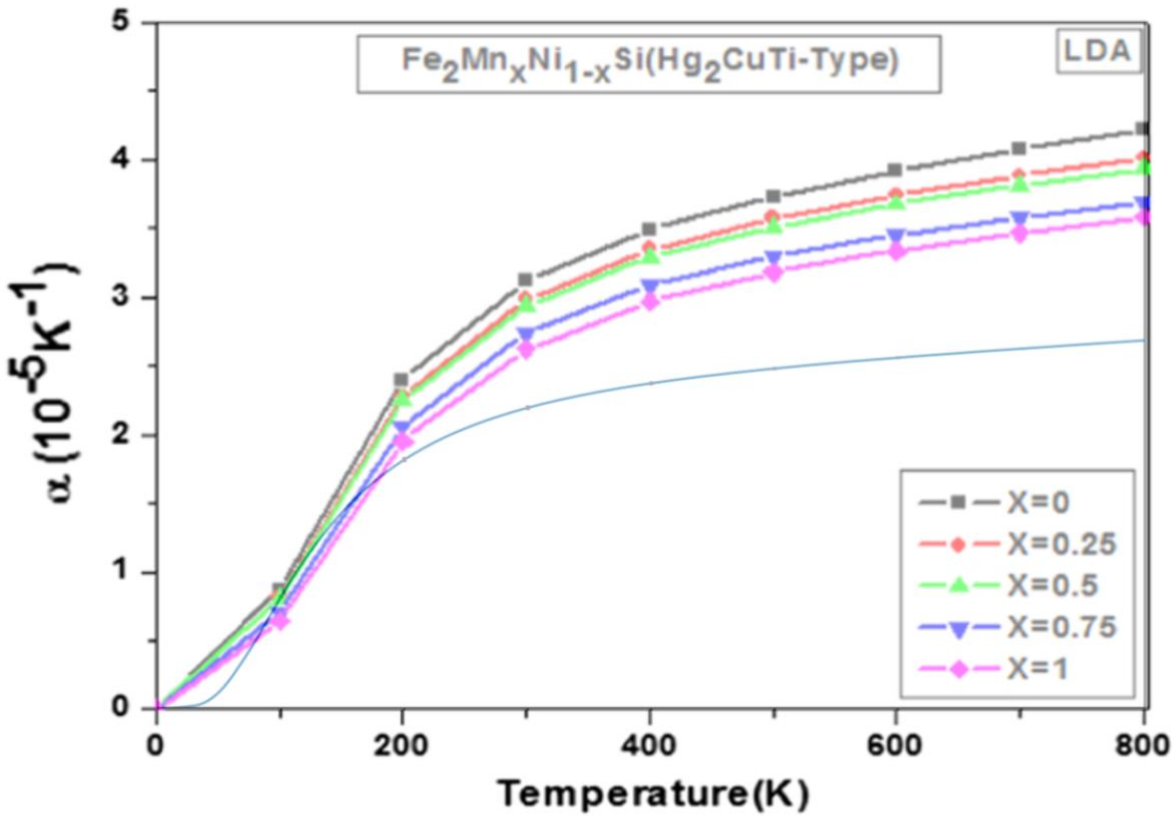

Figure 47: CTE with respect to volume for $Fe_2Mn_xNi_{1-x}Si$ from Noui et al.'s study[71] and the CTE of $TiFe_2Si$ from this study as the solid light blue line with red error bars. This plot is for the structure with the iron atoms at sites with different chemical surroundings.

Another study of a Heusler structure with some of the same atoms as $TiFe_2Si$ is a study from Yan et al.[76] This study was experimental and the material was $TiFe_2Al$ which was investigated by neutron diffraction over a range of temperatures. $TiFe_2Al$ also had an amount of Laves phase. The Heusler phase dominated in the temperature range from 300 K to 1300 K, while the Laves phase dominated above 1350 K. The CTE of this material is only calculated from 300 K 1100 K, where the amount of Heusler phase is close to 100 %. Further, the iron atoms occupied the sites that gives the space group $Fm\overline{3}m$ which is the same as for the $TiFe_2Si$ structure studied here. Most of the Ti atoms were placed at the 4a site, but some on the 4b site. In the $TiFe_2Si$ structure in this study, the Ti atoms are at the 4a site. The CTE of $TiFe_2Al$ is from Yan et al.'s study is derived from a linear fit of the lattice parameter as a function of temperature and is therefore constant at $1.4552*10^{-5}$ K^{-1} and plotted with the CTE of this study in Figure 48. The CTE of $TiFe_2Si$ does not reach this value until around 2600 K and is not constant in the temperature range considered. The uncertainty is not stated.

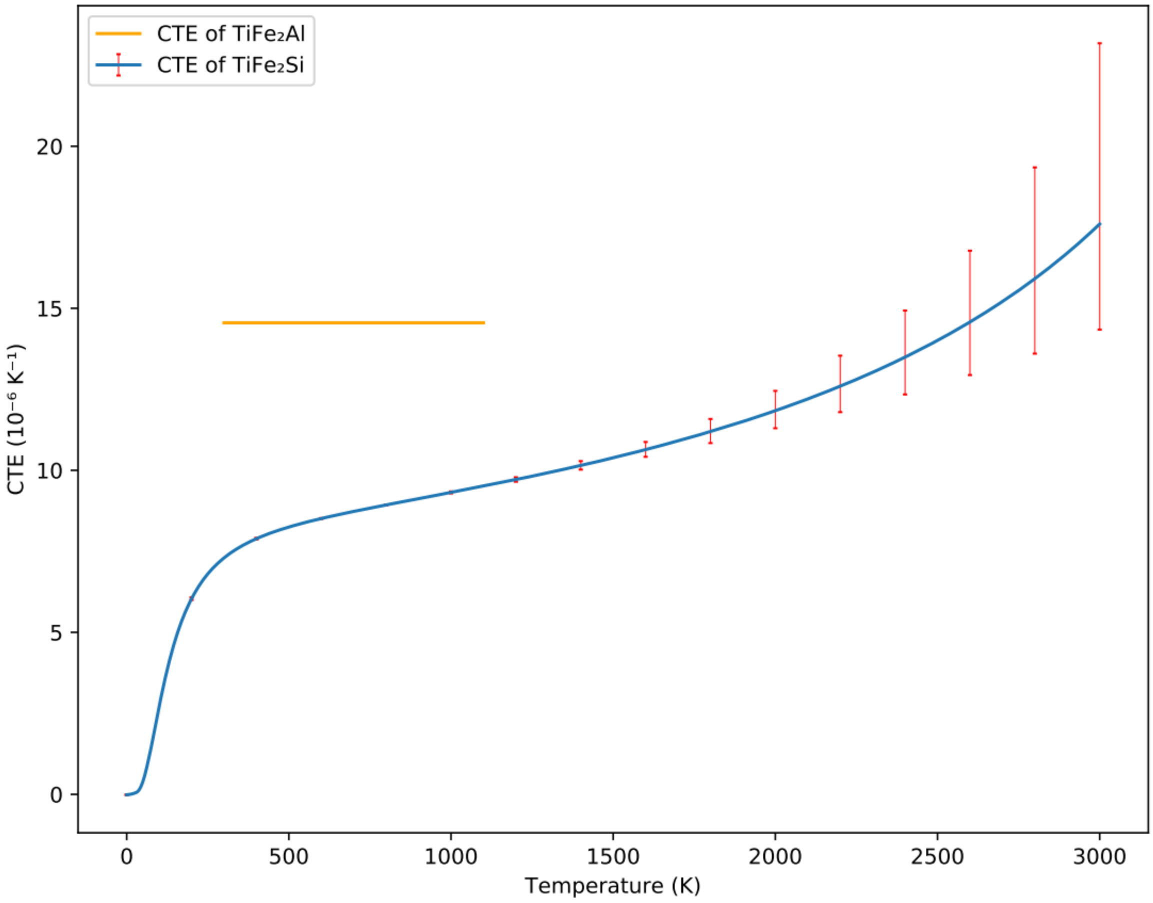

Figure 48: The CTE of $TiFe_2Si$ and the CTE of $TiFe_2Al$ from Yan et al.'s[76] study.

A third study of a material with a similar structure as $TiFe_2Si$ is a study of Fe_2CrX where X = [Al, Ga][77]. In this study by Paudel and Zhu, the Cambridge Serial Total Energy Package[78] (CASTEP) was used to perform DFT like calculations. The exchange-correlation potential used was the Perdew-Wang[23], the Perdew-Burke-Ernzerhof[69] (PBE) and the local density approximation, but PBE was used for all calculations of physical properties as it gave the best result. The ultra-soft pseudo-potential and plane wave basis sets[68] were used in the calculations and the ground state was found by using Broyden-Fletcher-Goldfarb-Shanno[79] optimization method. The thermodynamic characteristics were calculated using the quasi-harmonic Debye model by the GIBBS program[80, 81]. The iron atoms in these structures were also ordered in the same way as $TiFe_2Si$ in this study.

The phonon dispersion relations of these materials will be compared to see if it can help to explain the CTEs. Figure 49 compares the phonon dispersion relations of Fe_2CrAl and $TiFe_2Si$. From that it is seen that the wavevectors in Fe_2CrAl have frequencies between 4 THz and 8 THz on the wavevectors between W and L, X and W, and W and K. These wavevectors in $TiFe_2Si$ have frequencies from round 6 THz to a little below 14 THz. Further the wavevectors in Fe_2CrAl do not have frequencies between 8 THz and 11 THz, but some around 12 THz. This is not the case for $TiFe_2Si$ where the wavevectors have frequencies all the way from 0 THz to a little below 14 THz. Altogether, the wavevectors of $TiFe_2Si$ have higher frequencies than those of Fe_2CrAl. Except the difference in value, the structure of the two dispersions is rather equal. The curves going from gamma increasing on both sides, then stabilizing around a certain value. Also, the densely packed curves to the right of the X point.

The phonon dispersion relations of Fe_2CrGa and $TiFe_2Si$ are compared in Figure 50. The comparison shows that the frequencies for the wavevectors between W and L, X and W, and W and K are between 3 THz and 9 THz ca. for Fe_2CrGa. There is no gap of frequencies for this material phonon dispersion relations as the three highest curves only go up to around 9 THz. The sum of the frequencies of the wavevectors in Fe_2CrGa seems to be less than those of Fe_2CrAl which again is less than those of $TiFe_2Si$. Here also the shape of the curves of the two materials has similarities, like the raising curves from the gamma point that stabilizes at a certain value. All three materials have three acoustical and 9 optical curves, which is expected as there are 4 atoms in the primitive cells for all the materials. The acoustic branches are those that are 0 at the gamma point.

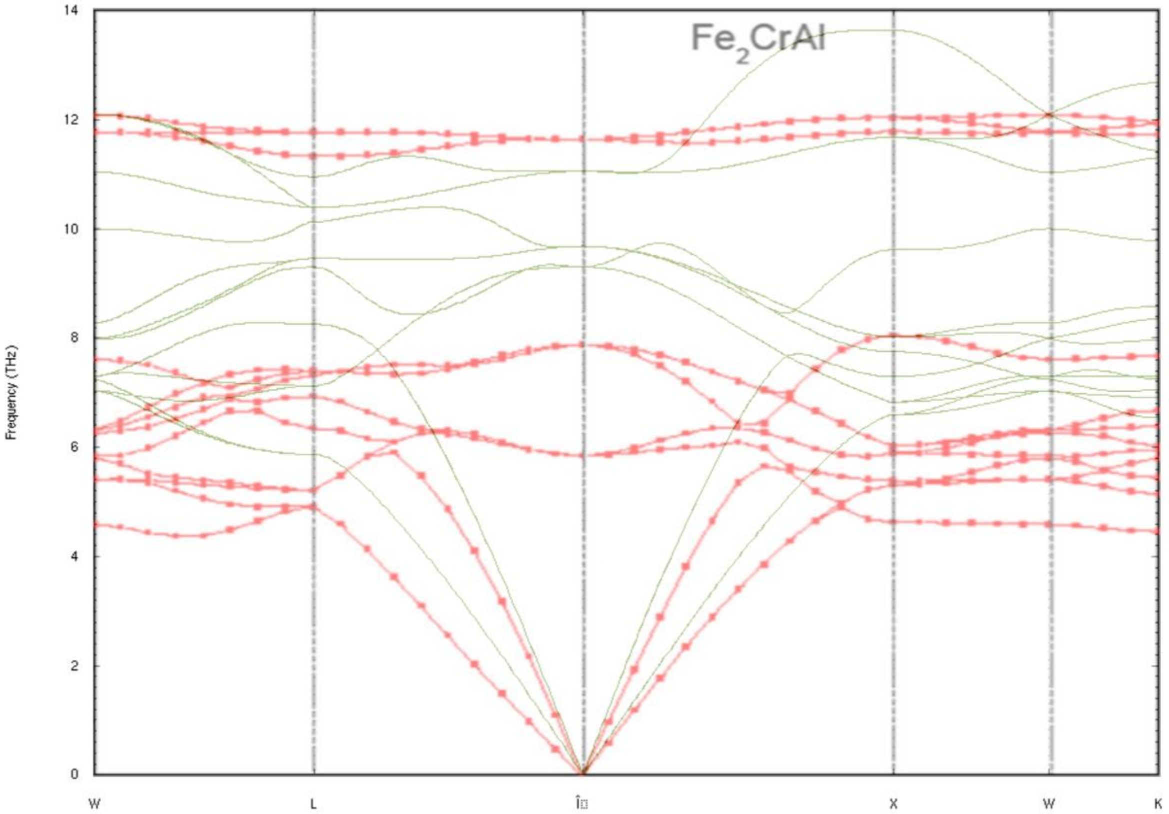

Figure 49: Phonon dispersion relations of Fe_2CrAl from Paudel and Zhu's[77] study as the red lines and the phonon dispersion relations of $TiFe_2Si$ from this study as the green lines. The phonon dispersion relations of this study results from 3 configurations that were made based on calculated force constants from the 20 configurations that were made based on the Debye temperature and the unit cell in its original size.

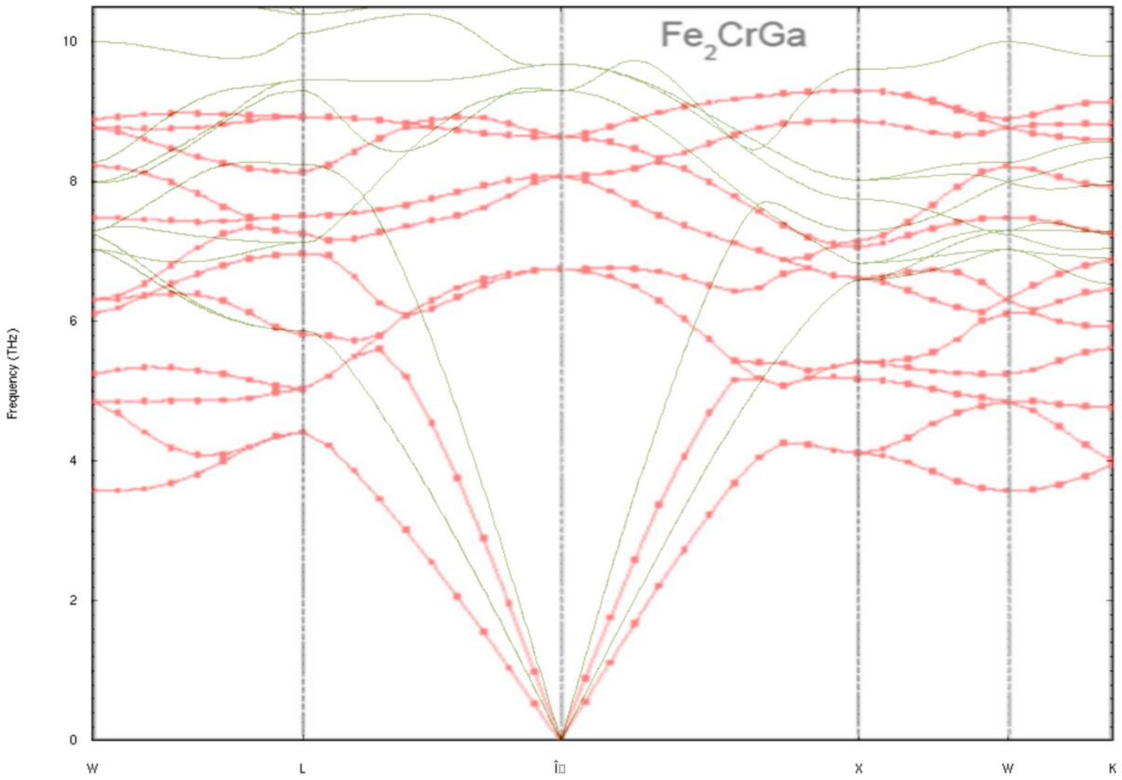

Figure 50: Phonon dispersion relations of Fe_2CrGa *from Paudel and Zhu's*[77] *study as the red lines and the phonon dispersion relations of* $TiFe_2Si$ *from this study as the green lines. The three highest curves from this study are not in the plot as they only go up to 10.5 THz.*

The CTE of Fe_2CrAl and the CTE of $TiFe_2Si$ are compared in Figure 51. It will be the curve calculated at 0 GPa that will be the most comparable to the CTE of $TiFe_2Si$ in this study, as the pressure over its relaxed structure is around 0. Again, the shape of the CTEs of the two materials is very equal with the fast increase from 0 K to around 200 K, then a more and more linear increase. For this material as for $Fe_2Mn_xNi_{1-x}Si$, the behaviour is hard to compare below 100 K as the CTE of $TiFe_2Si$ is least linear here. This behaviour holds for all pressures. The CTE of Fe_2CrAl is a lot higher than the CTE of $TiFe_2Si$ right from the start which stands out from the behaviour of the CTEs of $Fe_2Mn_xNi_{1-x}Si$, which were of equal size with the CTE of $TiFe_2Si$ at 100 K.

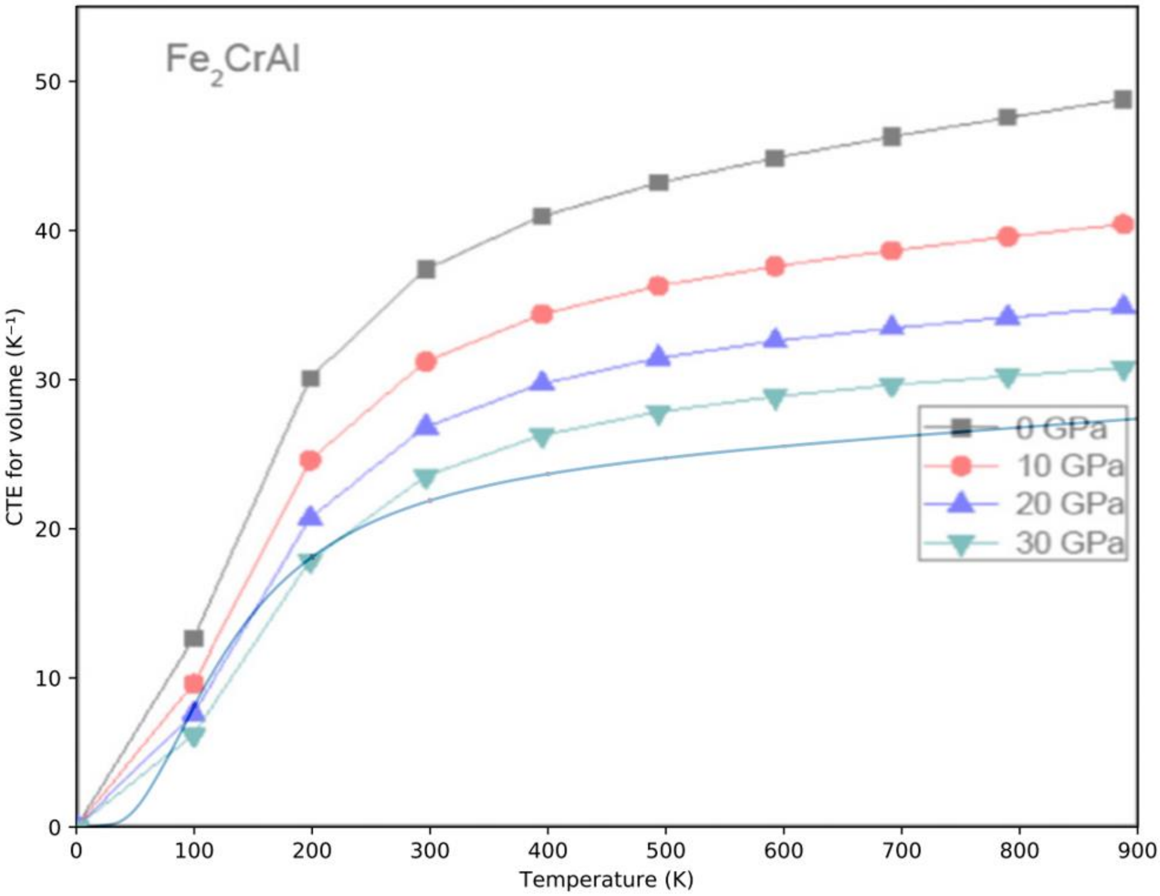

Figure 51: CTE with respect to volume for Fe_2CrAl from Paudel and Zhu's[77] study at different pressures shown by the labels, and the CTE with respect to volume for $TiFe_2Si$ as the blue line with red error bars.

The CTEs of $TiFe_2Si$ and Fe_2CrGa compared in Figure 52, show the same behaviour as the CTEs in Figure 51. One interesting observation in this plot is that the CTE at 30 GPa is very close to the CTE $TiFe_2Si$ at all temperatures. The CTE at 0 pressure is higher for Fe_2CrGa than for $TiFe_2Si$, but not as high as for Fe_2CrAl. The uncertainty in the CTE from this study is not stated. There has not been found any clear coherence between dispersion relations and CTE just from studying these three materials. Maybe it could be found by studying more materials, and maybe consider more properties as well. Also, the methods used are different, which makes the results less comparable. Different GGAs and optimization methods were used. The free energy is found using the quasi harmonic Debye model which is equivalent to the Debye-Slater model mentioned earlier, which is less accurate than the quasi harmonic approximation used in this study. Else the method for finding the optimized volume is rather equal. Also, the CTE is found by the analytical formula $\alpha = \frac{\gamma C_v}{B_T V}$ in the benchmarked paper, while it is found by direct differentiation in this study. In the analytical formula from the benchmarked paper, γ is the Grüneisen parameter, C_v the heat capacity, B_T the isothermal bulk modulus and V the volume. All these are functions of temperature.

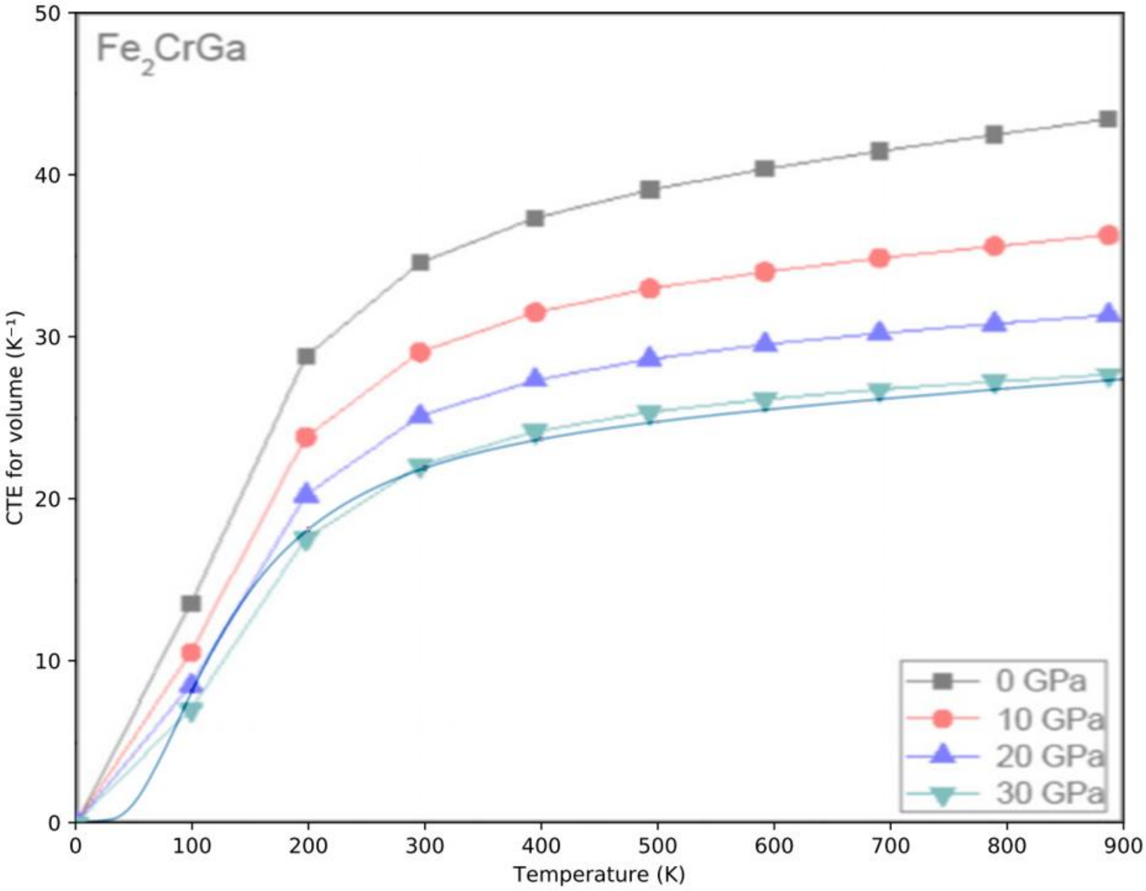

Figure 52: CTE with respect to volume for Fe_2CrGa *from Paudel and Zhu's*[77] *study at different pressures shown by the labels, and the CTE with respect to volume for* $TiFe_2Si$ *as the blue line with red error bars.*

The bulk moduli of Fe_2CrAl is 2149.9 kbar, the shear moduli 1338.7 kbar and the Debye temperature is 571.18 K at 0 K and 0 GPa. The bulk moduli of Fe_2CrGa is 2137.7 kbar, the shear moduli 1173.2 kbar and the Debye temperature is 517.75 K at 0 K and 0 GPa. This is lower than the bulk and shear moduli of $TiFe_2Si$ but higher than its Debye temperature.

5.4. Discussion of Gibbs free energy of $TiFe_2Si$

From Figure 20 it is seen that the Helmholtz free energy of $TiFe_2Si$ becomes more negative as the temperature increases. It can however not be concluded that this structure will be more stable with rising temperature, even though the lowering of the energy is favourable, since another phase can have even lower energies. The Gibbs free energy vs temperature and pressure is shown in Figure 22. As the pressure increases, the Gibbs free energy increases with temperature first, then decreases, like a second order polynomial with a vertex. At the highest pressures the temperature decreases at the lowest temperatures, before it increases to a vertex and decreases again.

5.5. Discussion of $GaNaTe_2$

The calculated curves of the CTEs of β-$GaNaTe_2$ shown in Figure 23 and Figure 24 do not follow exactly the same trend as the CTEs of diamond and $TiFe_2Si$. While the CTEs of diamond and $TiFe_2Si$ started rather flat, the CTEs of β-$GaNaTe_2$ increase fast immediately, especially for the one along the a-lattice parameter. The CTE along the c-lattice parameter has a touch of the behaviour of diamond and $TiFe_2Si$ as it increases faster and faster below around 50 K. However, this acceleration of the increase is not as clear as for the two earlier discussed materials which increase slower in the start. Then after a certain temperature the CTE along the a-lattice parameter increases slower like for diamond and $TiFe_2Si$. The CTE along the c-lattice parameter does not reach a temperature where it starts to slowly increase, it rather flattens out and decreases after 400 K. The large uncertainty around 600 K for the CTE along the c-lattice parameter may origin from the expansion starting to exceed the range of expanded unit cells. The CTE along the a-lattice parameter is clearly negative with uncertainty considered for the very lowest temperatures. The CTE along the c-lattice parameter is negative at 1 K and below. The uncertainty in CTE increases with temperature for the a-lattice parameter. The uncertainty in the CTE of the c-parameter increases while the CTE increases, then it decreases as the CTE drops after around 350 K and gets surprisingly small around 550 K. It does however get very big in the downward direction at the last point. It is the a-lattice parameter that expands fastest, except from at the lowest temperatures where it is negative. There has been no found calculations of the CTE of this phase of $GaNaTe_2$ to compare with. This material has the biggest expansion of the materials considered so far.

Sadly, the other phase of this material was found to not be stable within these calculations. However, it is important to state that this cannot be concluded to be true in reality. If the other phase of the material was found to be stable and the free energies could be calculated, everything calculated for the β-structure would be calculated for the α-structure too. Then if Gibbs free energy could be compared as a function of temperature and pressure, a phase change may have been found. The Gibbs free energy would have decided what phase is stable at the given temperature and pressure and from this a phase diagram of temperature and pressure could have been constructed. If a phase change was found in the temperature and pressure grid investigated, this material would theoretically be able to generate elctricity as described in the introduction since it would have all the properties searched for in this study. That is, a material that changes phase in the temperature and pressure grid investigated, has bandgap in both phases, and a change in pyroelectric coefficient during phase change.

5.6. Discussion of Gibbs free energy of $GaNaTe_2$

From Figure 27 it is seen that the Gibbs free energy at 0 pressure becomes more negative for the β-structure with increasing temperature, which is energetically favourable. From Figure 29 it is seen that the Gibbs free energy increases with increasing pressure. The temperature dependence as the pressure increases is so that the Gibbs free energy decreases slowly at low temperatures, and then decreases more dramatically after a certain temperature.

5.7. Discussion of $GaCuSe_2$

The CTE of the a-lattice parameter of $GaCuSe_2$ starts being negative, then quickly increasing linearly to a little above 10^{-5} K^{-1} around 150 K. Then it increases more slowly to about 1250 K where it reaches ca. $15*10^{-6}$ K^{-1} before it slowly starts to increase faster again and reaches ca. $25*10^{-6}$ K^{-1} at 2000 K. The behaviour is similar to that of the CTE of $TiFe_2Si$ except at the very lowest temperatures. It should be noted that it is at the lowest temperatures the shape of the CTE is most affected by the intervals of the spline interpolation. It is also very similar to the CTE of the a-lattice parameter of β-$GaNaTe_2$ in the temperature range it is plotted for, which is very clear from Figure 53. The CTE of the a-lattice parameter of $GaCuSe_2$ is larger than the CTE of diamond and $TiFe_2Si$, but lower than the CTE of the a-lattice parameter of β-$GaNaTe_2$. Except at the lowest temperatures, it is clearly higher than the CTE of the c-lattice parameter of the same material. The uncertainty of the CTE of the a-lattice parameter gets bigger as the temperature and CTE gets bigger. It is below 3 % up to ca. 1300 K and always below 5 % up to 2000 K. It is much bigger at the lowest temperatures, but here relative uncertainty measures bad as the values are very small. The CTE of the c-lattice parameter of $GaCuSe_2$ is unlike any of the other CTEs calculated before. It starts around 0 K^{-1} at 0 K, then decreases fast to ca $-2*10^{-6}$ K^{-1} around 100 K before it increases fast to ca $2*10^{-6}$ K^{-1} around 200 K. From there, it increases more slowly but still fast to ca. $13*10^{-6}$ K^{-1} at ca. 1500 K before it decreases a little bit faster to around 7*10^{-6} K^{-1} at 2000 K. It is lower at all compared temperatures than the CTE of the c-lattice parameter of $GaNaTe_2$ and different in shape as shown in Figure 54. It is bigger than the CTE of diamond after ca. 150 K and above. It gets bigger than the CTE of $TiFe_2Si$ at ca. 1000 K and then gets smaller again at around 1800 K. The uncertainty of the CTE of the c-lattice parameter doesn't follow a particular trend, it varies with temperature. For the error bars shown in Figure 31 the largest is at 1200 K. The uncertainty of the c-lattice parameter is below 5 % at most temperatures. The uncertainty came up to a little below 10 % around 1900 K.

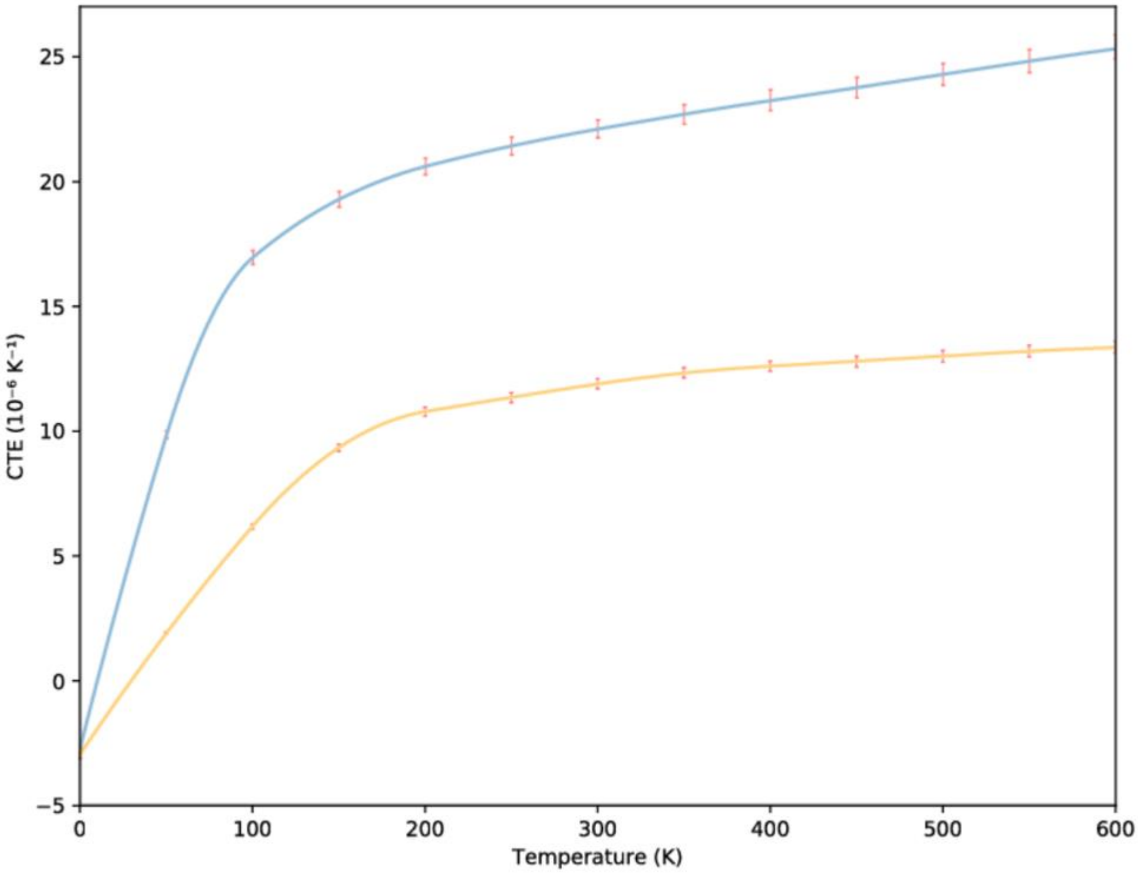

Figure 53: CTE of the a-lattice parameter of $GaNaTe_2$ as the blue line and the CTE of the a-lattice parameter of $GaCuSe_2$ as the orange line. It clearly shows that the CTE of $GaNaTe_2$ is higher at all temperatures compared, but that the behaviour is very similar.

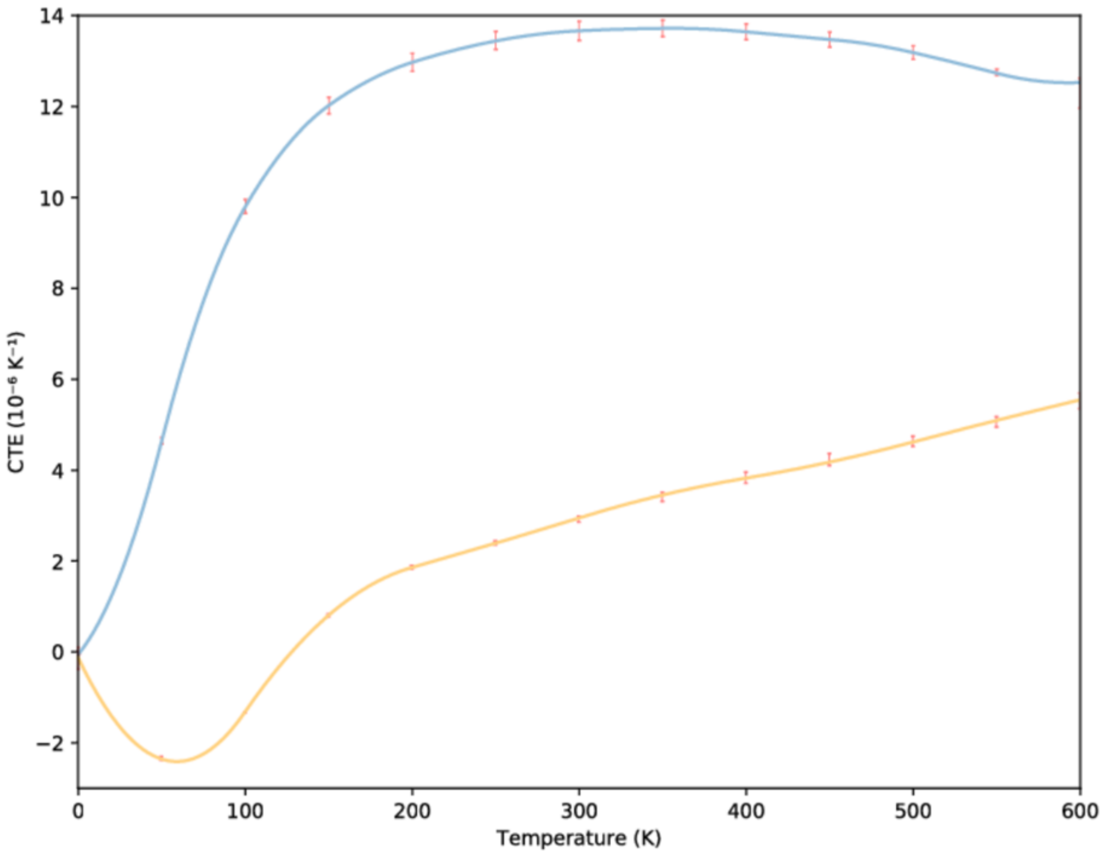

Figure 54: CTE of the c-lattice parameter of $GaNaTe_2$ as the blue line and the CTE of the c-lattice parameter of $GaCuSe_2$ as the orange line. It clearly shows that the CTE of the c-lattice parameter of $GaNaTe_2$ also is higher than that of $GaCuSe_2$ at all temperatures compared.

5.8. Discussion of Gibbs free energy of $GaCuSe_2$

The Gibbs free energy at zero pressure as a function of temperature is shown in Figure 34. It shows, just as for the other materials, that the energy decreases with temperature. The uncertainty increases with temperature. The Gibbs free energy as a function of temperature and pressure is shown in Figure 36. It shows that as the pressure increases, the Gibbs free energy gets higher and increases faster with temperature.

5.9. Discussion of secondary pyroelectricity of $GaCuSe_2$

The pyroelectric components are given by the αββ components of the piezoelectric tensor (shown in Table 7) where α, β = (x,y,z) as it is only the diagonal terms of the CTEs that are nonzero. The x-component of the second term of the pyroelectric vector is equal to the y-component for $GaCuSe_2$. It behaves like a negative CTE of diamond or $TiFe_2Si$ except around 0 K. That is, it starts a little above 0 C/m^2K, then rapidly decreases as the temperature increases until around $4*10^{-9}$ C/m^2K at ca. 200 K. Then the curve decreases more slowly, but as the temperature increases the curve decreases faster and faster until it reaches a little under -10^{-8} C/m^2K at 2000 K. The behaviour of the x- and y-component is not a surprise, as these components turns out to be $-37*10^{-5}$ times the CTE of the a-lattice parameter. The z-component follows the same pattern, but in the opposite direction. It starts at around $-7*10^{-9}$ C/m^2K, then increases fast as the temperature increases until around $25*10^{-9}$ C/m^2K at ca. 200 K. Then the curve increases more slowly, but as the temperature increases, it increases faster and faster until it reaches around $57*10^{-9}$ C/m^2K at 2000 K. The behaviour of the z-component is easy to predict too, as it is almost just a positive number times the CTE of the a-lattice parameter. The influence of the CTE of the c-lattice parameter is well below 1 %. The uncertainty seems to increase as the absolute value of the pyroelectricity increases, even though the error bar is larger at 1800 K than at 2000 K. The uncertainty seems to be very much the same in the negative and the positive direction. In this study the temperature dependence of the pyroelectric vector comes alone from the temperature dependence of the CTEs, while the piezoelectric tensor is calculated at 0 K and is constant at all temperatures.

5.10. Lattice parameter as a function of temperature

Figure 39 shows the lattice parameter of diamond as a function of temperature from multiple experimental studies. It is clear from this plot that the lattice parameter from this work is too high and outside the uncertainty range of the experimental data. In comparison, the lattice parameter from this study at 25 degrees Celsius is 3.584842 Å, while the experimental lattice data from the high accuracy data of Stoupin and Shvyd'ko is around 3.5671 at this temperature. This disagreeing will be rather constant or even increase as the CTEs of the experimental data and from this calculation are quite equal with this calculation's CTE being a little above most of the experimental points. This is expected as it is normal that the lattice parameter calculated with VASP is not quite correct[82]. It is only the CTE that is hypothesised to be very correct. The uncertainty gets generally bigger as the lattice constant gets bigger, just as for the CTE of diamond.

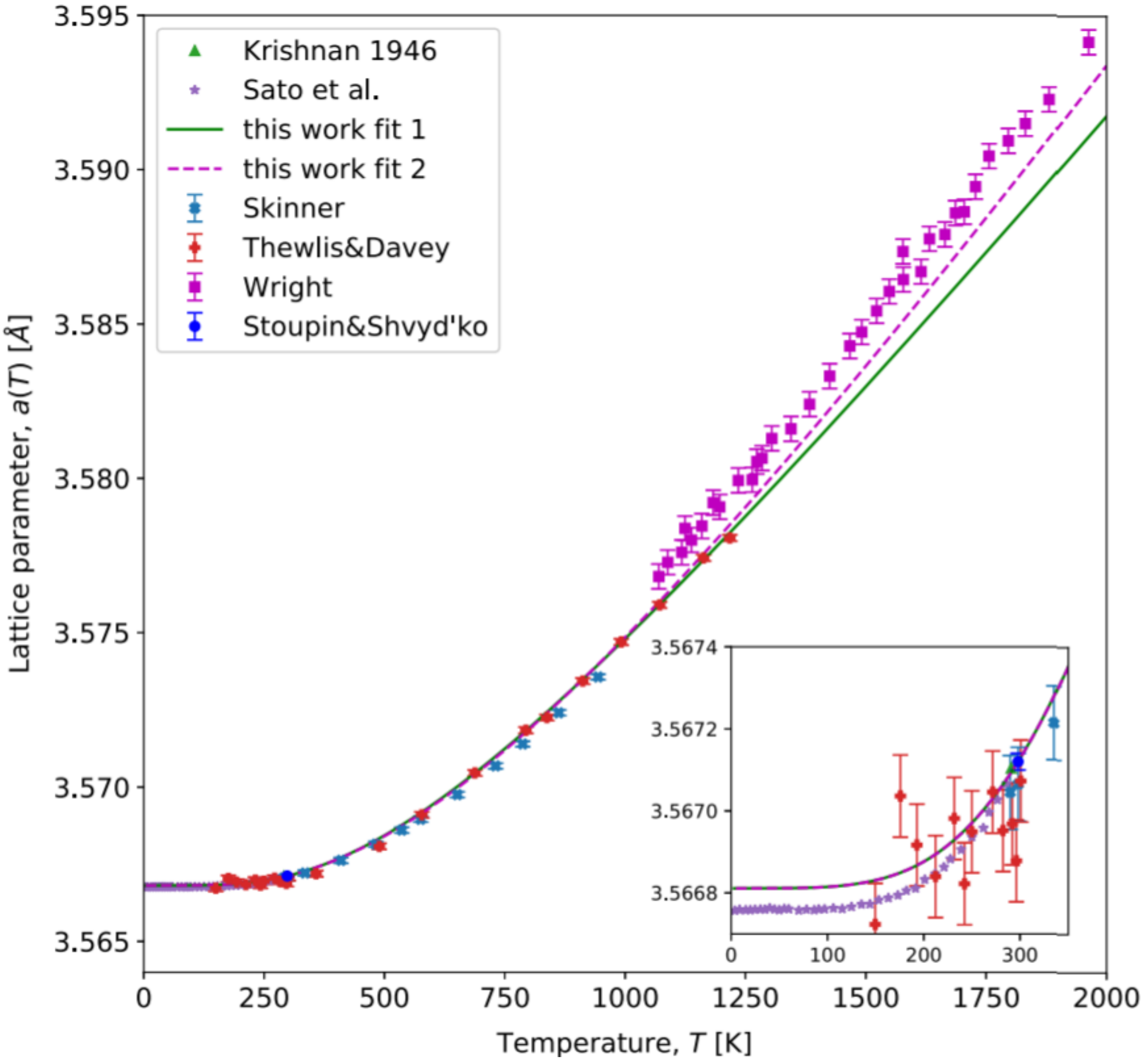

Figure 55: The lattice parameter of diamond as a function of temperature from the Jacobsen and Stoupin collection of experimental data[58].

The lattice parameter of $TiFe_2Si$ has very much the same form as the CTE of diamond, except that the lattice parameter of $TiFe_2Si$ increases faster. This is nothing new as the shape of the lattice parameter vs temperature is decided by their CTEs. It is only the starting point that gives new information. The uncertainty increases as the lattice parameter increases, as for the CTE of this material. The lattice parameter of $TiFe_2Si$ has been found experimentally to be 5.709 Å at ca. 300 K[28]. The lattice constant from this study at the same temperature is 5.650 Å. From Figure 56 one sees that the lattice constant from this study does not reach the experimental value until around 1500 K. The phase has been reported to only form at or below 800 K[83].

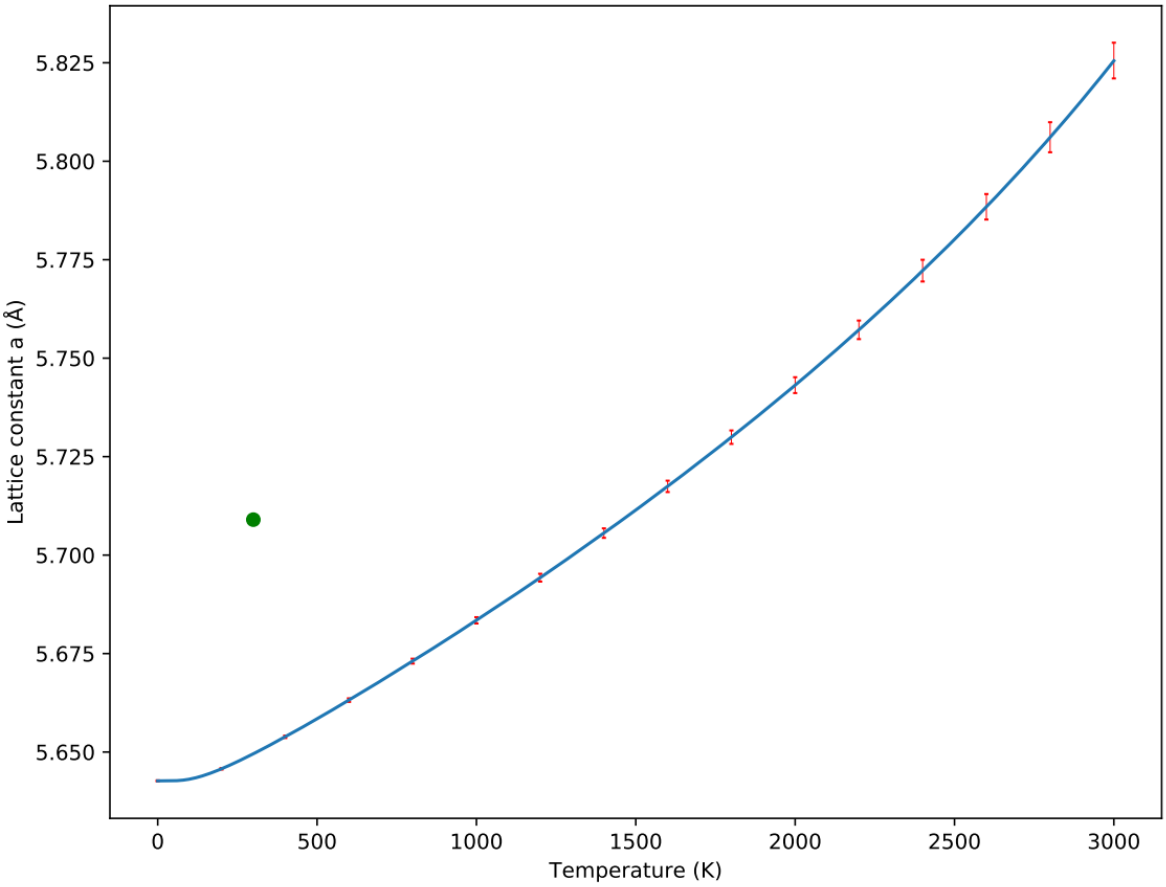

Figure 56: Lattice parameter vs temperature for $TiFe_2Si$ with the experimental value[28]. The experimental value is higher and outside the uncertainty range, which again confirms the disagreement between experimental lattice parameters and DFT lattice parameters.

The a-lattice parameter is higher than the c-lattice parameter of β-$GaNaTe_2$ at 0 K, and expands relatively faster as discussed from the CTEs. At 0 K the a-lattice parameter is at 8.113 Å while the c-lattice parameter is at 6.765 Å. At 600 K the a-lattice parameter is at 8.212 Å and the c-lattice parameter is at 6.812 Å. For $GaCuSe_2$ the c-lattice parameter is highest at 0 K, and expands just most up to 2000 K, but the relative expansion is smaller as shown from the CTEs. The a-lattice parameter at 0 K is 5.602 Å while the c-lattice parameter is 11.063 Å. At 2000 K, the a-lattice parameter is 5.773 Å while the c-lattice parameter is 11.241 Å.

5.11. Discussion of the heat capacity

The specific heat capacity at constant volume of diamond has a very similar shape as the CTE of diamond. It starts around 0 and stays almost constant to around 150 K before it starts to quickly increase until it increases slower and slower from around 500 K. It seems to converge to just above 500 J/K kg as the temperature increases. The shape of the heat capacity of $TiFe_2Si$ is similar, but the increase starts much faster, around 50 K. The increase is also steeper, so that it is almost finished around 500 K. It seems to converge toward a little above 2000 J/K kg. The shape of the heat capacity of β-$GaNaTe_2$ is also similar to the two others. The increase starts early, around 20 K and is almost finished around 200 K. It converges toward a little above 500 K. It is the same for $GaCuSe_2$. The increase starts early around 20 K and is almost finished at 250 K. The converging value is a little above 500 K.

5.12. Drawbacks of the method

Although the method used works very well, there are some fundamental drawbacks of it. First, the materials that are being investigated are perfect crystals, because the cell that is used in each calculation is repeated periodic to generate the material. A perfect crystal does not exist in nature, it does not even form theoretically, simply because the entropy term in the Gibbs free energy makes the material more stable if there exist vacancies in the material. Also, the eigenfrequencies are calculated at a certain temperature, 300 K for the stable materials. Therefore, we do not know for what temperatures the materials exist at, except diamond which was mentioned to destabilize at 1800 K. That is why the α-phase of $GaNaTe_2$ was calculated for at 100 K and 1000 K. We do not know at what pressures the materials exist at either. The exchange-correlation functionals used when doing calculations with VASP are not the correct exchange-correlation functionals. It is just an approximation. The fact that the correct exchange-correlation functional is not known is a limitation for all DFT calculations. Another limit is the numerical accuracy.

5.13. Central processing unit time

The calculations performed in this thesis have in total used a lot of CPU time. Some of the calculations are cheap while some are very expensive. The CPUs used by the calculations will be discussed in this section. Since calculations are done on both the supercomputer Abel, which is shut down now, and Saga, a time factor is calculated so that it is possible to compare calculation time on the two computers. This is calculated by dividing the total CPU time used for the total energy calculation on the first supercell configuration of diamond in its relaxed structure at 0 K made from force constants based on the Debye temperature performed on Saga, by the total CPU time used for the same calculation on Abel. This time factor is calculated to be 0.61494. The tables in Appendix C shows the CPU time used for the different materials. It is clear from these that it is the supercell calculations that take up the time while they also have to be done for different configurations. The CPU time on the small original cells are negligible compared to the CPU time of the supercells. It is the calculations of the supercells of $TiFe_2Si$ which are clearly most expensive. However, the expensive calculation of the supercell of $TiFe_2Si$ was done with 8 tasks and 10 CPU's per task and four tasks per node. The cheap calculation and many of the other supercell calculations for other materials were done with 64 tasks and 2 nodes. Therefore, it seems like the second setup is the most effective one, at least for these calculations. For almost all other supercell calculations, 64 tasks on two nodes or 36 tasks on 1 node were used, as both setups seemed to be effective. Also, the relaxations of the supercells were expensive calculations, most expensive after the total energy calculations of $TiFe_2Si$.

5.14. Summary of discussion

The CTEs, the Gibbs free energy, the lattice parameters and the heat capacity of the different materials have been discussed. The secondary pyroelectricity of $GaCuSe_2$ and the CPU time of the different calculations have been discussed.

6. Conclusion

6.1. Conclusion of diamond

Diamond is the only material that has experimental values to compare the CTE with. The calculated CTE of diamond in this study is tremendous close to the experimental points. It is also the only material with other theoretical CTEs to compare with. It is very similar with these too. Diamond was only a test material and was not expected to or had the symmetry to have a non-zero pyroelectric vector. It does however show that the method used works extremely well for calculating CTEs. The uncertainty of the CTE of diamond is below 3 % above 300 K. Below this temperature the values are so small that the relative uncertainty is not a good measure of the uncertainty.

6.2. Conclusion of $TiFe_2Si$

The CTE of $TiFe_2Si$ does have a very similar shape as that of diamond. It is negative below 5 K. Compared to the other similar materials, the CTE of $TiFe_2Si$ is lower at temperatures above 200 K which means that it expands less above this temperature. Under 200 K it was more equal. The frequencies of the phonons in $TiFe_2Si$ are higher than for the compared materials. There has not been found any coherence between the dispersion relations of the materials and their CTE. This may be due to different methods of the investigations. The symmetry of $TiFe_2Si$ is so that the piezoelectric tensor is zero and the second term of the pyroelectric vector is zero.

6.3. Conclusion of $GaNaTe_2$

The CTE of the lattice parameters of β-$GaNaTe_2$ does have some similarity to the CTEs of diamond and $TiFe_2Si$, but is not quite the same. The CTE of the a-lattice parameter is the largest of the materials in this study and the CTE of the c-lattice parameter is the next highest for most temperatures, only preceded by the CTE of the a-lattice parameter of $GaCuSe_2$ around 600 K. Only the non-pyroelectric phase of β-$GaNaTe_2$ was found to be stable within these calculations. Therefore, it has not been proven that this system could potentially produce electricity from heat. If the other phase is stable in reality, cannot be concluded.

6.4. Conclusion of $GaCuSe_2$

The CTE of the a-lattice parameter of $GaCuSe_2$ does have a similar behavior to that of the a-lattice parameter of diamond, $TiFe_2Si$ and β-$GaNaTe_2$. The CTE of the c-lattice parameter on the other hand shows a behavior that has not been seen for the other materials. The expansion is higher along the a-lattice parameter than along the c-lattice parameter. The expansion along the a-lattice parameter is lower than the expansion along the a-lattice parameter of β-$GaNaTe_2$, but for most temperatures higher than the expansion of diamond and $TiFe_2Si$. The expansion along the c-lattice parameter was lower for $GaCuSe_2$ compared with β-$GaNaTe_2$, higher than that of diamond for most of the temperatures, and dependent on temperature compared to $TiFe_2Si$. The uncertainty was below 5 % for most temperatures. The symmetry of $GaCuSe_2$ made it possible to have a non-zero piezoelectric tensor. Indeed, it was nonzero, and the second term of the pyroelectric vector was calculated as a function of temperature. It is very promising for the future that it can be calculated from purely ab initio assumptions.

6.5. Main conclusion

The motivation for this study was to find a PTM with bandgap in both phases and a large change in the pyroelectric vector upon the phase change. This was to achieve high energy efficiency by the electric field that will be caused by this phase transformation and design a heat harvesting technology to reduce the greenhouse gas that is a large problem for the world. To do this, four materials have been investigated. Those are diamond, a Heusler $TiFe_2Si$ in the space group 225, two phases of $GaNaTe_2$ with space group 122 and 140, and two phases of $GaCuSe_2$ with space group 122 and one with space group 225. For the phases that were stable, ab initio molecular dynamics and the TDEP package have been used to find different properties. The CTE has been found as a function of temperature from 0 K up to at least 600 K. The Gibbs free energy as a function of temperature and pressure has been found in the same temperature range as for the CTE and from 0 GPa to 18.8 GPa. The heat capacity has been found as a function of temperature in the same range as the CTE. The lattice constant has also been found as a function of temperature in the same range, although it is not expected to be correct. The piezoelectric tensors of the materials have been found, and by combining it with the CTEs, the secondary pyroelectric vectors have been found. The third order force constants have been calculated and converged with respect to configurations for $TiFe_2Si$.

The Gibbs free energy was found for each material. If there were two phases of the materials, the Gibbs free energy would be compared for the two phases to see if there was a phase change at a given temperature and pressure. However, only one phase for each material was stable and a phase change could not be found. The instability of the other phases was found from the eigenfrequencies which were imaginary, and this is called dynamical instability. The secondary pyroelectric vector was found for each phase to check if going from one phase to another would cause an electrical field in the material that would make it possible to create an external current. The heat capacity was found because it is interesting in many situations and because it is automatically calculated within TDEP when calculating the free energies and therefore easy to plot. The CTE is found from the lattice constant and is therefore a result that automatically comes using the method in this thesis. The third order force constants are necessary to calculate the first term of the pyroelectric coefficients and is therefore interesting to investigate for further work finding the complete pyroelectric coefficients.

The method used works very well. That is, the CTE has been found with impressive similar results to experimental data where they existed, from completely ab initio principles with no parameters from experimental data over a wide temperature range. That is, for diamond, the low temperature high accuracy data from Stoupin and Shvyd’ko were very close to being inside the accuracy range of this study for almost all points. For higher temperatures it followed the trend of the experimental points all the way up to 2000 K. This shows how good GGA exchange-correlation potentials works for calculation of properties that are not dependent of the bandgap. The CTE of diamond was plotted up to 3000 K in this study, even though it is only stable up to 1800 K as mentioned earlier. Further the CTE was found for $TiFe_2Si$ up to 3000 K and even for the β phase of $GaNaTe_2$ and $GaCuSe_2$ which are anisotropic materials. For $GaNaTe_2$ the CTE was found for both independent lattice parameters up to 600 K. Calculating the CTEs of anisotropic materials from ab initio calculations are not something that have been done often earlier. The number volumes that are required for calculating the CTE for an isotropic material have to be raised to the second and third power for an anisotropic material with two and three independent lattice parameters respectively. This study has shown that instead of using volumes with lattice parameters with one percent gap, lattice parameters with two percent gap have been sufficient, not including the equilibrium structure at 0 K and adding a compression at minus three percent. This reduces the volume grid for an expansion up to 5 percent from 8^2 = 64 to 5^5 = 25 for a tetragonal structure. That is, the CPU hours needed are less than half of what was originally assumed. The piezoelectric tensor was found, and from those the secondary pyroelectric vector which was zero for most materials. Further, the Gibbs free energy has been found as a function of temperature and pressure for all materials. Also, the CPU and memory requirements were not prohibitive to perform all the steps of the calculations required to achieve the second term of the pyroelectric coefficients. So, the conclusion is that it is very possible to calculate the second term of the pyroelectric coefficient. This was also done for $GaCuSe_2$ in the range from 0 K to 2000 K, with the temperature dependence from the CTEs.

7. Future work

Unfortunately, the other phase of the materials investigated was not stable shown from the imaginary phonon frequencies. Therefore, the Gibbs free energy of the two phases could not be compared to make a phase diagram with respect to temperature and pressure and the change in pyroelectricity could not be measured. Future work will be to find a material with two phases that are stable and have bandgap, then calculate the secondary pyroelectric vectors for them which hopefully are different for the two phases. Even further, the other terms of the pyroelectric coefficient could be calculated too.

References

1. Lang, S. B., Pyroelectricity: From ancient curiosity to modern imaging tool. *Physics Today* **2005,** *58* (8), 31-36.
2. Kresse, G.; Hafner, J., Ab initio molecular dynamics for liquid metals. *Phys. Rev. B* **1993,** *47* (1), 558-561.
3. Kresse, G.; Hafner, J., Ab initio molecular-dynamics simulation of the liquid-metal--amorphous-semiconductor transition in germanium. *Phys. Rev. B* **1994,** *49* (20), 14251-14269.
4. Kresse, G.; Furthmüller, J., Efficiency of ab-initio total energy calculations for metals and semiconductors using a plane-wave basis set. *Computational Materials Science* **1996,** *6* (1), 15-50.
5. Kresse, G.; Furthmüller, J., Efficient iterative schemes for ab initio total-energy calculations using a plane-wave basis set. *Phys. Rev. B* **1996,** *54* (16), 11169-11186.
6. Hellman, O.; Abrikosov, I. A.; Simak, S. I., Lattice dynamics of anharmonic solids from first principles. *Phys. Rev. B* **2011,** *84* (18), 180301.
7. Hellman, O.; Abrikosov, I. A., Temperature-dependent effective third-order interatomic force constants from first principles. *Phys. Rev. B* **2013,** *88* (14), 144301.
8. Hellman, O.; Steneteg, P.; Abrikosov, I. A.; Simak, S. I., Temperature dependent effective potential method for accurate free energy calculations of solids. *Phys. Rev. B* **2013,** *87* (10), 104111.
9. Born, M., On the Quantum Theory of Pyroelectricity. *Reviews of Modern Physics* **1945,** *17* (2-3), 245-251.
10. Szigeti, B., Temperature Dependence of Pyroelectricity. *Physical Review Letters* **1975,** *35* (22), 1532-1534.
11. Radousky, H. B.; Liang, H., Energy harvesting: an integrated view of materials, devices and applications. *Nanotechnology* **2012,** *23* (50), 35.
12. Valant, M., Electrocaloric materials for future solid-state refrigeration technologies. *Progress in Materials Science* **2012,** *57* (6), 980-1009.
13. Sebald, G.; Guyomar, D.; Agbossou, A., On thermoelectric and pyroelectric energy harvesting. *Smart Materials & Structures* **2009,** *18* (12).
14. Liu, W. S.; Jie, Q.; Kim, H. S.; Ren, Z. F., Current progress and future challenges in thermoelectric power generation: From materials to devices. *Acta Materialia* **2015,** *87*, 357-376.
15. Chluba, C.; Ge, W.; de Miranda, R. L.; Strobel, J.; Kienle, L.; Quandt, E.; Wuttig, M., Ultralow-fatigue shape memory alloy films. *Science* **2015,** *348* (6238), 1004-1007.
16. James, R. D., Taming the temperamental metal transformation. *Science* **2015,** *348* (6238), 968-969.
17. Song, Y.; Chen, X.; Dabade, V.; Shield, T. W.; James, R. D., Enhanced reversibility and unusual microstructure of a phase-transforming material. *Nature* **2013,** *502* (7469), 85-88.
18. Chen, X.; Srivastava, V.; Dabade, V.; James, R. D., Study of the cofactor conditions: Conditions of supercompatibility between phases. *Journal of the Mechanics and Physics of Solids* **2013,** *61* (12), 2566-2587.
19. Shulumba, N.; Hellman, O.; Rogstrom, L.; Raza, Z.; Tasnadi, F.; Abrikosov, I. A.; Oden, M., Temperature-dependent elastic properties of Ti1-xAlxN alloys. *Applied Physics Letters* **2015,** *107* (23), 4.
20. Liu, J.; Fernández-Serra, M. V.; Allen, P. B., First-principles study of pyroelectricity in GaN and ZnO. *Phys. Rev. B* **2016,** *93* (8), 081205.
21. Liu, J.; Pantelides, S. T., Mechanisms of Pyroelectricity in Three- and Two-Dimensional Materials. *Physical Review Letters* **2018,** *120* (20), 207602.
22. Giannozzi, P.; Baroni, S.; Bonini, N.; Calandra, M.; Car, R.; Cavazzoni, C.; Ceresoli, D.; Chiarotti, G. L.; Cococcioni, M.; Dabo, I.; Dal Corso, A.; de Gironcoli, S.; Fabris, S.; Fratesi, G.; Gebauer, R.; Gerstmann, U.; Gougoussis, C.; Kokalj, A.; Lazzeri, M.; Martin-Samos, L.; Marzari, N.; Mauri, F.; Mazzarello, R.; Paolini, S.; Pasquarello, A.; Paulatto, L.; Sbraccia, C.; Scandolo, S.; Sclauzero, G.; Seitsonen, A. P.; Smogunov, A.; Umari, P.; Wentzcovitch, R. M., QUANTUM

ESPRESSO: a modular and open-source software project for quantum simulations of materials. *Journal of Physics: Condensed Matter* **2009,** *21* (39), 395502.
23. Perdew, J. P.; Wang, Y., Accurate and simple analytic representation of the electron-gas correlation energy. *Phys. Rev. B* **1992,** *45* (23), 13244-13249.
24. Baroni, S.; de Gironcoli, S.; Dal Corso, A.; Giannozzi, P., Phonons and related crystal properties from density-functional perturbation theory. *Reviews of Modern Physics* **2001,** *73* (2), 515-562.
25. Matocha, K.; Tilak, V.; Dunne, G., Comparison of metal-oxide-semiconductor capacitors on c- and m-plane gallium nitride. *Applied Physics Letters* **2007,** *90* (12), 123511.
26. Bykhovski, A. D.; Kaminski, V. V.; Shur, M. S.; Chen, Q. C.; Khan, M. A., Pyroelectricity in gallium nitride thin films. *Applied Physics Letters* **1996,** *69* (21), 3254-3256.
27. Heiland, G.; Ibach, H., Pyroelectricity of zinc oxide. *Solid State Communications* **1966,** *4* (7), 353-356.
28. Raghavan, V., Fe-Si-Ti (Iron-Silicon-Titanium). *Journal of Phase Equilibria and Diffusion* **2009,** *30* (4), 393-396.
29. David S. Sholl, J. A. S., Density functional theory: a practical introduction. Wiley: Hoboken, N.J, 2009; p 9.
30. David S. Sholl, J. A. S., Density functional theory: a practical introduction. Wiley: Hoboken, N.J, 2009; p 10.
31. David S. Sholl, J. A. S., Density functional theory: a practical introduction. Wiley: Hoboken, N.J, 2009; p 11.
32. David S. Sholl, J. A. S., Density functional theory: a practical introduction. Wiley: Hoboken, N.J, 2009; p 12.
33. David S. Sholl, J. A. S., Density functional theory: a practical introduction. Wiley: Hoboken, N.J, 2009; p 13.
34. David S. Sholl, J. A. S., Density functional theory: a practical introduction. Wiley: Hoboken, N.J, 2009; p 14.
35. David S. Sholl, J. A. S., Density functional theory: a practical introduction. Wiley: Hoboken, N.J, 2009; p 15.
36. Griffiths, D. J., Introduction to Quantum Mechanics. Second edition ed.; Cambridge University Press: 2017; p 251.
37. Giannozzi, P.; de Gironcoli, S.; Pavone, P.; Baroni, S., Ab initio calculation of phonon dispersions in semiconductors. *Phys. Rev. B* **1991,** *43* (9), 7231-7242.
38. Pavone, P.; Karch, K.; Schütt, O.; Strauch, D.; Windl, W.; Giannozzi, P.; Baroni, S., Ab initio lattice dynamics of diamond. *Phys. Rev. B* **1993,** *48* (5), 3156-3163.
39. Le Page, Y.; Saxe, P., Symmetry-general least-squares extraction of elastic data for strained materials from ab initio calculations of stress. *Phys. Rev. B* **2002,** *65* (10), 104104.
40. Kittel, C., Introduction to Solid State Physics. 8 ed.; John Wiley & Sons, Inc: 2005; p 73.
41. Kittel, C., Introduction to Solid State Physics. 8 ed.; John Wiley & Sons, Inc: 2005; p 76.
42. Kittel, C., Introduction to Solid State Physics. 8 ed.; John Wiley & Sons, Inc: 2005; p 75.
43. Kittel, C., Introduction to Solid State Physics. 8 ed.; John Wiley & Sons, Inc: 2005; p 78.
44. T. Jia, G. C., and Y. Zhang, Lattice thermal conductivity evaluated using elastic properties. *Physical Review B* **2017,** *95*, 2.
45. Pike, N. A.; Løvvik, O. M., Calculation of the anisotropic coefficients of thermal expansion: A first-principles approach. *Computational Materials Science* **2019,** *167*, 257-263.
46. Shulumba, N.; Hellman, O.; Minnich, A. J., Intrinsic localized mode and low thermal conductivity of PbSe. *Phys. Rev. B* **2017,** *95* (1), 014302.
47. Dove, M. T., Introduction to Lattice Dynamics. Press Syndicate of the University of Cambridge: 1993; p 85.
48. Dove, M. T., Introduction to Lattice Dynamics. Press Syndicate of the University of Cambridge: 1993; p 86.

49. West, D.; Estreicher, S. K., First-Principles Calculations of Vibrational Lifetimes and Decay Channels: Hydrogen-Related Modes in Si. *Physical Review Letters* **2006,** *96* (11), 115504.
50. Maradudin, A. A.; Vosko, S. H., Symmetry Properties of the Normal Vibrations of a Crystal. *Reviews of Modern Physics* **1968,** *40* (1), 1-37.
51. Dove, M. T., Introduction to Lattice Dynamics. Press Syndicate of the University of Cambridge: 1993; p 65.
52. Birch, F., Finite Elastic Strain of Cubic Crystals. *Physical Review* **1947,** *71* (11), 809-824.
53. Schroeder, D. V., An Introduction to Thermal Physics. 1 ed.; Pearson Education Limited: 2014; p 157.
54. Schroeder, D. V., An Introduction to Thermal Physics. 1 ed.; Pearson Education Limited: 2014; p 150.
55. Liu, J.; Allen, P. B.; Fernández-Serra, M., Erratum: First-principles study of pyroelectricity in GaN and ZnO [Phys. Rev. B 93, 081205(R) (2016)]. *Phys. Rev. B* **2018,** *98* (3), 039905.
56. Løvvik, O. M.; Pike, N. A., Unpublished work.
57. Løvvik, O. M., Kvantemekaniske modellering av nanomaterialer. University of Oslo, 2019.
58. Jacobson, P.; Stoupin, S., Thermal expansion coefficient of diamond in a wide temperature range. *Diamond and Related Materials* **2019,** *97*, 107469.
59. Stoupin, S.; Shvyd'ko, Y. V., Thermal Expansion of Diamond at Low Temperatures. *Physical Review Letters* **2010,** *104* (8), 085901.
60. Stoupin, S.; Shvyd'ko, Y. V., Ultraprecise studies of the thermal expansion coefficient of diamond using backscattering x-ray diffraction. *Phys. Rev. B* **2011,** *83* (10), 104102.
61. Xu, C. H.; Wang, C. Z.; Chan, C. T.; Ho, K. M., Theory of the thermal expansion of Si and diamond. *Phys. Rev. B* **1991,** *43* (6), 5024-5027.
62. Slack, G. A.; Bartram, S. F., Thermal expansion of some diamondlike crystals. *Journal of Applied Physics* **1975,** *46* (1), 89-98.
63. Skinner, B. J., Thermal Expansion of Thoria, Periclase, and Diamond. *Am. Mineralogist* **1957,** *Vol: 42*.
64. Krishnan, R. S., Thermal Expansion of Diamond. *Nature* **1944,** *154* (3911), 486-487.
65. Krishnan, R. S., Thermal expansion of diamond. *Proceedings of the Indian Academy of Sciences - Section A* **1946,** *24* (1), 33.
66. Sato, T.; Ohashi, K.; Sudoh, T.; Haruna, K.; Maeta, H., Thermal expansion of a high purity synthetic diamond single crystal at low temperatures. *Phys. Rev. B* **2002,** *65* (9), 092102.
67. Mounet, N.; Marzari, N., First-principles determination of the structural, vibrational and thermodynamic properties of diamond, graphite, and derivatives. *Phys. Rev. B* **2005,** *71* (20), 205214.
68. Vanderbilt, D., Soft self-consistent pseudopotentials in a generalized eigenvalue formalism. *Phys. Rev. B* **1990,** *41* (11), 7892-7895.
69. Perdew, J. P.; Burke, K.; Ernzerhof, M., Generalized Gradient Approximation Made Simple. *Physical Review Letters* **1996,** *77* (18), 3865-3868.
70. Herrero, C. P.; Ramírez, R., Structural and thermodynamic properties of diamond: A path-integral Monte Carlo study. *Phys. Rev. B* **2000,** *63* (2), 024103.
71. Noui, S.; Charifi, Z.; Baaziz, H.; Uğur, G.; Uğur, Ş., Effect of Structure on the Electronic, Magnetic and Thermal Properties of Cubic Fe2MnxNi1−xSi Heusler Alloys. *Journal of Electronic Materials* **2019,** *48* (1), 337-351.
72. Blaha, P.; Schwarz, K.; Tran, F.; Laskowski, R.; Madsen, G. K. H.; Marks, L. D., WIEN2k: An APW+lo program for calculating the properties of solids. *The Journal of Chemical Physics* **2020,** *152* (7), 074101.
73. Perdew, J. P.; Zunger, A., Self-interaction correction to density-functional approximations for many-electron systems. *Phys. Rev. B* **1981,** *23* (10), 5048-5079.
74. Otero-de-la-Roza, A.; Luaña, V., Gibbs2: A new version of the quasi-harmonic model code. I. Robust treatment of the static data. *Computer Physics Communications* **2011,** *182* (8), 1708-1720.

75. Otero-de-la-Roza, A.; Abbasi-Pérez, D.; Luaña, V., Gibbs2: A new version of the quasiharmonic model code. II. Models for solid-state thermodynamics, features and implementation. *Computer Physics Communications* **2011,** *182* (10), 2232-2248.
76. Yan, X.; Grytsiv, A.; Rogl, P.; Pomjakushin, V.; Palm, M., The Heusler Phase Ti25(Fe50 − xNix)Al25 (0 ≤ x ≤ 50); Structure and Constitution. *Journal of Phase Equilibria and Diffusion* **2008,** *29* (6), 500-508.
77. Paudel, R.; Zhu, J., Theoretical Study of Structural, Magnetic, Elastic, Phonon, and Thermodynamic Properties of Heusler Alloys Fe2CrX (X = Al, Ga). *Journal of Superconductivity and Novel Magnetism* **2018,** *31* (6), 1791-1798.
78. Payne, M. C.; Teter, M. P.; Allan, D. C.; Arias, T. A.; Joannopoulos, J. D., Iterative minimization techniques for ab initio total-energy calculations: molecular dynamics and conjugate gradients. *Reviews of Modern Physics* **1992,** *64* (4), 1045-1097.
79. Fischer, T. H.; Almlof, J., General methods for geometry and wave function optimization. *The Journal of Physical Chemistry* **1992,** *96* (24), 9768-9774.
80. Blanco, M. A.; Francisco, E.; Luaña, V., GIBBS: Isothermal-Isobaric Thermodynamics of Solids From Energy Curves Using a Quasi-Harmonic Debye Model. *Computer Physics Communications* **2004,** *158*, 57-72.
81. Otero-de-la-Roza, A.; Abbasi-Pérez, D.; Luaña, V., GIBBS2: A new version of the quasiharmonic model code. II. Models for solid-state thermodynamics, features and implementation. *Computer Physics Communications* **2011,** *182*, 2232-2248.
82. Haas, P.; Tran, F.; Blaha, P., Calculation of the lattice constant of solids with semilocal functionals. *Phys. Rev. B* **2009,** *79* (8), 085104.
83. Weitzer, F.; Schuster, J. C.; Naka, M.; Stein, F.; Palm, M., On the reaction scheme and liquidus surface in the ternary system Fe–Si–Ti. *Intermetallics* **2008,** *16* (2), 273-282.
84. Csonka, G. I.; Perdew, J. P.; Ruzsinszky, A.; Philipsen, P. H. T.; Lebègue, S.; Paier, J.; Vydrov, O. A.; Ángyán, J. G., Assessing the performance of recent density functionals for bulk solids. *Phys. Rev. B* **2009,** *79* (15), 155107.

Appendix A

The tables in this appendix specifies the INCAR input used for the different calculations. The NPAR parameter, which decides the number of bands that are treated parallel, is not specified as this varied to be as close as possible to the square root of the number of cores for each calculation.

- Table 9 shows the input for the energy cutoff of the planewave basis set test.
- Table 10 and Table 11 shows the input for the relaxation of the materials.
- Table 12 and Table 13 shows the input for the DFPT calculations.
- Table 14 shows the input for the calculations of the canonical configurations.
- Table 15 and Table 16 shows the input for the relaxation of the supercells.

Table 9: INCAR input for diamond, TiFeSi system, $GaNaTe_2$ system and $GaCuSe_2$ for the energy cutoff test. ALGO decides the electronic minimisation algorithm. ALGO = Fast uses the Davidson algorithm in the initial phase, then switches to the RMM-DIIS. NELMIN decides the minimum number of electronic self-consistent steps. EDIFF decides the break condition of the electronic steps with respect to difference in energy between two steps. PREC decides the number of grid points in the fast Fourier transform-grid and how accurate the projectors are represented in in real space. LREAL decides if the projection operators are evaluated in reciprocal or real space. ISMEAR determines the function for smearing for each orbital. SIGMA determines the width of the smearing in eV. ISPIN = 2 decides that spin polarized calculations are done. For GGA = not specified, the PBE[69] GGA will be used and for GGA = PS, PBE-sol[84] will be used.

Parameter:	Diamond:	TiFeSi:	$GaNaTe_2$:	$GaCuSe_2$:
ALGO	Fast	Fast	Fast	Fast
NELMIN	4	4	4	4
EDIFF	10^{-5}	10^{-5}	10^{-6}	10^{-6}
PREC	Normal	Normal	Normal	Normal
LREAL	.FALSE.	.FALSE.	.FALSE.	.FALSE.
ISMEAR	-5	-5	-5	-5
SIGMA	0.2	0.2	0.2	0.2
ISPIN	2	2	2	2
GGA	Not specified	Not specified	PS	PS

Table 10: INCAR values for electronic relaxation for diamond, $TiFe_2Si$, $GaNaTe_2$ and $GaCuSe_2$ for the relaxation calculations. NELM decides the maximum number of self-consistent electronic steps. ENCUT is the energy cutoff value.

Parameter:	Diamond:	$TiFe_2Si$:	$GaNaTe_2$:	Tetragonal $GaCuSe_2$:	Cubic $GaCuSe_2$:
ALGO	Fast	Fast	Fast	Fast	Fast
NELMIN	4	4	4	4	4
NELM	Not specified	Not specified	Not specified	300	300
EDIFF	10^{-5}	10^{-6}	10^{-6}	10^{-6}	10^{-6}
ENCUT	450	500	400	450	500
PREC	Accurate	Accurate	Accurate	Accurate	Accurate
LREAL	Auto	.FALSE.	.FALSE.	.FALSE.	.False.
ISMEAR	0	0	0	0	0
SIGMA	0.2	0.2	0.2	0.2	0.2
ISPIN	2	2	2	2	2
GGA	Not specified	PS	PS	PS	PS

Table 11: INCAR values for ionic relaxation for diamond, $TiFe_2Si$, $GaNaTe_2$ and $GaCuSe_2$ for the relaxation calculations. EDIFFG decides the condition for breaking the ionic relaxation loop with respect to forces between to ionic steps when it is negative. NSW is the maximum number of ionic steps. MAXMIX specifies the maximal rank of the approximation of the charge dielectric function build up by the Broyden mixer. IBRION decides how the ions are updated and moved. IBRION = 1

makes VASP use the RMM-DIIS method to find the 0 K structure. ISIF decides if the stress tensor is calculated and if the positions, call shape and cell volume are free to vary. ISIF = 3 decides that the stress tensor is calculated and that positions, cell shape and cell volume are free to vary. ADDGRID decides if an additional support grid is used when evaluating the augmentation charges.

Parameter:	Diamond:	$TiFe_2Si$:	$GaNaTe_2$:	Tetragonal $GaCuSe_2$:	Cubic $GaCuSe_2$:
EDIFFG	-0.01	-0.001	-0.001	-0.001	-0.001
NSW	80	80	80	80	80
MAXMIX	80	80	80	80	80
IBRION	1	1	1	1	1
ISIF	3	3	3	3	3
ADDGRID	.TRUE.	.TRUE.	.TRUE.	.TRUE.	.TRUE.

Table 12: INCAR values for electronic relaxation for calculation of elastic parameters of Diamond, $TiFe_2Si$, $GaNaTe_2$ and $GaCuSe_2$ for the DFPT calculations.

Parameter:	Diamond:	$TiFe_2Si$:	α-$GaNaTe_2$:	β- $GaNaTe_2$:	$GaCuSe_2$:
ALGO	Fast	Fast	Fast	Fast	Fast
NELMIN	4	4	4	4	4
NELM	200	200	200	200	200
EDIFF	10^{-7}	10^{-7}	10^{-7}	10^{-7}	10^{-7}
ENCUT	450	500	500	400	450
PREC	Accurate	Accurate	Accurate	Accurate	Accurate
LREAL	.FALSE.	.FALSE.	.FALSE.	.FALSE.	.FALSE.
ISMEAR	-5	-5	-5	-5	-5
SIGMA	0.2	0.2	0.2	0.2	0.2
ISPIN	2	2	2	2	2
GGA	Not specified	PS	PS	PS	PS

Table 13: INCAR values for calculation of elastic parameters for Diamond, $TiFe_2Si$, $GaNaTe_2$ and $GaCuSe_2$ for the DFPT calculations. IBRION = 6 determines that the Hessian matrix and the vibrational frequencies should be calculated. NFREE decides how many displacements are used for each direction and ion. LEPSILON = .TRUE. determines the electronic contribution to the piezoelectric tensor, the static dielectric matrix and the Born effective charges using DFPT.

Parameter:	Diamond:	$TiFe_2Si$:	α-$GaNaTe_2$:	β- $GaNaTe_2$:	$GaCuSe_2$:
IBRION	6	6	6	6	6
NFREE	2	2	2	2	2
ISIF	3	3	3	3	3
LEPSILON	.TRUE.	.TRUE.	.TRUE.	.TRUE.	.TRUE.

Table 14: INCAR values for electronic relaxation for Diamond, $TiFe_2Si$, $GaNaTe_2$ and $GaCuSe_2$ for the canonical configuration calculations.

Parameter:	Diamond:	$TiFe_2Si$:	α-$GaNaTe_2$:	β- $GaNaTe_2$:	$GaCuSe_2$:
ALGO	Fast	Fast	Fast	Fast	Fast
NELMIN	4	4	4	4	4
EDIFF	10^{-5}	10^{-6}	10^{-6}	10^{-6}	10^{-6}
ENCUT	400	500	400	400	450
PREC	Normal	Normal	Normal	Normal	Normal
LREAL	.FALSE.	.FALSE.	.FALSE.	.FALSE.	.FALSE.

ISMEAR	-5	-5	-5	-5	-5
SIGMA	0.2	0.2	0.2	0.2	0.2
ISPIN	2	2	2	2	2
GGA	Not specified	PS	PS	PS	PS

Table 15: INCAR values for electronic relaxation for $GaCuSe_2$ for the supercell relaxations.

Parameter:	Value:
ALGO	Fast
NELMIN	4
NELM	300
EDIFF	10^{-6}
ENCUT	450
PREC	Accurate
LREAL	.False.
ISMEAR	0
SIGMA	0.2
ISPIN	2
GGA	PS

Table 16: INCAR values for ionic relaxation for the supercell relaxations. ISIF = 2 is the difference from the earlier ionic relaxation which do not allow the lattice parameters to change.

Parameter:	Value:
EDIFFG	-0.001
NSW	80
MAXMIX	80
IBRION	1
ISIF	2
ADDGRID	.TRUE.

Appendix B

The tables in this appendix show the difference in vibrational free energy as a function of different parameters. They are used for convergence of the vibrational free energy.

- Table 17, Table 18 and Table 19 are with respect to number of configurations.
- Table 20 is with respect to the cutoff radius of included atoms.

- Table 21 is with respect to Debye temperature.

Table 17: Difference in free energy for $TiFe_2Si$ at 300 K for one more configuration used as a function of configurations used.

Number of configurations used	1	2	3	4
Difference in free energy using one more configuration (meV/formula)	1.4032	1.4313	0.0977	0.0574

Table 18: Difference in free energy for $TiFe_2Si$ at 1500 K for one more configuration used as a function of configurations used.

Number of configurations used	1	2	3	4
Difference in free energy using one more configuration (meV/formula)	6.0866	6.0041	0.3586	0.1736

Table 19: Difference in free energy for $TiFe_2Si$ at 3000 K for one more configuration used as a function of configurations used.

Number of configurations used	1	2	3	4
Difference in free energy using one more configuration (meV/formula)	12.1123	11.9328	0.7086	0.3398

Table 20: Difference in free energy for $TiFe_2Si$ at 300 K for one more layer of neighbour atoms included as a function of radius of including atoms at 300 K. Each cutoff value plotted corresponds to including one more layer of neighbour atoms.

Cutoff value for second order force constants (Å)	2.439	2.816	3.982	4.670	4.877	5.632	6.137
Difference in free energy including the next layer of neighbour atoms (meV/formula)	6.696	0.6173	0.7607	0.2243	0.0464	0.1075	0.1698

Table 21: Change in free energy for $TiFe_2Si$ at 300 K going from the calculated Debye temperature at 494 K to the compared Debye temperature.

Debye temperature compared (K)	100	300	700	900
Difference in free energy (meV/formula)	1.5464	0.4149	0.6710	1.7204

Appendix C

This appendix consists of tables that shows the CPU time used by the different calculations for the different materials.

Table 22: CPU time used by different calculations for diamond.

Calculation:	Time (hours:minutes:seconds):
First relaxation	00:00:18
Second relaxation	00:00:11
Elastic parameters	00:06:29
An expensive total energy calculation of supercell configuration based on any volume	17:19:04
A cheap total energy calculation of supercell configuration based on any volume	08:34:19
Most expensive total energy calculation of the small cells with any volume	00.00.05
Least expensive total energy calculation of the small cells with any volume	00.00.04

Table 23: CPU time used by different calculations for $TiFe_2Si$.

Calculation:	Time (days:hours:minutes:seconds):
First relaxation	00:00:17:55
Second relaxation	00:00:04:03
Elastic parameters	00:00:35:24
An expensive total energy calculation of supercell configuration based on any volume	222:21:25:50
A cheap total energy calculation of supercell configuration based on any volume	43:02:41:39
Most expensive total energy calculation of the small cells with any volume	00:00:02:16
Least expensive total energy calculation of the small cells with any volume	00:00:00:50

Table 24: CPU time used by different calculations for $GaNaTe_2$.

Calculation:	Time (days:hours:minutes:seconds):
First relaxation	00:02:10:09
Second relaxation	00:01:04:24
Elastic parameters	00:29:42:24
An expensive total energy calculation of supercell configuration based on any volume	84:03:47:09
A cheap total energy calculation of supercell configuration based on any volume	15:14:35:59
Most expensive total energy calculation of the small cells with any volume	00:00:13:53
Least expensive total energy calculation of the small cells with any volume	00:00:09:32

Table 25: CPU time used by different calculations for $GaCuSe_2$.

Calculation:	Time (days:hours:minutes:seconds):
First relaxation	00:00:57:14
Second relaxation	00:00:19:43
Elastic parameters	00:07:31:33
An expensive relaxation of a supercell	138:10:31:47
A cheap relaxation of a supercell	31:00:19:48
An expensive total energy calculation of supercell configuration based on any volume	79:06:58:12
A cheap total energy calculation of supercell configuration based on any volume	21:18:18:50
Most expensive total energy calculation of the small cells with any volume	00:00:03:49
Least expensive total energy calculation of the small cells with any volume	00:00:02:35